
Generation of turbulence by means of active grids for wind turbine investigations

Erzeugung von Turbulenz mittels aktiver Gitter
für Untersuchungen von Windenergieanlagen

Lars Kristian Neuhaus

Von der Fakultät für Mathematik und Naturwissenschaften
der Carl von Ossietzky Universität Oldenburg
zur Erlangung des Grades und Titels eines

DOKTOR DER INGENIEURWISSENSCHAFTEN
DR.-ING.

angenommene Dissertation
von Herrn Lars Kristian Neuhaus
geboren am 19.03.1990 in Bonn



Erstgutachter: Prof. Dr. Joachim Peinke

Zweitgutachter: Assoc. Prof. Dr. R. Jason Hearst

Tag der Abgabe: 15.08.2022

Tag der Disputation: 01.12.2022

Contents

Abstract / Zusammenfassung	v
1 Introduction	1
2 State of the art	5
2.1 Wind energy	5
2.2 Turbulence	11
2.3 Stochastic analysis - The Langevin approach	19
3 Exploring the capabilities of active grids	21
3.1 Experimental setup and flow generation	21
3.2 Generation of specific flow structures	25
3.3 Application to turbulence	34
3.4 Conclusion	37
4 Generation of atmospheric turbulence	39
4.1 Experimental setup and turbulence excitation	40
4.2 Analysis of the generated flow	41
4.3 Conclusion	48
5 Model wind turbine in turbulent inflow	49
5.1 Experimental setup and methods	50
5.2 Results	54
5.3 Conclusion	68
6 Conclusion	71
Appendix	81
A Generation of atmospheric turbulence	81
B Model wind turbine in turbulent inflow	82
Acknowledgements / Danksagung	87
Curriculum	89

List of publications	91
Erklärung	95

Abstract

Wind energy is an important part of the energy transformation. The increasing size of wind turbines requires a detailed analysis of new turbine concepts. These turbines, exposed to turbulent wind, require realistic testing.

The most realistic investigations can be undertaken in the free field. However, those measurements are difficult, lengthy, costly and not reproducible. Numerical investigations allow to test different concepts and easily vary design parameters. But, they cannot cover all details and require simplifications, especially for dynamic effects and turbulence. Wind tunnel measurements offer the possibility to investigate scaled models under realistic conditions. Yet, it is restricted to the tunnel size and requires scaling of the models. In this way, wind tunnel measurements with realistic inflow conditions and numerical investigations with an easy variation of design parameters complete each other and are the tool of choice for wind energy research.

To produce meaningful results, realistic flows in the wind tunnel are needed. In this work, a new method to produce large scale turbulent flows in the wind tunnel by means of active grids is developed. The possibilities to generate these reproducible turbulent wind fields are investigated. In the following, the generated inflow situations are used to investigate the dynamic properties of different rotor configurations of a model wind turbine by means of the Langevin approach. Thus, a method for the systematic investigation of wind turbines in a wind tunnel is provided.

It was shown that the structures that can be imprinted by active grids depend on the reduced frequency. The generated flows undergo a transition downstream and form a fully developed turbulence far behind the active grid. In combination with a dynamic speed variation of the wind tunnel fans, very large Reynolds numbers and integral length scales can be achieved. The dynamic properties of a model turbine under these inflow conditions can be studied in detail using the Langevin approach and differences in the dynamics between different configurations can be specifically assigned to operational points.

Zusammenfassung

Windenergie ist ein wichtiger Teil der Energietransformation. Die zunehmende Größe von Windkraftanlagen erfordert eine detaillierte Analyse neuer Anlagenkonzepte. Diese Windenergieanlagen, die dem turbulenten Wind ausgesetzt sind, müssen realitätsnah getestet werden.

Die realistischsten Untersuchungen können im Freifeld durchgeführt werden. Diese Messungen sind jedoch schwierig, langwierig, kostenintensiv und nicht reproduzierbar. Numerische Untersuchungen ermöglichen es, verschiedene Konzepte zu testen und Designparameter einfach zu variieren. Sie können jedoch nicht alle Details abdecken und erfordern Vereinfachungen, besonders im Bereich dynamischer Effekte und Turbulenz. Windkanalmessungen bieten die Möglichkeit, skalierte Modelle unter realistischen Bedingungen zu untersuchen. Sie sind jedoch auf die Tunnelgröße beschränkt und erfordern eine Skalierung der Modelle. Auf diese Weise ergänzen sich Windkanalmessungen mit realistischen Anströmbedingungen und numerische Untersuchungen mit einer einfachen Variation der Entwurfparameter und sind das Mittel der Wahl für die Windenergieforschung.

Um aussagekräftige Ergebnisse zu erhalten, werden realistische Strömungen im Windkanal benötigt. In dieser Arbeit wird eine neue Methode zur Erzeugung großskaliger turbulenter Strömungen im Windkanal mittels aktiver Gitter entwickelt. Es werden die Möglichkeiten zur Erzeugung dieser reproduzierbaren turbulenten Windfelder untersucht. Im Folgenden werden die erzeugten Anströmsituationen genutzt, um die dynamischen Eigenschaften verschiedener Rotorkonfigurationen einer Modellwindkraftanlage mit Hilfe des Langevin-Ansatzes zu untersuchen. Damit wird eine Methode zur systematischen Untersuchung von Windenergieanlagen im Windkanal bereitgestellt.

Es konnte gezeigt werden, dass die mittels aktiver Gitter aufprägbaren Strukturen von der reduzierten Frequenz abhängen. Die erzeugten Strömungen unterlaufen eine Transition und bilden eine vollständig entwickelte Turbulenz weit hinter dem aktiven Gitter aus. In Kombination mit einer dynamischen Geschwindigkeitsvariation der Windkanalgebläse lassen sich so sehr große Reynoldszahlen und integrale Längen erzeugen. Die dynamischen Eigenschaften einer Modellanlage unter diesen Einströmbedingungen können mittels des Langevin Ansatzes detailliert untersucht und Unterschiede der Dynamik zwischen verschiedenen Konfigurationen gezielt Betriebsbereichen zugeordnet werden.

Chapter 1

Introduction

The climate change is here. The CO₂ rate in the atmosphere increased from 280 ppm before the industrial revolution to 410 ppm in 2018. Not the only but the major reason for a rising global temperature, which till today has increased by 1.1 °C compared to the pre-industrial time (Gillett et al., 2021). This increase is not about to slow down. There are different scenarios on the future development (Chen et al., 2021). Without any climate policies, the prognostic temperature rise till the end of the century is in the range of 4.1 °C to 4.8 °C compared to the pre-industrial time (Ritchie et al., 2020). With dramatic consequences world wide, as a rise of the ocean level, droughts, floods, and an accumulation of extreme weather events in general. The most optimistic scenarios still claim a rise of 1.5 °C, but only if rapid and dramatic changes are made. However, this might not be very likely and the most realistic scenario today predicts a rise of 2.2 °C to 2.9 °C (Sognaes et al., 2021). Hence, there is an urgent need to reduce this temperature rise. The reduction of CO₂ emissions plays a key role here.

Due to the climate change, in the last decades the global interest in wind energy increased. Wind is an important source of renewable (CO₂-free) energy and is treated as the most important source to achieve an energy transition away from the carbon-based energy production. Currently, the share of renewable electric energy is 29% world wide and 44.9% in Germany¹, and wind is contributing 6.2% (21.2% of renewable) world wide and 23.7% (52.8% of renewable) in Germany (Ritchie and Roser, 2020). In 2020 the global installed wind converter capacity reached 743 GW. In the last years the growth rate increased and reached more than 90 GW installed capacity in 2020 (GWEC, 2021). Thus, there is a high demand for wind turbines.

To fulfill this request of continuous growth, turbines get larger and larger. The average rotor diameter of wind turbines installed in Germany in 2010 was 80 m with a rated power of 2 MW, in 2020 it reached 122 m and 3.4 MW onshore and 153 m and 6.8 MW offshore (iwd, 2020; Deutsche Windguard, 2021b,a). The largest rotor diameters found are in the order of 230 m producing up to 15 MW. While becoming larger and larger and producing more and more power, turbines need to become more

¹In 2020, electricity had a share of about 20% of the final energy consumption worldwide and 21% in Germany

sophisticated, since a simple upscaling is not possible. The blades must become lighter, and new control concepts are needed to enable reliable operation and reduce costs due to downtime and maintenance, but also to extend the service life of the turbines.

Consequently, there is a tremendous amount of research questions which need to be addressed (Veers et al., 2019; Meneveau, 2019; Van Kuik et al., 2016). The largest wind turbines operate in heights and experience winds which till now were not investigated and considered for turbine design. Large offshore wind farms make an investigation of interactions within wind farms, but also between different wind farms, relevant (Porté-Agel et al., 2020). New turbine controls, e.g., reacting on individual blade loads (see Petrović et al., 2019) or on the inflow (e.g., model predictive control (see Bossanyi et al., 2012)) are being developed to reduce loads and hence maintenance costs. Further, the benefit of add-ons, such as vortex generators or leading edge slats, but also active devices, such as active slats and flaps are to be investigated (Aramendia et al., 2017). To name just a few examples (the list is not exhaustive) that illustrate that there is a great desire to further and better understand and control the behavior of wind turbines in the free field.

To do so, the right methods are needed for the investigations. Tests in the free field offer the most realistic conditions. However, they are costly, lengthy and conditions, due to the constant change of the weather, are not controllable and hence also not reproducible. Simulations (computational fluid dynamics (CFD)) allow to test different concepts and easily vary design parameters. However, they cannot provide a complete picture as they require simplifications and thus a correct replication of turbulence and dynamic effects is not possible (Meneveau, 2019). Wind tunnel experiments allow for an investigation under reproducible turbulent conditions, which, once everything is setup, can easily be varied. However, the models have to be scaled and manufactured for the wind tunnel, which makes varying the design parameters cost-intensive and time-consuming. Therefore, a combination of easily varied design parameters in CFD and easily varied realistic inflow conditions in the wind tunnel is the most promising research approach.

To be able to perform meaningful measurements in the lab, defined and reproducible inflows are needed. Whereas for most applications laminar flows are required or at least sufficient, that does not apply for wind turbine research. Wind turbines are located in the atmospheric boundary layer, which is far from being laminar. Hence, turbulence needs to be generated in the wind tunnel. This is done for almost 90 years by passive grids (Simmons and Salter, 1934). Different grids allow for different flow characteristics. However, these flows are rather simple and allowing for comparatively low degrees of turbulence. To generate more complex flows with higher degrees of turbulence so-called active grids were introduced by Makita (1991). Starting with a simple random excitation, elaborated excitation methods were developed to generate flows with different characteristics (see review by Mydlarski, 2017). The benefit of those active grids is further, that they enable to generate different flows with the exactly same setup and reproduce them for repetitive tests. However, the full potential of active grids for wind energy research is not utilized.

The objective of this thesis is to develop a method to generate reproducible atmospheric-like inflow conditions in the wind tunnel and by this allow for a systematic investigation of model wind turbines. This objective is treated in three parts.

In the first part of this work, the generation process of flows using active grids is explored (Ch. 3). The possibilities to generate tailored flows and turbulence in the wind tunnel are investigated. The resulting knowledge can be used to improve the quality of the generated turbulent flows in the wind tunnel.

In the second part, the possibility to generate atmospheric-like turbulence in the wind tunnel by an active grid is investigated (Ch. 4). The new large active grid of the working group "TWiSt" offers completely new possibilities here, not only by the size of the grid, but also by the length of the measurement section. The long test section allows to investigate the downstream development of the turbulence. The observed transition to a fully developed turbulence state downstream in combination with a dynamic variation of the wind tunnel fan speed can then be used to generate atmospheric-like turbulence.

In the last part, the possibilities for a stochastic analysis of the turbine behavior in this atmospheric-like turbulence are shown (Ch. 5). This dynamic characterization, based on the Langevin approach (Anahua et al., 2008), describes the deterministic and stochastic behavior of wind turbines under dynamic inflow conditions and has so far been applied to free field turbines. The method is transferred to an aerodynamically scaled wind turbine model and its application exemplarily shown for different turbine configurations.

The needed background to understand the content of this thesis is presented in Ch. 2. It gives general information on wind energy (Sec. 2.1), turbulence (Sec. 2.2), and the applied stochastic analysis method (Sec. 2.3). This is followed by the main part of the work, which consists, on the one hand, of the generation of characteristic inflow situations in the wind tunnel (by means of an active grid, see Ch. 3 and Ch. 4) and, on the other hand, of an analysis (by means of the Langevin approach) of a model wind turbine under these inflow conditions (Ch. 5). The results in the broader context are discussed in Ch. 6.

Chapter 2

State of the art

This chapter presents a brief overview of the fundamentals of this work. A short introduction into wind energy and turbines is given in Sec. 2.1. Turbulence and its generation by active grids in the wind tunnel are described briefly in Sec. 2.2. Lastly, the herein used stochastic analysis method (the Langevin approach) is presented in Sec. 2.3.

2.1 Wind energy

Wind is an important source of renewable energy. Wind turbines are used to harvest it. In this section a brief summary on the basics for horizontal axis wind turbines (the rotor is perpendicular to the mean wind direction) is given as it may be found in textbooks such as Burton et al. (2011).

Actuator disc - extraction of wind energy

The power of the wind

$$P_{\text{wind}} = 1/2\rho Au_{\infty}^3, \quad (2.1)$$

is given by the density of the air ρ , the observed area A and the cube of the undisturbed wind speed u_{∞} . To extract energy from the wind, wind turbines transfer the kinetic energy into electric energy.

The flow passing the rotor area can be described by a stream-tube (Fig. 2.1). The velocity is reduced downstream leading to an increase of the tube's cross sectional area and consequently an increase of the static pressure up to the rotor plane (actuator disc). At the location of the rotor plane (actuator disc) a sudden reduction in pressure (Δp) can be observed, which downstream of the rotor plane increases up to the ambient pressure p_{∞} , while the wind speed further reduces. Following the Rankine-Froude theorem, the velocity at the rotor plane (actuator disc) corresponds to $u_D = 1/2(u_{\infty} + u_w) = u_{\infty}(1 - a)$ with the wake velocity $u_w = u_{\infty}(1 - 2a)$ far downstream of the turbine and a the induction factor of the turbine.

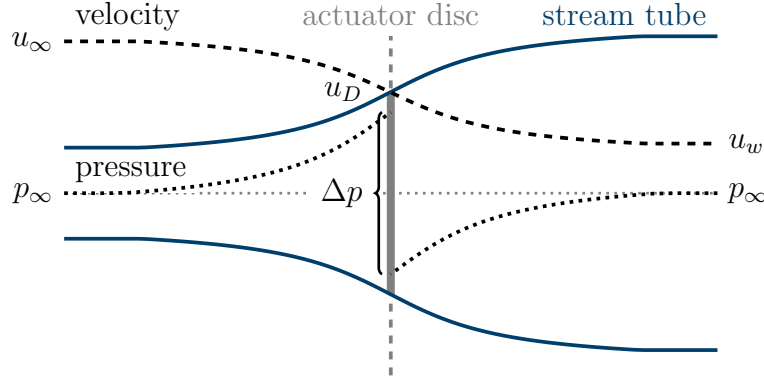


Figure 2.1: Stream tube showing the assumptions of the downstream change of the wind speed and pressure within the actuator disc concept (adapted from Burton et al. (2011)).

The power extracted by the turbine

$$P_{\text{WT}} = \dot{V} \Delta p \quad (2.2)$$

is given by the by the volumetric flow rate $\dot{V} = A_D u_D$ (which due to the incompressibility ($\rho = \text{const.}$, and $\dot{m} = \dot{V} \rho = \text{const.}$) is constant) with the area of the actuator disc A_D and the pressure loss over the actuator disc Δp . The pressure loss can be quantified by Bernoulli's equation,

$$\frac{1}{2} \rho u^2 + p + \rho g z = \text{const.} \quad (2.3)$$

with the velocity u , the pressure p , Earth's gravitational acceleration g , and the height z at a point of a streamline. Bernoulli's equation is constant without energy injection or extraction. However, the turbine is extracting energy and by this the equation becomes

$$\frac{1}{2} \rho u_\infty^2 + p_\infty + \rho g z = \frac{1}{2} \rho u_w^2 + p_\infty + \rho g z + \Delta p. \quad (2.4)$$

Hence, the pressure loss can be determined by $\Delta p = 1/2 \rho (u_\infty^2 - u_w^2)$ leading to the extracted power

$$P_{\text{WT}} = A_D u_D \frac{1}{2} \rho (u_\infty^2 - u_w^2) = 2 A_D \rho a (1 - a^2) u_\infty^3. \quad (2.5)$$

Based on this the power coefficient

$$c_P = \frac{P_{\text{WT}}}{P_{\text{wind}}} = \frac{2 A_D \rho a (1 - a)^2 u_\infty^3}{1/2 A_D \rho u_\infty^3} = 4 a (1 - a)^2 \quad (2.6)$$

is defined. Its maximum is given by $16/27 \approx 59.3\%$ (Betz's law) for an induction of $a = 1/3$ (Betz, 1927). This common non-dimensional power coefficient c_P is used in

combination with the tip speed ratio

$$\text{TSR} = \frac{2\pi Rn}{u_\infty} \quad (2.7)$$

as ratio of the blade tip speed $2\pi Rn$, with the rotor radius R and the rotational speed n , to the undisturbed wind speed u_∞ , to describe the wind turbine performance independently of its operation.

Blade element momentum theory

To estimate the local inflow conditions on the rotor, the blade element momentum theory is used. The blade element theory divides the blade into several individual sections and treats them as if they are experiencing two-dimensional inflow (Fig. 2.2).

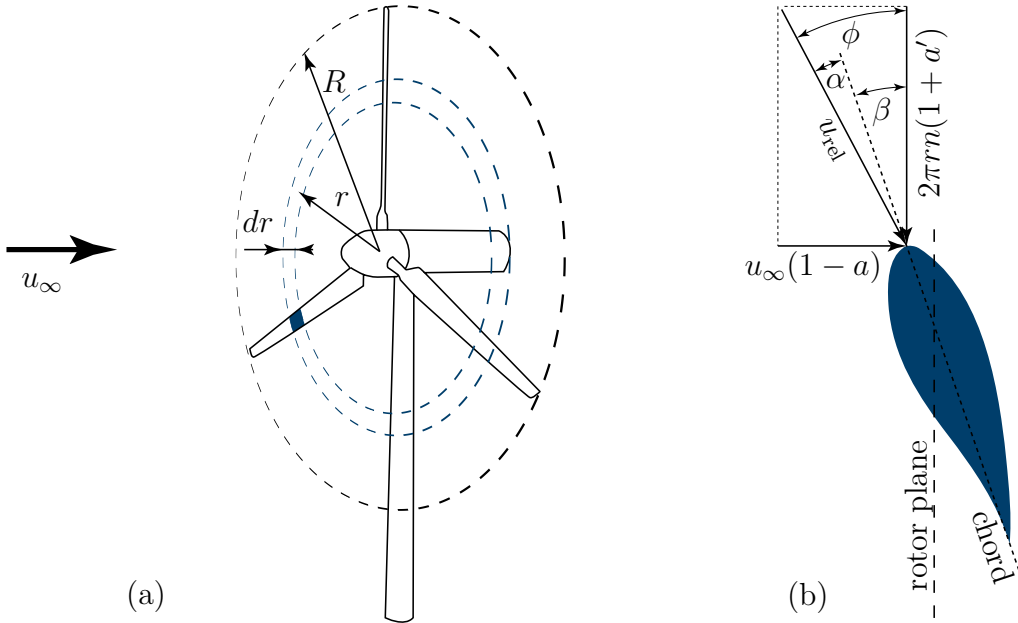


Figure 2.2: Definition of blade elements on the wind turbine (a) and local inflow conditions on a rotor blade element experiencing two-dimensional inflow (b).

The local angles of attack α are determined in an iterative process for every blade element. From the angle of attack the individual lift $F_L = 1/2 \rho u_{\text{rel}}^2 c dr c_L$ and drag forces $F_D = 1/2 \rho u_{\text{rel}}^2 c dr c_D$ are determined using the relative inflow velocity u_{rel} , the chord length c , the span wise extend of the blade element dr , and the tabular lift c_L and drag coefficients c_D of the individual airfoils. The relative inflow velocity

$$u_{\text{rel}} = \sqrt{(u_\infty^2(1-a)^2 + (2\pi rn)^2(1+a')^2)} \quad (2.8)$$

is given by the wind speed in the rotor plane $u_\infty(1-a)$ and the tangential velocity $2\pi rn$ at the span wise location r of the blade element considering the tangential velocity of

the wake $2\pi rna'$ and the tangential induction factor a' . The angle of attack $\alpha = \phi - \beta$ can then be calculated by the inflow angle

$$\phi = \arcsin \frac{u_\infty(1-a)}{u_{\text{rel}}} \quad (2.9)$$

and local blade twist angle β (including optional pitch angle of the blade) (Fig. 2.2 (b)).

The blade element rotor thrust

$$dT = 1/2\rho u_{\text{rel}}^2 Bc(c_L \cos \phi + c_D \sin \phi)dr \quad (2.10)$$

and rotor torque

$$dQ = 1/2\rho u_{\text{rel}}^2 Bcr(c_L \sin \phi - c_D \cos \phi)dr \quad (2.11)$$

are calculated with the number of Blades B .

The axial induction

$$\frac{a}{1-a} = \frac{\sigma_r c_x}{4 \sin^2 \phi} \quad (2.12)$$

and tangential induction

$$\frac{a'}{1+a'} = \frac{\sigma_r c_y}{4 \sin \phi \cos \phi}, \quad (2.13)$$

are given by the axial force coefficient $c_x = c_L \cos \phi + c_D \sin \phi$, the tangential force coefficient $c_y = c_L \sin \phi - c_D \cos \phi$ and the local solidity $\sigma_r = \frac{Bc}{2\pi rR}$. As the inflow angle ϕ depends on the induction and vice versa, the forces on the blade as well as the flow properties (induction and inflow angle) need to be calculated in an iterative process until the residuum is within a certain tolerance.

Wind turbine operation

In order to operate wind turbines optimally, e.g., to maximize energy production and reduce fatigue load, it is necessary to control the turbines. Various turbine operations methods can be applied. A recent review on control methods is given by Menezes et al. (2018). Nowadays wind turbines are mainly variable speed operated with optimal torque control in the partial load region and a collective pitch control in the full load region. For this operation method, the operational range of a wind turbine can be divided in five regions (Fig. 2.3):

- Region 1: out of operation - Below cut in wind speed ≈ 3 m/s. Due to the low wind speed no power is produced and the turbine is either stopped or idling.
- Region 2: partial load region - The power output is below the rated power and maximized by the optimal torque control. Here, the rotational speed is set by the generator torque

$$T = K_\lambda n^2. \quad (2.14)$$

The optimal torque is defined by the controller constant

$$K_\lambda = 1/2\rho\pi R^2 \frac{c_{P,\text{opt}}}{\text{TSR}^3}. \quad (2.15)$$

To obtain the controller constant for the optimal power coefficient $c_{P,\text{opt}}$, the optimal setting of TSR and blade pitch angle needs to be determined.

- Region 2.5: transition region (between partial and full load region) - The rotational speed has reached its rated value. The torque is slowly increased till it also reaches its rated value and by this the turbines rated power output. By this a smooth transition between region 2 and region 3 is achieved. Further, this allows for a separation of the partial load controller (optimal torque control) and the full load controller (collective pitch control) and prohibits an interference.
- Region 3: full load region - The turbine is operated at its rated power. The generator torque is set to the rated value. The rotational speed is kept constant by collective pitch control. To do so, all blades are pitched in the same way to change their aerodynamic efficiency and by this the aerodynamic torque. If the aerodynamic torque is larger than the generator torque, an acceleration of the rotor is the consequence and vice versa. By the manipulation of the aerodynamic efficiency besides the power output, the loads are limited as well.
- Region 4: out of operation - Above cut-out wind speed ≈ 25 m/s. Due to high wind speeds and in consequence high loads, the turbine is stopped or may be idling.

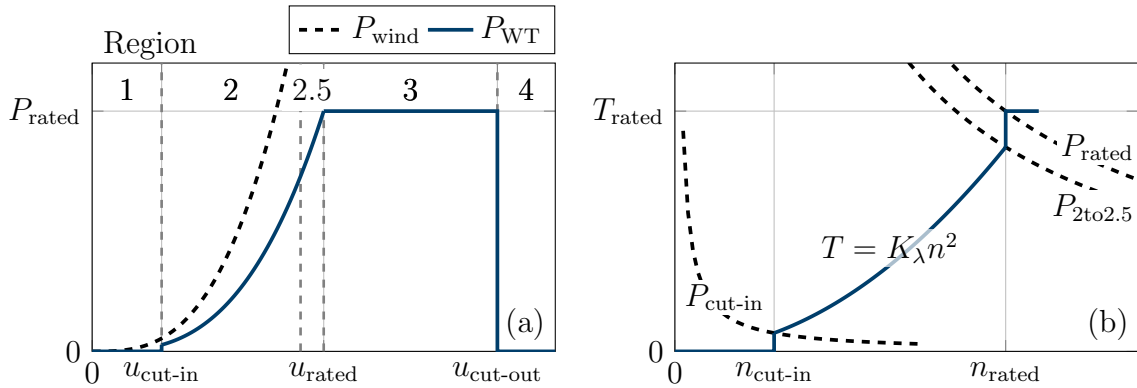


Figure 2.3: Wind turbine power curve with operational regions (a) and corresponding torque dependent on the rotational speed for optimal torque and collective pitch control (b).

Environmental conditions

Till here the descriptions were based on the assumption of laminar inflow. Due to turbulence a deviation from the theory can be expected. This is treated in industry standards as the IEC-standard 61400-1 (IEC, 2019). This IEC-standard defines design requirements for wind turbines and covers a simple standardized description of the

environmental conditions at the turbine location. In the framework of this thesis the most relevant environmental condition is the wind. Therefore, for this thesis relevant definitions are summarized in this section. Turbulence in detail is described in Sec. 2.2.

To describe different sites, wind turbine classes (I, II, and III) based on the annual average wind speed V_{ave} (10 m/s, 8.5 m/s, and 7.5 m/s) are defined. Additionally, turbulence categories (A+, A, B, and C) are given with reference turbulence intensities I_{ref} from 0.12 (C) to 0.18 (A+), where the turbulence intensity

$$TI = \frac{1}{\bar{u}} \sqrt{\frac{1}{3}(\sigma_u^2 + \sigma_v^2 + \sigma_w^2)} \quad (2.16)$$

(for isotropic turbulence simply σ_u/\bar{u}) is given by the standard deviation σ_i of the individual components i and the mean wind speed \bar{u} . Turbulence by the IEC-standard is described as the random variation of the wind speed from the 10 min mean value. It shall follow the Kaimal model (Kaimal et al., 1972), which is a parameterized form of the spectral behavior described by Kolmogorov (1941) (see Sec. 2.2).

The distribution of the 10 min mean wind speeds shall further follow a Rayleigh distribution

$$P_r(u_{hub}) = 1 - \exp\left(-\pi(u_{hub}/2u_{ave})^2\right) \quad (2.17)$$

dependent on the wind speed at hub height u_{hub} and the annual average wind speed u_{ave} . Depending on the 10 min mean wind speed the height resolved velocity and the 90% quantile of the turbulence intensity are given.

Besides these normal wind conditions, several extreme conditions with return periods from 1 year to 50 years are defined. Extreme events are, e.g., extreme velocities, extreme shear, extreme turbulence, extreme direction changes, or (which will be used in this thesis) gusts. The wind speed

$$u(t) = u_0 - 0.37u_{gust} \sin\left(\frac{3\pi t}{T}\right) \left(1 - \cos\left(\frac{2\pi t}{T}\right)\right) \quad (2.18)$$

for a gust event ($0 \leq t \leq T$) is given by the mean wind speed u_0 , the gust magnitude u_{gust} , and the gust duration T .

By means of these conditions, characteristic environmental influence parameters can be generated site unspecifically. Based on this standardized parameter space, turbines can be designed, but also investigated under reference conditions.

The environmental conditions influence the turbine dynamics, but an effect can also already be recognized in the mean values. Fig. 2.4 shows the effect of the turbulence intensity on a power curve (Kaiser et al., 2007).

The shown power curve is estimated based on the IEC-standard 61400-12 (IEC, 2017). For wind velocity bins of 0.5 m/s width, the mean wind speed and power output of 10 min mean values (u_{10min} , P_{10min}) are determined and define the power curve. It can be recognized that depending on the TI the individual power curves exhibit more or less power. This is caused by the non-linearity of this curve (cubic dependence of

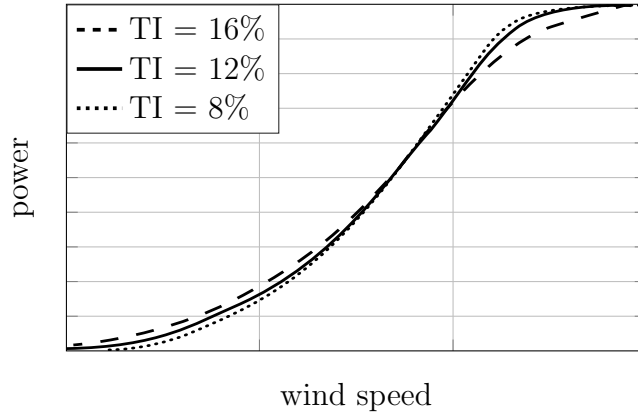


Figure 2.4: Wind turbine power curve for different turbulence intensities (adapted from Kaiser et al. (2007)).

power on wind speed). For low wind speeds, a high TI is beneficial, since negative gusts lead to a smaller power change (power reduction) than positive gusts (power increase), and thus the average power is higher. For high wind speeds close to the full load region, the beneficial effect of increased power for increased wind speed vanishes (as limited by the maximum power). Only a power decrease due to a reduced wind speed occurs. Hence, a lower TI is beneficial close to the full load region.

This is only a theoretic consequence of the cubic dependence of power on the wind speed. When turbulence is present there are further dynamic effects, which influence the turbine behavior (Milan et al., 2013). Hence, it is important to consider turbulence and its effect on wind turbines. A more detailed description of turbulence (besides the assumptions in the IEC-standard) will be given in the following section.

2.2 Turbulence

Turbulence is present in everyday life from large scale turbulence as experienced while commercial flights down to vortices occurring when mixing milk and coffee. It was already described by Leonardo da Vinci in his famous drawing (Fig. 2.5). Today, turbulence (turbulent wind) has also attracted attention as a source of renewable energy (Meneveau, 2019; Veers et al., 2019). Here a brief introduction to turbulence is given to provide a basis to understand the content of this thesis. This section is based on detailed descriptions as found in textbooks as Davidson (2004), Pope (2001), and Frisch (1995).

Energy cascade

Turbulence can be described as the fluctuation

$$u' = u(t) - \bar{u} \quad (2.19)$$



Figure 2.5: Leonardo da Vinci’s studies of water (da Vinci, 1510–1512).

of the velocity $u(t)$ of a fluid with the mean value \bar{u} . As turbulence is chaotic and non-reproducible, it is commonly described by the statistics of the fluctuations.

Leonardo da Vinci visually discovered, that big vortices break down into smaller vortices. Richardson (1922) introduced the idea of a cascading process (Fig. 2.6) where:

“Big whorls have little whorls
Which feed on their velocity,
And little whorls have lesser whorls
And so on to viscosity.”

In this cascade vortices of different size can be found. On the integral length scale L energy is introduced. The energy is then transferred to the smaller scales until it dissipates at the smallest scales, the Kolmogorov microscale

$$\eta = \left(\frac{\nu^3}{\epsilon} \right)^{1/4} \quad (2.20)$$

with the kinematic viscosity of the fluid ν and the dissipation rate ϵ . A further common scale to describe the flow is the Taylor microscale

$$\lambda_T = \sqrt{\frac{\langle u'^2 \rangle}{\left\langle \left(\frac{\partial u'}{\partial x} \right)^2 \right\rangle}}, \quad (2.21)$$

which defines the largest scale which is affected by the viscosity. The Taylor microscale marks the edge between the inertial sub-range, which is not affected by viscous dissipation, and the dissipation range where the dissipation to heat increases with decreasing scale.

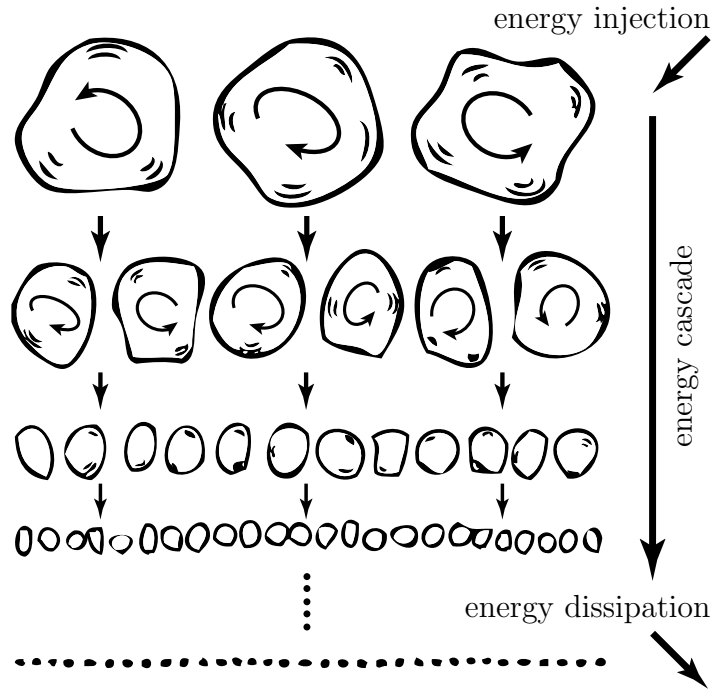


Figure 2.6: Cascading process from large scales to small scales (adapted from Frisch, 1995).

Characterizing the flow situation the Reynolds number

$$\text{Re} = \frac{ul}{\nu} \quad (2.22)$$

with the characteristic velocity u and the characteristic length scale l can be applied (Reynolds, 1883). The Reynolds number is given by the ratio of inertia to friction in a flow and thereby describes how turbulent the flow is. When inertia and friction are in equilibrium ($\text{Re} \approx 1$, which is the case for the Kolmogorov scale η), the flow is laminar, while for large Reynolds numbers ($\text{Re} \gg 1$), the flow becomes turbulent. Flow situations of different scale show a similar mechanical behavior as long as their Reynolds numbers are comparable. This became an important feature for investigations, as it allowed to undertake meaningful experiments on scaled down models with Reynolds numbers matching the application case. Wind tunnel experiments benefit extremely from this scalability. The introduced turbulent length scales (L , λ_T , and η) can be used as characteristic length scales. The dependency between these scales are given by

$$\text{Re} = \left(\frac{L}{\eta} \right)^{4/3}, \quad (2.23)$$

which indicates, that with increasing difference between the scales the Reynolds number becomes larger. Hence, a large Reynolds number corresponds to a large inertial

sub-range. The Taylor length scale is further used to define the characteristic (sometimes called turbulent Reynolds number) Taylor-scale Reynolds number

$$\text{Re}_{\lambda_T} = \frac{\sqrt{\langle u'^2 \rangle} \lambda_T}{\nu}. \quad (2.24)$$

The cascading process from largest to smallest scales was further quantified by Kolmogorov (1941). Considering the scale r dependent velocity increments

$$u_r = u(x+r) - u(x) \quad (2.25)$$

and making different assumptions:

- local isotropy - If the Reynolds number is sufficiently large, the directional information on the large scales (anisotropy on large scales) gets lost down the cascade ($\eta \ll r \ll L$) and the smallest scales are isotropic.
- first similarity - If the Reynolds number is sufficiently large, the structure functions $\langle u_r^n \rangle$ depend only on ϵ and ν .
- second similarity - For scales which are larger compared to the Kolmogorov scale ($r \gg \eta$), the structure functions are independent of ν and solely depend on the dissipation rate ϵ .

Hence, there is a range of scales r which is not affected by viscosity, the inertial sub-range (Fig. 2.7). Based on these assumptions, for the scales $\eta \ll r \ll L$ the second order structure function

$$\langle u_r^2 \rangle = f(\epsilon, r) = \beta \epsilon^{2/3} r^{2/3} \quad (2.26)$$

is a function of the scale r and the energy dissipation ϵ , which both need to have an exponent of $2/3$ when applying dimensional analysis. Kolmogorov (1941) assumed β to be an universal constant. Following the Wiener-Khinchin-theorem, the Fourier transform of the autocorrelation (equals the second order structure function $\langle u_r^2 \rangle$) corresponds to the energy spectra

$$E(k) = \alpha \epsilon^{2/3} k^{-5/3}. \quad (2.27)$$

Considering the wave number $k = 2\pi/r$ this gives Kolmogorov's $-5/3$ power law.

To characterize turbulence normally the structures in the flow are described depending on its spatial dimension. However, these structures (especially large structures) cannot always be measured spatially. Commonly, one point measurements are performed, recording the structures while passing the measurement location. To transfer information from this temporal space (time lag τ) to spatial space (length scale r), Taylor's hypothesis of frozen turbulence $r = \tau \bar{u}$ can be applied. It assumes, that the structures (size and characteristic parameters) stay constant (the structures are

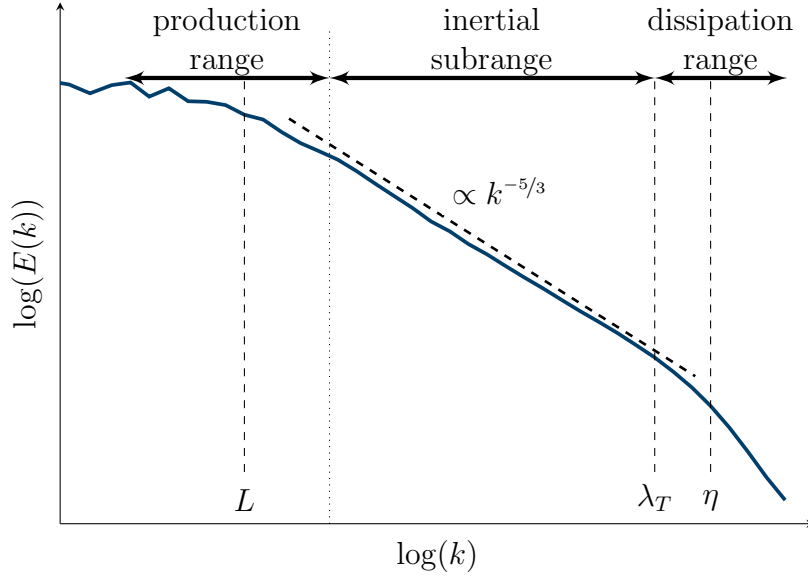


Figure 2.7: Energy spectra with characteristic scales and regions.

frozen) while passing the measurement location and are traveling with the mean wind speed \bar{u} . Accordingly, the velocity increments

$$u_\tau = u(t) - u(t + \tau) \quad (2.28)$$

can be defined by the time lag τ . However, Taylor's hypothesis of frozen turbulence is only valid for velocity fluctuations that are small compared to the mean wind speed.

Intermittency - increment statistics

The $-5/3$ power law was introduced by Kolmogorov (1941) assuming a dependence of the structure functions on the scale and the mean dissipation rate. However, in a system, which is strongly fluctuating, considering the global mean dissipation rate turned out to be an oversimplification. By a constant dissipation rate a Gaussian distribution of the velocity increments u_r is assumed.

When the distribution of the velocity increments of a turbulent flow is investigated on different scales, a deviation from the Gaussian distribution can be observed (Fig. 2.8). The smaller the scales, the more heavy-tailed the distribution, i.e., extreme events occur more often than expected by a Gaussian-distribution. This further means, that the small scales are less space filling than expected.

To adapt his theory, Kolmogorov (1962) assumed that the local dissipation rate ϵ_r is log-normal distributed for $r \ll L$ resulting in the variance of the local dissipation rate

$$\Lambda^2(r) = \Lambda_0^2 - \mu \ln(r/L) \quad (2.29)$$

with the universal constant μ (the intermittency factor) and the variable Λ_0 , which depends on the large scales. The dissipation rate fluctuations $\langle (\ln \epsilon_r)^2 \rangle \propto \Lambda^2(r)$ are

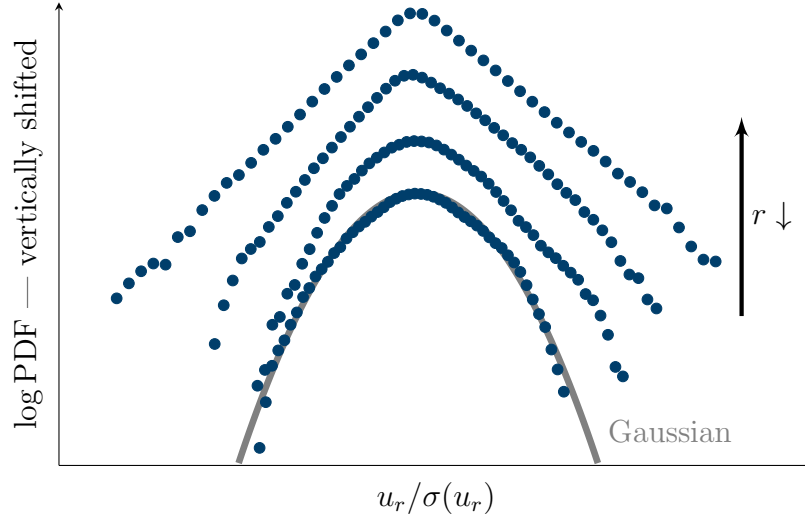


Figure 2.8: Probability density function (PDF) of the velocity increments u_r on different scales r .

connected to the shapefactor

$$\lambda^2 = \frac{1}{4} \ln \left(\frac{\langle u_r^4 \rangle}{3 \langle u_r^2 \rangle^2} \right), \quad (2.30)$$

which is calculated by the flatness $\langle u_r^4 \rangle / \langle u_r^2 \rangle^2$ of the velocity increments (Castaing et al., 1990; Chilla et al., 1996). In a semi-logarithmic presentation a linear decrease of the shapefactor λ^2 following $\lambda^2(\tau) \propto -\frac{\mu}{9} \ln \tau$ (Kolmogorov, 1962) is expected with the intermittency factor $\mu \approx 0.2$ to 0.3 for turbulent flow (Davidson, 2004; Arneodo et al., 1996). Morales et al. (2012) found an intermittency factor of 0.29 for atmospheric wind measured at the FINO 1 platform in the North Sea. By this, the shapefactor dependent on the scale τ combines the information contained in the structure functions up to fourth order.

To summarize, Kolmogorov (1962) modified the assumptions made in Kolmogorov (1941) ($\langle u_r^n \rangle = \beta_n (\epsilon r)^{n/3}$) by a correction term $(L/r)^{\mu/18(n(n-3))}$ considering a log-normal distribution of the local dissipation rate ϵ_r

$$\langle u_r^n \rangle = \beta_n \epsilon^{n/3} r^{n/3} (L/r)^{\mu/18(n(n-3))}. \quad (2.31)$$

This is resulting in the log-normal model of intermittency

$$\zeta_n = \frac{n}{3} - \frac{\mu}{18} (n(n-3)) \quad (2.32)$$

with the exponent ζ_n of the structure function $\langle u_r^n \rangle \propto r^{\zeta_n}$ and the intermittency factor μ . The first term ($\frac{n}{3}$) describes the exponent after Kolmogorov (1941) giving the $-5/3$ power law (without considering intermittency on the small scales). The second term ($-\frac{\mu}{18}(n(n-3))$) was added by Kolmogorov (1962) to consider a scale dependence of

the energy dissipation $\epsilon_r \neq \text{const.}$ by the intermittency factor μ . However, there are different turbulence models with different fluctuations of the energy dissipation ϵ_r (see Frisch, 1995).

Active grids - turbulence in the wind tunnel ¹

For many engineering problems the impact of turbulence is of high relevance. Quite often, like for wind turbines, the environmental conditions are highly unsteady. Thus, for a deeper scientific investigation it is desirable to remodel this interaction of turbulence and objects under reproducible laboratory conditions.

There is a special interest for small scales, as the statistics of the fluctuations change fundamentally with decreasing scale. Whereas nearly Gaussian distributed fluctuations are characterizing the large scales, the small scale fluctuations show heavy-tailed statistics, where extreme events with values of several standard deviations become much more likely than in a Gaussian field. Since atmospheric turbulence is driven on large scales larger than several km, even objects as big as wind turbines or houses are exposed to such small scale extreme events Böttcher and Peinke (2007). This challenges the desire to generate turbulent flow conditions, which resemble the atmospheric turbulence (which requires large Reynolds numbers) under laboratory conditions.

The first approach to generate turbulent flows in a wind tunnel was made by applying a simple regular grid to the nozzle (Simmons and Salter, 1934). Following this first grid experiment, different turbulence intensities and Taylor-scale Reynolds numbers were achieved by varying the grid mesh width, the tunnel cross sectional size, or the downstream position in the wind tunnel. For a long time such regular passive grids were the state of the art.

Such flows are restricted by several constraints. Firstly, in order to avoid the influence of incompressibility, laboratory wind speeds should not exceed several tens of meters per second. Secondly, the spatial extent of the large-scale velocity fluctuations which are generated at the grid, is mostly of the order of one meter (a fraction of the diameter of the wind tunnel), corresponding to the length scale over which a velocity-difference (shear) can be sustained. The biggest wind tunnels (Saddoughi and Veeravalli, 1994; Bourgoïn et al., 2018; DNW, 2021) allow to increase the Reynolds number up to the order of millions, still well below the values of atmospheric turbulence. Finally, the third quantity determining Re is the kinematic viscosity which can be lowered using different fluids, such as pressurized SF₆ (Bodenschatz et al., 2014), cryogenic N₂ (Viehweger, 1989) or low temperature He (Heslot et al., 1987; Niemela

¹The content presented in this section is published as part of Lars Neuhaus, Frederik Berger, Joachim Peinke, and Michael Hölling: Exploring the capabilities of active grids, *Experiments in Fluids*, 2021. and Lars Neuhaus, Wouter J. T. Bos, Michael Hölling, and Joachim Peinke: Generation of atmospheric turbulence with unprecedentedly large Reynolds-number in a wind tunnel, *Physical Review Letters*, 2020. L. Neuhaus carried out the measurements as well as the scientific analysis and wrote the manuscript. F. Berger helped to specify relevant inflow scenarios. W.J.T. Bos helped to interpret the results and wrote the section "kinetic energy balance". Michael Hölling and Joachim Peinke had a supervising function.

and Sreenivasan, 2006; Pietropinto et al., 2003). However, the use of such fluids largely complicates the experimental installations.

An additional way to increase the Reynolds number is to act directly on the nature of the velocity fluctuations. One possibility to do so is to vary the shape of the grid (Hurst and Vassilicos, 2007). A new concept to generate turbulence was shown by Makita (1991), when he introduced an active grid. The change from passive to actively controlled grid elements allowed to generate a variety of new flow conditions and to increase the Reynolds numbers significantly. This was a big step, as high Reynolds numbers could now be generated also in smaller wind tunnels. Many new experiments were initiated, which are summarized in a recent review by Mydlarski (2017). Alternating the excitation methods, grids are used (a) to generate homogeneous and isotropic turbulence (HIT) (see Mydlarski and Warhaft, 1996, 1998; Shen and Warhaft, 2000; Poorte and Biesheuvel, 2002; Larssen and Devenport, 2011; Hearst and Lavoie, 2015; Griffin et al., 2019; Cekli et al., 2015), (b) to create a defined shear flow in the wind tunnel (see Cekli and van de Water, 2010; Hearst and Ganapathisubramani, 2017), and (c) to reproduce atmospheric wind conditions either directly (see Reinke et al., 2017; Kröger et al., 2018a) or by their statistical properties (see Knebel et al., 2011; Good and Warhaft, 2011; Neuhaus et al., 2020).

The first active grid was operated in a *synchronous mode*, where all shafts are rotating with the same speed, but adjacent shafts in different directions. This allowed for an increase of the turbulence intensity. To further increase the turbulence intensity, a *single-random asynchronous mode* was introduced (Mydlarski and Warhaft, 1996). In contrast to the *synchronous mode*, the direction of the rotation was changed individually for the shafts after random time steps. However, the constant rotational speed caused a peak in the velocity spectrum. To reduce this effect, Mydlarski and Warhaft (1998) modified this mode by slightly different rotational speeds for the different shafts. This peak in the spectrum was completely eliminated by the *double-random asynchronous mode*, in which the rotational speed (negative and positive speeds are possible) and the duration are chosen randomly and individually for each shaft (Poorte and Biesheuvel, 2002). Hearst and Lavoie (2015) performed a comprehensive study of the initial conditions for active grid excitation and found that the highest homogeneity of the flow was generated by this *double-random asynchronous mode*.

All these methods focus exclusively on the movements of the active grid without direct reference to the resulting flows behind it. An alternative approach to this is a *blockage induced flow design*, which establishes a link between grid setting and generated flow. Therefore, the dependence of the wind velocity on the blockage (shaft angle) of the active grid is captured by a transfer function (see Knebel et al., 2011; Weitemeyer et al., 2013). Wind statistics were reproduced by randomly changing the global blockage of the grid according to the velocity distribution found in the atmosphere (see Knebel et al., 2011). Weitemeyer et al. (2013) introduced an operation of the active grid where they kept the global blockage constant, while changing the local blockage. This approach was further used for the direct reproduction of measured atmospheric wind by using a transfer function of the local blockage of the grid and the

velocity behind it (see Reinke et al., 2017). It was also applied to mimic atmospheric wind statistics by using stochastic processes as input for the motion of the shafts (see Kröger et al., 2018b; Neuhaus et al., 2020).

Additionally, grids which increased the degree of freedom for the excitation were built. Hearst and Lavoie (2015) installed two active grids with staggered flaps. An even higher variability can be found for the grid by Bodenschatz et al. (2014), which allows to control all flaps individually. This grid allows for greater control of the spatial velocity correlations (Griffin et al., 2019).

Apart from classical turbulence generation and wind field reproduction, approaches have been made to generate special flow structures as defined in the IEC 61400-1 standard for wind energy (IEC, 2019). One of these approaches with reduced complexity, uses a rotating bar, which blocks the wind while passing the wind tunnel cross section to generate inverse gusts (Neunaber and Braud, 2020). Another approach is based on a fan array at the test section inlet, for which the fans can be controlled individually allowing to create shears and gusts on time scales as small as a few seconds (Shirzadeh et al., 2020).

2.3 Stochastic analysis - The Langevin approach

Having started with statistic description of turbulence, in this section the stochastic analysis method applied in this thesis is presented. The motivation is to investigate a dynamic system and describe its fundamental behavior. A stochastic analysis is further done to be able to build a simple model of a complex system. To do so, probability theory is applied and model parameters are extracted from observations. This allows to quantify the behavior of the dynamic system and further to predict its behavior. The description of a dynamic system in this thesis is done by applying the Langevin approach (Anahua et al., 2008; Gottschall and Peinke, 2008).

The herein used Langevin approach goes back on the characterization of Brownian motion (Brown, 1828). First mathematical description were made amongst others by Einstein (1905). Langevin introduced a simpler description

$$\dot{y}(t) = D_1(y(t)) + \sqrt{D_2(y(t))}\Gamma_t \quad (2.33)$$

by using a deterministic $D_1(y(t))$ and a random $\sqrt{D_2(y(t))}\Gamma_t$ term with δ -correlated Gaussian white noise Γ_t (Lemons and Gythiel, 1997).

By the Gaussian white noise Γ_t , the process exhibits Markov property, i.e., it solely depends on the current state and is independent of the history of the process. This can be expressed by the conditional properties

$$p(y(t)|y(t-1), y(t-2)) = \frac{p(y(t), y(t-1), y(t-2))}{p(y(t-1), y(t-2))} = p(y(t)|y(t-1)) \quad (2.34)$$

(which is assumed to be comparable to $p(y(t)|y(t-1), \dots, y(0)) = p(y(t)|y(t-1))$). Hence, the process allows to define the next step by the current state and therefore

allows for an easy estimation of a trajectory, by the integrate of the Langevin equation

$$y(t + \tau) = y(t) + \tau D_1(y(t)) + \sqrt{\tau D_2(y(t))} \Gamma_t. \quad (2.35)$$

To describe a dynamic system by measured data, the drift coefficient D_1 and the diffusion coefficient D_2 need to be determined. To do so, the conditional moments

$$M_n(y, \tau) = \langle (y(t + \tau) - y(t))^n \rangle_{|y(t)=y} \quad (2.36)$$

of first and second order n are estimated for different time lags τ . For small time lags the linear slope of $M_n(\tau)$ is determined to extract the Kramers-Moyal coefficients

$$D_n(y) = \frac{1}{n!} \lim_{\tau \rightarrow 0} \frac{1}{\tau} M_n(y) \approx \frac{1}{n!} \frac{dM_n(y)}{d\tau}. \quad (2.37)$$

The Langevin equation is applied to different fields, as brain dynamics, turbulence, and stock markets (Friedrich et al., 2011). An application to wind energy is made by applying the equation to wind power data. Therefore, the dynamic process of a wind turbine is conditioned on two parameters, namely wind speed and power output. For the individual conditions, the Kramers-Moyal coefficients are determined, giving a two-dimensional plane, which is describing the dynamic system. Further, the so-called Langevin power curve (LPC) can be determined by the zero-crossings (stable fixed points) of the drift coefficient $D_1(P)$ in function of the power output for the individual wind speeds. This LPC holds further information compared to the conventional power curve, as it can have multiple stable fixed points per wind speed (and by this, e.g., detect failures (see Wächter et al. (2011))) and is less sensitive to turbulence.

In this way, the Langevin approach (as also described in Anahua et al. (2008) and Gottschall and Peinke (2008)) is applied to analyse model wind turbine data (Ch. 5). Further, the Langevin equation is used to generate random time series for the driving of the shafts of the active grid (Ch. 3) and the wind tunnel fans (Ch. 4). This is allowing for a stochastic turbulent-like excitation of the flow.

Chapter 3

Exploring the capabilities of active grids ¹

For wind energy research realistic atmospheric-like conditions are required in the wind tunnel. Active grids are commonly used in wind tunnels to generate turbulence with different characteristic features. In contrast to the common objective to generate turbulence with a very high Reynolds number, this chapter focuses on a method of *blockage induced flow design* for the generation of special flow structures. By the *blockage induced flow design*, flow structures can directly be imprinted on the corresponding scales by the active grid motion protocols. Particularly, the objective of this chapter is to investigate the underlying constraints of this excitation method. By a dimensionless consideration it is shown, how the layout of an active grid results in limitations in the scales of the generated flow structures. This knowledge can further be transferred from specific flow structures to turbulence generation. Consequently, the chapter is structured as follows. The experimental setup is presented (Sec. 3.1) and a method to tailor motion protocols by a transfer function of the active grid for different inflows is shown. Flow structures such as sinusoidal velocity variations, velocity steps, and single gusts are generated (Sec. 3.2) and the behavior of their limitations are discussed. The coherence of the flow is investigated in Sec. 3.2. The outcome of the investigation is further used to show a possible application to more complex turbulence time series (Sec. 3.3).

3.1 Experimental setup and flow generation

The measurements are done in Oldenburg in a Göttingen type wind tunnel with a 3 x 3 m² cross section and a length of 30 m. The wind tunnel can be operated in

¹The content presented in this chapter is published as Lars Neuhaus, Frederik Berger, Joachim Peinke, and Michael Hölling: Exploring the capabilities of active grids, Experiments in Fluids, 2021. L. Neuhaus carried out the measurements as well as the scientific analysis and wrote the manuscript. F. Berger helped to specify relevant inflow scenarios. Joachim Peinke and Michael Hölling had a supervising function.

an open (up to 32 m/s) or a closed (up to 42 m/s) test section configuration. Flow is generated by four fans with a power of 110 kW each and its temperature is kept constant by a cooling system with an effective cooling power of roughly 400 kW .

An active grid, $3 \times 3\text{ m}^2$, is mounted on the nozzle to manipulate the flow (Kröger et al., 2018a; ForWind, 2021) (Fig. 3.1). The active grid has 80 individually controllable shafts, each equipped with rectangular flaps. The mesh width M is 0.143 m . The local blockage can be altered by changing the angle of the flaps. By this the global blockage can be varied from 21% to 92%.

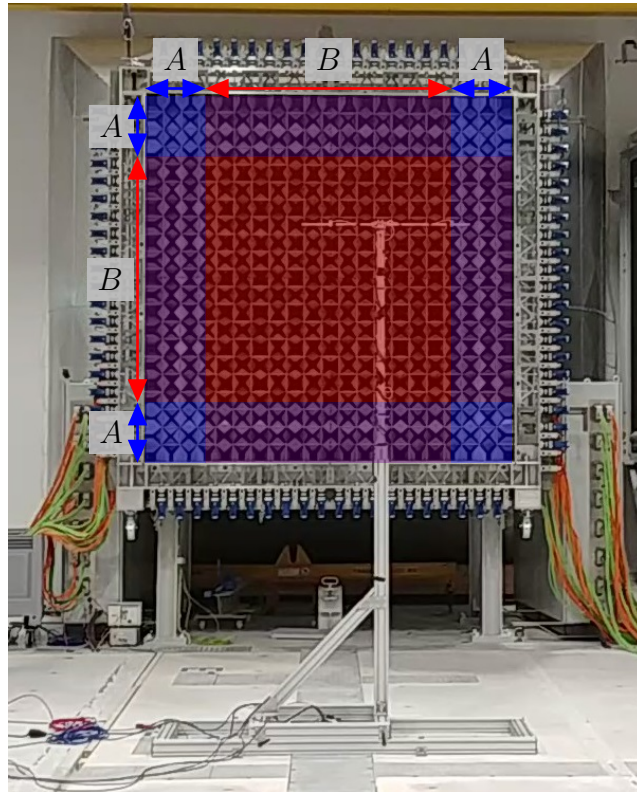


Figure 3.1: Active grid and hot-wire support. Example of A -shaft group and B -shaft group combination for defined flow generation on a $2 \times 2\text{ m}^2$ square in the center.

The active grid is controlled by a real time system that moves the shafts according to predefined shaft angle time series. Further, the protocol allows to generate user defined trigger signals, which ensure a temporal matching of repetitions.

Two different hot-wire setups with single and triple 1-D hot-wire 55P16-probes by Dantec Dynamics are used for the measurements. The hot-wires are mounted on a 3 m high support in the vertical center of the wind tunnel. A distance of $4.6\text{ m} \approx 32M$ downstream to the active grid was chosen as well as the open test section, see Fig. 3.1. One setup uses one single hot-wire on the centerline of the wind tunnel to characterize the flow structures (Sec. 3.2). The second setup with 3 hot-wires is used for the investigation of the coherence of the flow (Sec. 3.2). The hot-wire signals are sampled with a frequency of 20 kHz after being low pass filtered with 10 kHz .

Shaft motion groups

The active grid motion protocols are designed to ensure an easy and secure operation. Furthermore it is required that the flow must not be deflected and the global blockage of the active grid must remain constant.

To guarantee that no large redirection of the flow takes place, adjacent shafts are rotated in opposite directions, so that the flaps point in opposite directions. To keep the global blockage constant the active grid shafts are split in two groups, labeled with A and B (Fig. 3.1). For the first group (A) a shaft angle time series $\alpha(t)$ is prescribed. The second group (B) is following the shaft angle time series

$$\beta(t) = \arcsin((\sin(|\alpha(t)|) - 1 + x_{cb}) \cdot N_A/N_B), \quad (3.1)$$

which is given by the shaft angle time series $\alpha(t)$ and the corresponding number of shafts per group N_A and N_B ($N_B \geq N_A$). Due to this dependence (Eq. 3.1), the local blockage variations of both shaft groups compensate each other, so that the global blockage is approximately constant and can be set via the constant x_{cb} . In one group all shafts follow the same angle time series ($\alpha(t)$ or $\beta(t)$). However, adjacent shafts point in opposite directions (follow the angle time series with the opposite sign). In contrast to common excitation methods for the generation of high Reynolds number homogeneous isotropic turbulence (HIT), the shafts are not randomly rotating but flapping back and forth. The shaft angle is following a pre-defined time series (between $\alpha = 0^\circ$ and $|\alpha| = 90^\circ$) to dynamically change the local blockage (for a visual impression see ForWind, 2021).

Based on this *blockage induced flow design* approach, different combinations (patterns) of the two groups of shafts (A and B) can be picked. In this chapter a $2 \times 2 \text{ m}^2$ square pattern in the center is used, as shown in Fig. 3.1. As mentioned before, the motion pattern for the active grid keeps the global blockage approximately constant, allowing to neglect pumping effects of the wind tunnel and to assume a constant load on the fans. At the same time special shaft dynamics allow to generate special temporal structures of the flow downstream. In particular, transfer functions are used to predict special temporal structures. This methodology will be outlined in detail in the following.

Transfer function

To allow for the generation of defined flow conditions, the dependence between wind velocity behind the active grid and shaft angle (corresponding to the blockage) needs to be determined. This relation between active grid and resulting flow is expressed by a transfer function, which is determined with the following procedure (see also Reinke et al., 2017): For a constant wind tunnel fan speed (mean velocity) the shaft angle α is varied from 0° to 90° with a low angular velocity of $1^\circ/\text{s}$ (quasi-steady). The velocity $u(\alpha)$ is recorded at the position in the wind tunnel where later flow conditions should be created (here the centerline is used), as shown exemplarily in Fig. 3.2. From the

measurements the transfer function $u_{transfer}$ is extracted by a polynomial fit of 7th order for shaft angles α from 0° to 90° . The corresponding fluctuations are given by

$$u'(\alpha) = u(\alpha) - u_{transfer}(\alpha). \quad (3.2)$$

This procedure is repeated for different constant fan speeds u_{fan} . In this way a transfer function of

$$(\alpha, u_{fan}) \rightarrow (u_{transfer}(\alpha, u_{fan}), u'(\alpha, u_{fan})) \quad (3.3)$$

is obtained.

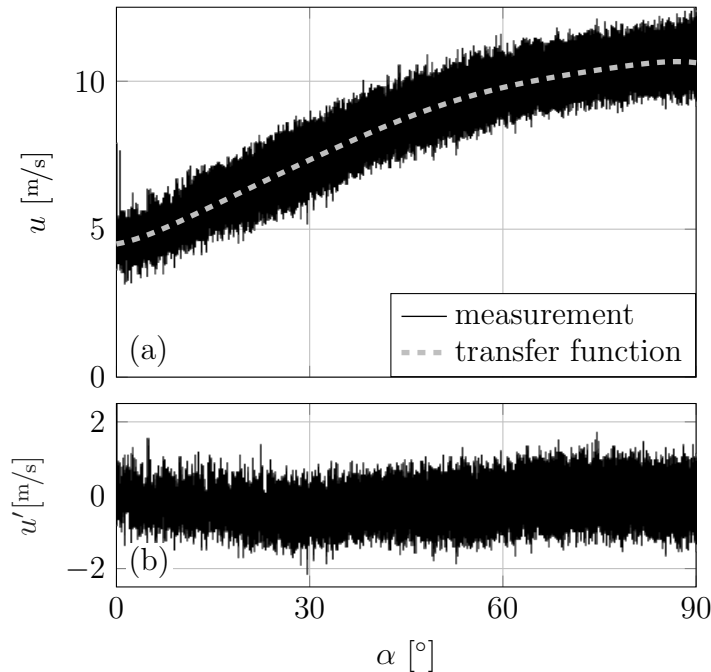


Figure 3.2: Exemplary time resolved velocity measurement dependent on the corresponding shaft angle α with extracted transfer function (a) and corresponding fluctuations u' (b) on the centerline behind the active grid.

The transfer function (Eq. 3.3) allows to predict a velocity time series and its statistics (e.g., distribution, power spectra, and increment statistics) by a corresponding time series for the shaft angle $\alpha(t)$. Following the method introduced by Reinke et al. (2017), for every sample point of the grid motion (10 to 20 ms) the mean wind speed is extracted from the transfer function. Subsequently, a velocity time series with high temporal resolution (20 kHz) is created by a cubic spline interpolation between these sample points. To this velocity time series high frequency fluctuations are added, which consist of 10 to 20 ms of $u'(\alpha)$ for each sample point. All this is also working vice versa. Having a velocity time series, the transfer function can be used to define the needed shaft angle time series $\alpha(t)$. This enables the generation of customized velocity time series.

A user-interface MATLAB-program was built to automatize the generation of active grid motion protocols including an automatized extraction of the transfer function of the active grid. This allows for an easy generation of new active grid motion protocols, tailored for the requested applications and inflows. In the next sections some examples are shown.

3.2 Generation of specific flow structures

Three different test cases are generated by the method just mentioned. The aim is to work out the range of validity of the *blockage induced flow design* method. First periodic sinusoidal velocity variations with different frequencies and amplitudes are studied. Subsequently, flow structures of upwards and downwards steps of the velocity are investigated. This step structure allows to see how symmetric the system behavior is. Finally gusts are studied, which provide information about the dependence of amplitude and symmetry on the frequency.

The corresponding motion protocols have to take into account the maximum rotational speed of the shafts and overshoots effects, which can be dampened by adjusting the acceleration and deceleration of the shaft motion. The single cases are repeated several times (sinusoidal velocity variation and gusts: 50 repetitions; velocity steps: 20 repetitions). The ensemble average of the centerline measurements are used for the detailed analysis.

Sinusoidal velocity variation

The first case of a sinusoidal velocity variation can be used to test objects under the influence of a simple periodic flow. To investigate the operation range of the active grid different frequencies and amplitudes are used.

Measurements are undertaken for six different frequencies from 0.5 Hz to 10 Hz and seven different aimed amplitudes \hat{u}_{aim} from 0.5 m/s to 3 m/s for mean wind speeds of 6 m/s and 12 m/s with amplitudes from 1 m/s to 6 m/s (Tab. 3.1). The highest amplitudes are not investigated for the higher frequencies, as the loads for the active grid are too high for a secure operation.

In Fig. 3.3 the averaged velocity signals of three cases with the same aimed amplitude \hat{u}_{aim} of 2.5 m/s and frequencies of 0.5 Hz, 2 Hz, and 4 Hz are shown. The solid lines correspond to the ensemble averages, the envelopes indicate its standard deviations, and the dashed black lines represent the corresponding sine fits of the ensemble averages.

For all frequencies a sinusoidal velocity variation can be recognized. The deviations from an ideal sine wave are small. The relatively small standard deviation is quite constant over the period and indicates a good reproducibility. For the lowest frequency of 0.5 Hz the sinusoidal motion follows the expectations. For the higher frequencies the aimed amplitude of 2.5 m/s is not reached.

Table 3.1: Investigated sine frequency and amplitude combinations.

\bar{u} [m/s]	f [Hz]	\hat{u}_{aim} [m/s]
6	0.5	0.5, 0.75, 1, 1.5, 2, 2.5, 3
	1	0.5, 0.75, 1, 1.5, 2, 2.5, 3
	2	0.5, 0.75, 1, 1.5, 2, 2.5, 3
	4	0.5, 0.75, 1, 1.5, 2, 2.5
	5	0.5, 0.75, 1, 1.5, 2
	10	0.5, 0.75, 1, 1.5, 2
12	0.5	1, 1.5, 2, 3, 4, 5, 6
	1	1, 1.5, 2, 3, 4
	2	1, 1.5, 2, 3, 4
	4	1, 1.5, 2, 3, 4
	5	1, 1.5, 2, 3, 4
	10	1, 1.5, 2, 3, 4

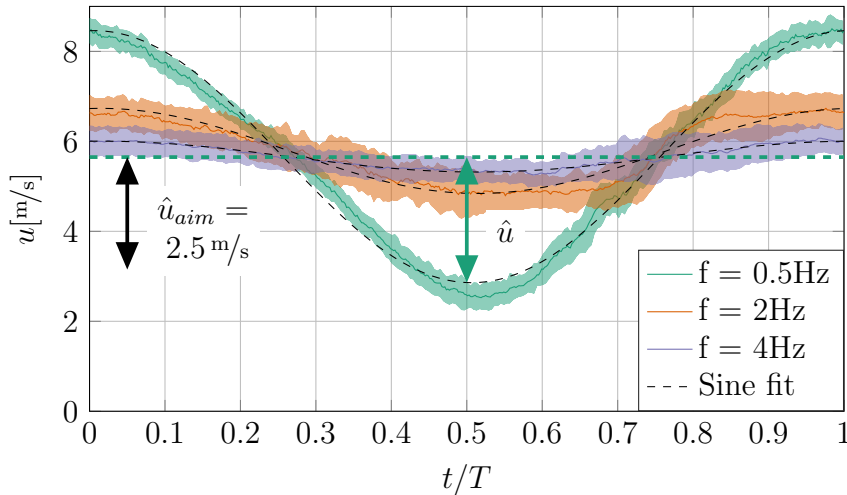


Figure 3.3: Ensemble average, ensemble standard deviation (envelope), and sine fit of generated sinusoidal velocity variations for frequencies of 0.5 Hz, 2 Hz, and 4 Hz (corresponding to reduced frequencies k_{red} of 0.04, 0.15, and 0.31), with an aimed amplitude \hat{u}_{aim} of 2.5 m/s.

To quantify the quality of the sinusoidal variation, the root mean square error (RMSE) is estimated between the measurement and the sine fit, which then is normalized by the estimated amplitude \hat{u} . The threshold for good quality is here the normalized RMSE of a flat line compared to a sine wave ($RMSE = \sqrt{0.5}$). A flat line corresponds to no signal, and signals with a larger RMSE than the one of no signal are considered as being of poor quality. Values below this threshold indicate a high quality sinusoidal velocity variation, whereas values above this threshold may not show a sinusoidal velocity fluctuation with the imprinted frequency or the imprinted flow

may be dominated by noise (i.e., natural velocity fluctuations).

The dynamic response of the flow, and hence the quality of the sinusoidal velocity variation, seem to be connected to the overflow time of the flaps. This is one central finding of this work and discussed next.

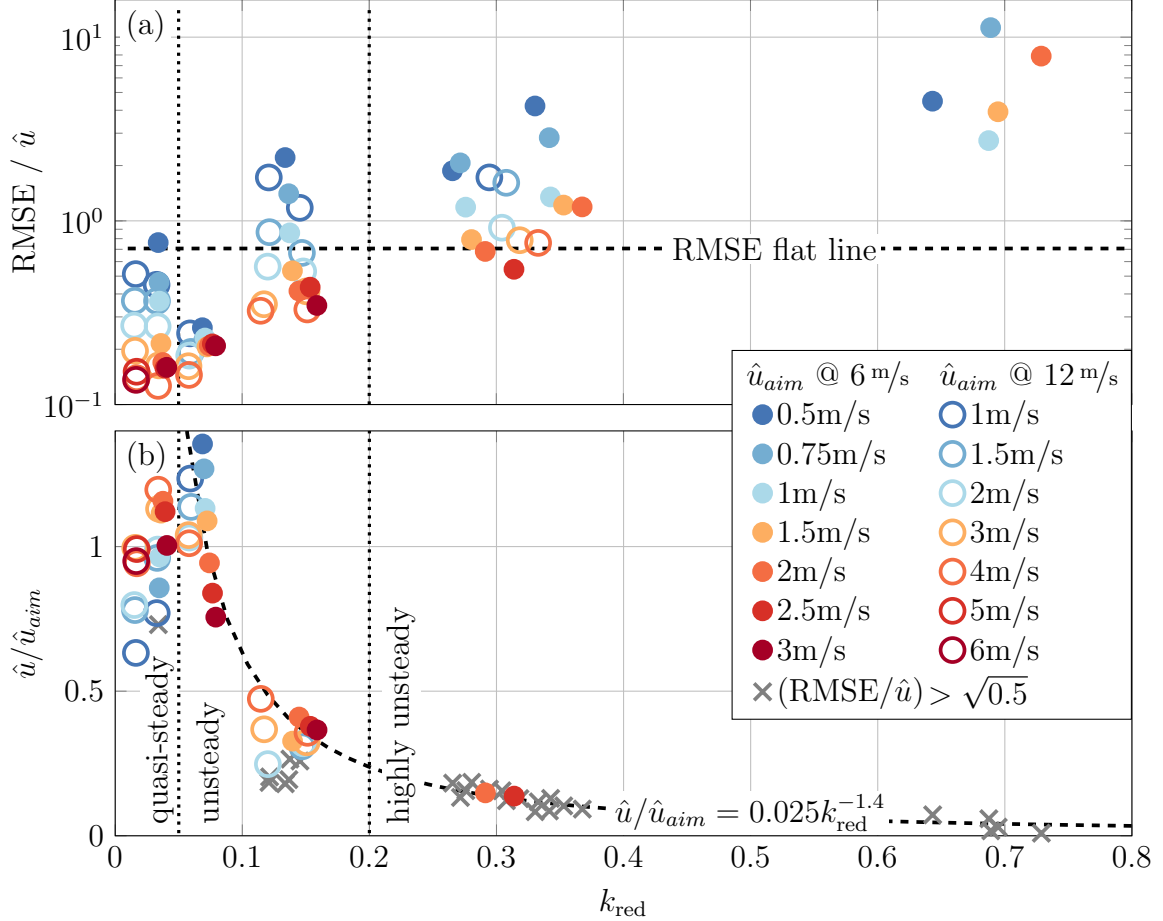


Figure 3.4: Root mean square error (RMSE) normalized by the measured amplitude (a) and amplitude ratio (b) dependent on the reduced frequency k_{red} .

The overflow time is commonly expressed by the reduced frequency

$$k_{\text{red}} = lf\pi/\bar{u}, \quad (3.4)$$

of the imprinted sinusoidal frequency f the diagonal of the flaps $l \approx 0.14$ m and the mean wind velocity \bar{u} . The resulting normalized RMSE is shown dependent on this reduced frequency in a semi-log presentation (Fig. 3.4 (a)). The best results are found for low reduced frequencies and high amplitudes. With increasing reduced frequency, the normalized RMSE increases linearly in the semi-logarithmic presentation. The normalized RMSE of the lower amplitudes is consistently larger than the one of the high amplitudes. According to the introduced threshold of $\sqrt{0.5}$ (marked by a dashed

line in Fig. 3.4 (a)) all cases of Fig. 3.3 show a good quality. Normalized RMSE of 0.16 for 0.5 Hz, 0.44 for 2 Hz, and 0.54 for 4 Hz are found, which is consistent with the visual impression, as for all cases the sinusoidal velocity variations can be recognized.

Besides the sinusoidal form, which is quantified by the normalized RMSE, the aimed amplitudes \hat{u}_{aim} are compared with the measured ones \hat{u} by the ratio of both amplitudes (Fig. 3.4 (b)). Sinusoidal velocity variations with poor quality are marked by an X-symbol. The dependence of this amplitude ratio can be divided into three regions. Up to approximately $k_{red} = 0.075$ the aimed amplitude can be achieved. In the second region for $0.075 < k_{red} < 0.2$, the amplitude is damped to 20% to 50% of the aimed amplitude. For larger reduced frequencies ($k_{red} > 0.2$), the amplitude is strongly damped to less than 20% up to cases where hardly any sinusoidal motion can be detected. Together with the RMSE results these regions can be linked to the different states of the flow described, namely, quasi-steady state ($k_{red} \leq 0.05$), unsteady state ($k_{red} > 0.05$), and highly unsteady state ($k_{red} > 0.2$). Further, the reduced frequency region with a low damping of the amplitude also corresponds to the region with a good quality (Fig. 3.4 (a)).

For $k_{red} \geq 0.075$ it is found that the amplitudes decay with a power law $\hat{u}/\hat{u}_{aim} = 0.025k_{red}^{-1.4}$. To verify this result, a second measurement with twice the mean wind speed ($\bar{u} = 12 \text{ m/s}$) was done (Tab. 3.1). All results of this measurement fit well to the former results with lower wind speed.

In general, it can be recognized, that for the quasi-steady state and up to $k_{red} = 0.075$ the transfer function (Sec. 3.1) can be used to directly design the flow. For higher reduced frequencies the imprintable amplitude is lower than expected from the transfer function. Hence, the quasi-steady transfer function needs to be adapted for dynamic effects to compensate the damping of the amplitude for reduced frequencies $k_{red} > 0.075$ and may not be applicable for very high reduced frequencies of $k_{red} > 0.3$ (Sec. 3.3).

Velocity step

To further understand the dynamics of flow excitations, the active grid is used to generate jumps between two flow conditions. Again the aim is to determine the limits of producible velocity steps with the active grid and to study steps with different amplitudes. It is distinguished between a velocity increase and decrease and differences in the dynamic response of the flow are investigated.

Measurements are undertaken for nine different step amplitudes from 0.5 m/s to 6 m/s and a lower wind speed level of 5 m/s . Fig. 3.5 shows the ensemble average of the smoothed and downsampled 20 repetitions (solid line) and its standard deviations (envelope).

Velocity step amplitudes up to roughly 6 m/s are possible and are well reproduced. For the small step amplitudes ($\leq 2.5 \text{ m/s}$) fluctuations (damped oscillations) after the upwards and downwards steps can be recognized. An asymmetric behaviour is found for larger steps amplitudes. Here large fluctuations (damped oscillations) are found after the downwards step, whereas hardly any fluctuation can be recognized after the

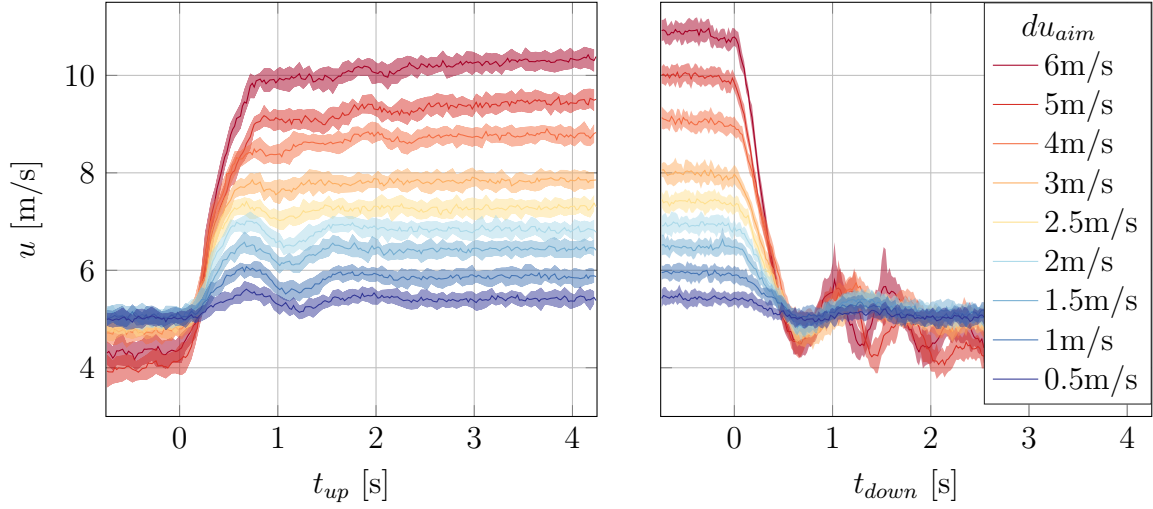


Figure 3.5: Smoothed and downsampled ensemble average (solid lines) and its standard deviation (envelope) of the velocity steps generated by the active grid.

upwards step.

To quantify the steps, the velocity increments $du = u(t+dt) - u(t)$ for different temporal increments dt are determined. Per temporal increment the maximum (upwards step) and minimum (downwards step) velocity increment is determined. Fig. 3.6 shows the temporal increment dt after which the absolute value of the maximum/minimum velocity increment exceeds 80% and 90% of the aimed step amplitude du_{aim} . This is giving a rough measure of the time needed to complete the steps of different amplitudes.

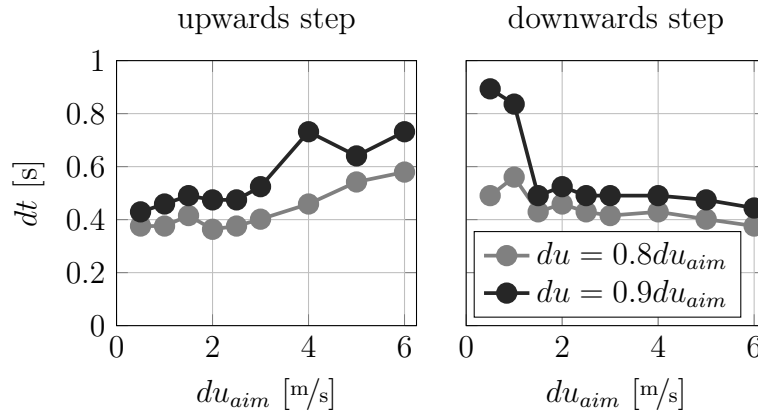


Figure 3.6: Time increments dt to reach 80% and 90% of the aimed step amplitude du_{aim} dependent on the aimed step amplitude du_{aim} for upwards and downwards steps.

For the upwards step it is found, that larger step amplitudes need longer time to reach the aimed value. Step amplitudes below 3 m/s need less than 0.5 s to reach 90% of the aimed value. The largest step amplitude takes roughly 0.75 s to reach 90% of

the aimed value.

For the downward step the opposite dependence can be found. Steps above 1 m/s are completed to 90% after roughly 0.5 s. Smaller step amplitudes take way longer and up to 0.9 s.

To summarize the step measurements, it can be seen that it is possible to create different velocity steps with the active grid. Very fast and large velocity steps up to 6 m/s within 0.75 s can be generated.²

Fluctuations of the velocity after an upwards or downwards step may occur. For very large step amplitudes a slight drift of the velocity and a lower wind speed of the lower level was observed, which may be caused by the rapid change of the local blockage to which the whole wind tunnel has to adapt (Fig. 3.5). Interestingly, the time for the completion of the step depends not only on the step amplitude, but also on the sign of the step. Large steps are completed faster for a velocity decrease, whereas small step amplitudes are completed faster for a velocity increase. This shows some asymmetry between the dynamic response of the flow and the velocity manipulation by the active grid.

Gust

Here gusts are investigated as a third flow structure and use the IEC-standard 61400-1 (IEC, 2019) (see Sec. 2.1). The standard originates from the field of wind energy and it is used to define test cases for wind turbine design. Different amplitudes and duration are tested for the gust.

The equation for the temporal change of a gust

$$u = u_0 - 0.37u_{gust} \sin\left(\frac{3\pi t}{2T_{peak}}\right) \left(1 - \cos\left(\frac{2\pi t}{2T_{peak}}\right)\right) \quad (3.5)$$

is given by the IEC-standard with the mean wind speed u_0 the gust magnitude u_{gust} and the gust peak duration T_{peak} . However, for wind tunnel experiments a scaling needs to be considered, leading to reduced T_{peak} and velocity, depending on the application. These parameters are used as an input for the active grid. Four peak durations from 0.25 s to 2 s and four different gust magnitudes u_{gust} from 2 m/s to 5 m/s are tested for a mean wind speed u_0 of 6.25 m/s.

Four exemplary measurements are shown in Fig. 3.7 with the same aimed gust magnitude $u_{gust,aim} = 4$ m/s and with different peak duration of $T_{peak,aim}$, from 0.25 s to 2 s. The dashed line indicates an ideal gust (Eq. 3.5). It can be seen, that the measured peak magnitude u_{gust} gets damped for shorter aimed peak duration $T_{peak,aim}$. For $T_{peak,aim} \leq 0.5$ s, the measured peak duration T_{peak} gets longer than $T_{peak,aim}$. In

²This is in good agreement with the findings from the sinusoidal velocity variation. For a reduced frequency of $k_{red} = 0.075$ and a mean wind speed of 5 m/s the by amplitude damping unaffected frequency is found for roughly 0.83 Hz corresponding to a period time of 1.2 s. Assuming the time to complete an upwards step to correspond to half a period, the resulting time to complete an unaffected upwards step is found to be in the order of 0.6 s, which is in the observed range.

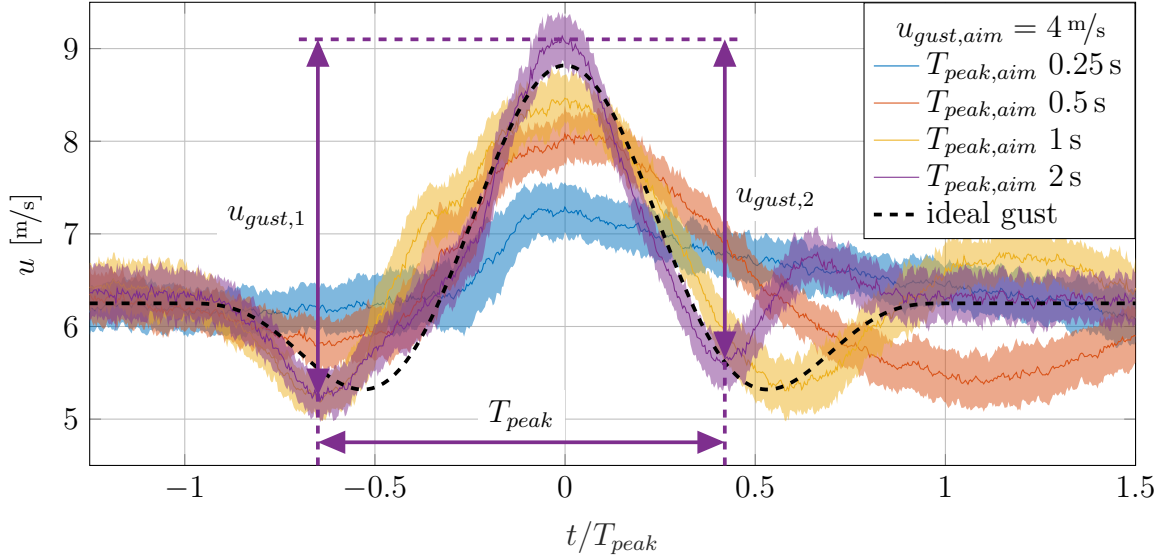


Figure 3.7: Ensemble average (solid lines) and its standard deviation (envelope) of gusts generated by the active grid with aimed duration from $T_{peak,aim} = 0.25$ s to 2 s compared to an ideal gust (Eq. 3.5). For a better visualization, the gust peak is shifted to $t = 0$.

particular, the decreasing part with a second dip occurs delayed compared to the expectation after Eq. 3.5. For longer aimed peak duration ($T_{peak,aim} \geq 1$ s) the gust shapes are close to the one expected.

To quantify the individual cases, the peak duration T_{peak} and the gust magnitude u_{gust} are estimated from the measurements according to Fig. 3.7. The peak duration T_{peak} is determined by the time difference between the two dips. The gust magnitude $u_{gust} = (u_{gust,1} + u_{gust,2})/2$ is estimated by the mean of the velocity difference between first dip and peak $u_{gust,1}$ and second dip and peak $u_{gust,2}$.

These characterising quantities are studied dependent on the inverse of the aimed peak duration $1/T_{peak,aim}$, which is proportional to the reduced frequency (Eq. 3.4), but can not be explicitly defined due to the superposition of different frequencies.

Fig. 3.8 (a) shows which duration T_{peak} can be achieved. A saturation at a peak duration of $T_{peak} = 0.8$ s is found. Shorter peak durations can not be obtained with the used active grid and T_{peak} starts to increase for faster excitations.

In Fig. 3.8 (b) it is shown how the gust magnitude gets damped, which is in accordance with the observation for the sinusoidal velocity variation. For the shortest aimed peak duration a comparable damping as in the unsteady state region can be observed. Besides this qualitative result, a direct quantitative comparison is not possible.

In addition to the amplitude and the duration of the gust, the symmetry of the gust is influenced if the aimed peak duration becomes shorter. To quantify the symmetry of the gust the correlation of the right side and the left side of the gust is determined (Fig. 3.8 (c)). Here the maximum of the measured signal is used to define left and right side. For low inverse aimed peak duration ($1/T_{peak,aim} \leq 1$ 1/s) high correlations

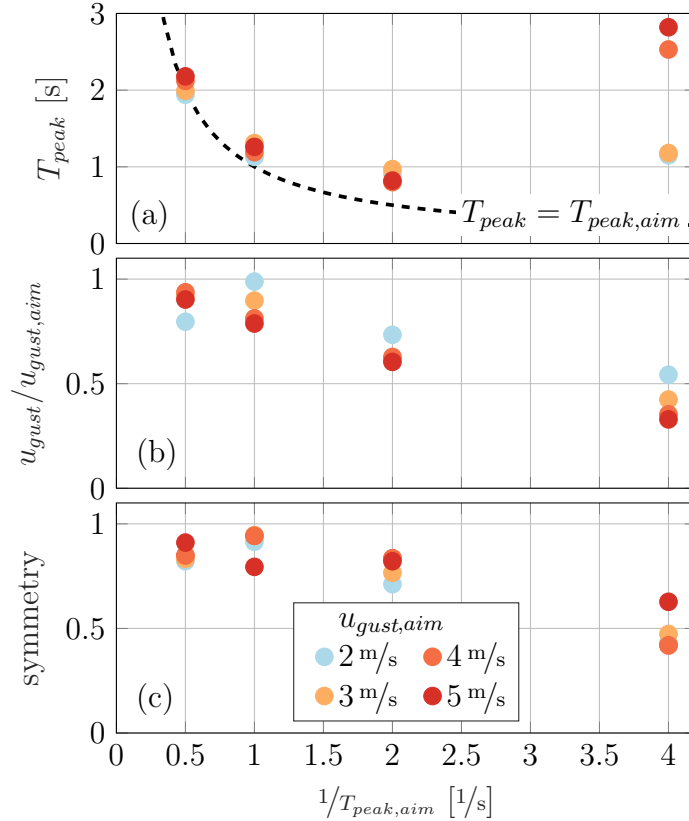


Figure 3.8: Measured peak duration T_{peak} (a), normalized measured gust magnitudes $u_{gust}/u_{gust,aim}$ (b), and correlation of left and right side of the peak (symmetry) (c) in dependence of the inverse aimed peak duration $1/T_{peak,aim}$.

(> 80%) are found. The correlation is reduced for higher inverse aimed peak duration. For the highest inverse aimed peak duration, the correlation is strongly reduced to values below 50% and only for the largest gust magnitude the correlation is found at roughly 65%.

To conclude the gust investigations, it can be seen that high magnitudes up to $u_{gust} = 5 \text{ m/s}$ were achieved. The shortest peak duration was found to be in the order of $T_{peak} = 0.8 \text{ s}$. This is in good agreement with the findings from the velocity step, where steps (corresponding to half a gust peak) were successfully generated on comparable time scales (Sec. 3.2).

For aimed peak duration of $T_{peak,aim} \geq 0.5 \text{ s}$ well-shaped gusts with symmetry correlations above 70% can be created. The gusts are repeated with some temporal spacing between each other. Hence, the flow has time to adapt to the undisturbed case (in contrast to the sinusoidal velocity variation). This revealed an increasing asymmetric response of the flow for decreasing aimed peak duration. For short aimed peak duration ($T_{peak,aim} \leq 0.5 \text{ s}$), the gusts exhibit longer peak duration than aimed for. However, it is possible to create comparatively short and strong gusts, which are close to the shape defined by the IEC-standard.

Coherence

The different generated flows were characterized by one single point measurement on the centerline of the tunnel. For an application it is important to ensure a similar flow behavior on a certain cross section.

To study the coherence of the generated flows, multiple transversal shifted positions are investigated. In total 12 hot-wire positions are considered ranging from the centerline to a transversal shifted position of 0.99 m with a spacing of 0.09 m. There to, three hot-wire probes are used with a transversal spacing of 36 cm, which are shifted collectively (Fig. 3.9). Here a fully symmetric flow over the cross section is assumed, as the active grid and the active grid motion are symmetric to the center point. Hence, the transversal shift by roughly 1 m should give a valid approximation of the coherence of the flow in a cross section of the size of $2 \times 2 \text{ m}^2$.

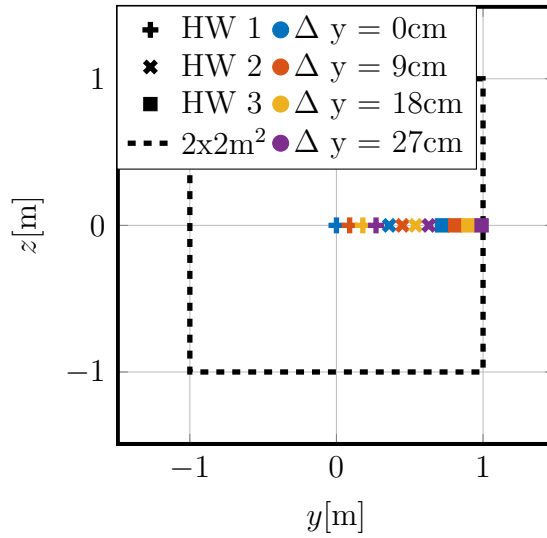


Figure 3.9: Positions of hot-wires for coherence measurements.

For the different single events a few representative cases are measured for all 12 positions. Frequencies of 0.5 Hz with 3 m/s , 1 Hz with an amplitude of 0.5 m/s , and 2 Hz with 3 m/s are investigated for the sinusoidal velocity variation. Large and small velocity steps (1 and 6 m/s) upwards and downwards are considered. For the gusts, peak durations of 0.5, 1, and 2 s with a gust magnitude of 5 m/s for the shortest duration and 4 m/s for the two longer durations are investigated. The correlations

$$\rho_{\text{corr}}(y) = \frac{\sum u'(t, y)u'(t, y = 0)}{\sqrt{\sum (u'(t, y))^2 \sum (u'(t, y = 0))^2}} \quad (3.6)$$

of the ensemble average of the different positions ($u'(t, y) = u(t, y) - \bar{u}(y)$) with the ensemble average of the centerline ($u'(t, y = 0) = u(t, y = 0) - \bar{u}(y = 0)$) are determined for all representative cases (Fig. 3.10).

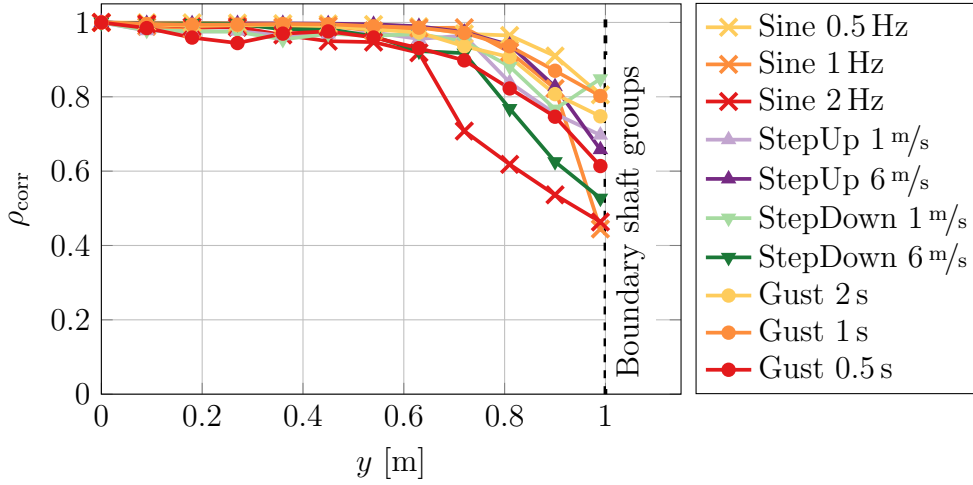


Figure 3.10: Correlation of the ensemble average of different generated flows measured at transversal shifted positions with the corresponding measurement at the centerline.

The correlations in the center region ($y \leq 0.63$ m) are very high (> 0.91). For the positions farther outside ($y \geq 0.72$ m) the correlations are reduced. The correlation for the outer position ($y = 0.99$ m) is found to be still above 0.5 for most cases. For some cases correlations up to 0.8 can be found for the outer measured position. The lowest correlations are found for fast and high velocity variations (StepDown 6 m/s and Sine 2 Hz). For slow variations the highest correlations are found (Sine 0.5 Hz).

The presented method allows for the generation of flow structures with a good coherence on a large area corresponding to the region of one shaft motion group. Only measurements at the outer positions show lower correlations, which is to be expected as they are located in the shear layer between the different shaft motion groups. On a large cross section (1.25×1.25 m²) very high correlations (≥ 0.9) can be found. Preliminary investigations on the downstream development of a single gust on the centerline showed a robust behavior of the structures over several meters in the stream-wise direction (see Fig. 3.11).

3.3 Application to turbulence

A clear dependence of the excitable frequencies on the reduced frequency was found. The amplitude damping, which occurs for high reduced frequencies, needs to be considered in the generation process.

Besides the investigation of specific frequencies and a superposition of different frequencies (gust) also the effect of a broad band excitation is of interest. The findings from the sinusoidal velocity variation are applied to the generation of fully developed turbulence in the wind tunnel by an active grid. The goal is to generate a flow that satisfies the $-5/3$ power law of Kolmogorov (1941) over a wide range directly through the motion protocol of the active grid. Therefore, a 10 min turbulent time series is

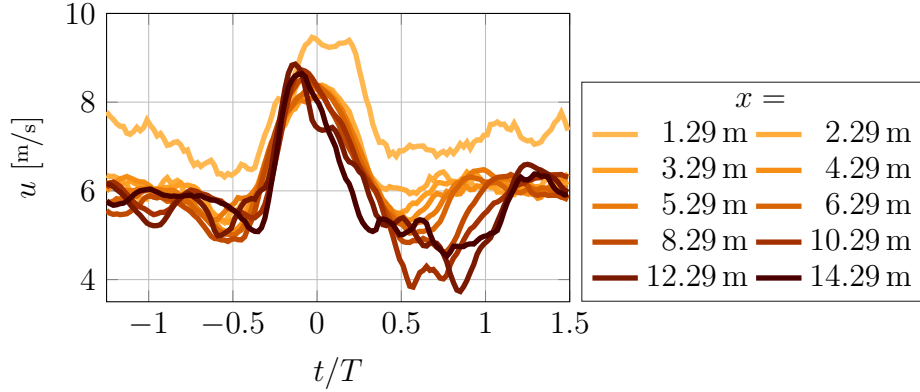


Figure 3.11: Downstream transition of a gust generated by the active grid.

generated by a broad band excitation based on a stochastic process exhibiting a power law decay (Ornstein-Uhlenbeck process (OU)) as presented by Neuhaus et al. (2020). By the quasi-steady transfer function (Sec. 3.1) the expected velocity time series and the corresponding expected spectra are determined. This expected spectrum (red curve) and the measured spectrum (blue curve) dependent on the reduced frequency are shown in Fig. 3.12 (a) in a double logarithmic presentation.

Three regions can be identified in the power spectra. In the first region for reduced frequencies up to $k_{\text{red}} \leq 0.075$, the measured power spectra behaves as expected and follows the $-5/3$ power law. From $k_{\text{red}} = 0.075$ to $k_{\text{red}} = 0.7$, a deviation from the power law and the expected power spectra can be observed. Hence, the active grid motion based on the Ornstein-Uhlenbeck process is not exciting the flow in the expected way, as already observed for the sinusoidal velocity variation (Sec. 3.2). For higher reduced frequencies ($k_{\text{red}} \geq 0.7$), the measured power matches the expected one again. This is caused by the different excitation of the flow for these frequencies, as the fluctuations are excited by the grid flap design and not by an active motion of the shafts. Hence, even the active excitation of complex flows is damped in the same region ($k_{\text{red}} > 0.075$) as shown for the simple sinusoidal inflow cases.

The quotient of the measured spectrum to the expected one (OU excitation) is shown in Fig. 3.12 (b) in a semi-logarithmic presentation. It can be recognized, that the measured spectra (gray line) gets damped not only in the same region but in the same way as the amplitudes of the sinusoidal inflow (markers and dashed line from Fig. 3.4 (b)) get damped. This comparability helps to understand the excitation by the active grid and the dynamic response of the flow to its motion.

To overcome this limitation, a first simple approach is shown exemplarily for the broad band excitation. Therefore, a stochastic process without a power law decay in the damping region (white noise (WN)) is used for the active grid motion. Using the quasi-steady transfer function the white noise expected spectrum (red curve) is determined (Fig. 3.13). In contrast to the previously shown broad band excitation (OU) (Fig. 3.12, red curve) the expected energy in the region $0.075 \leq k_{\text{red}} \leq 0.3$ is increased. The measured spectra of the flow generated by this adapted broad band

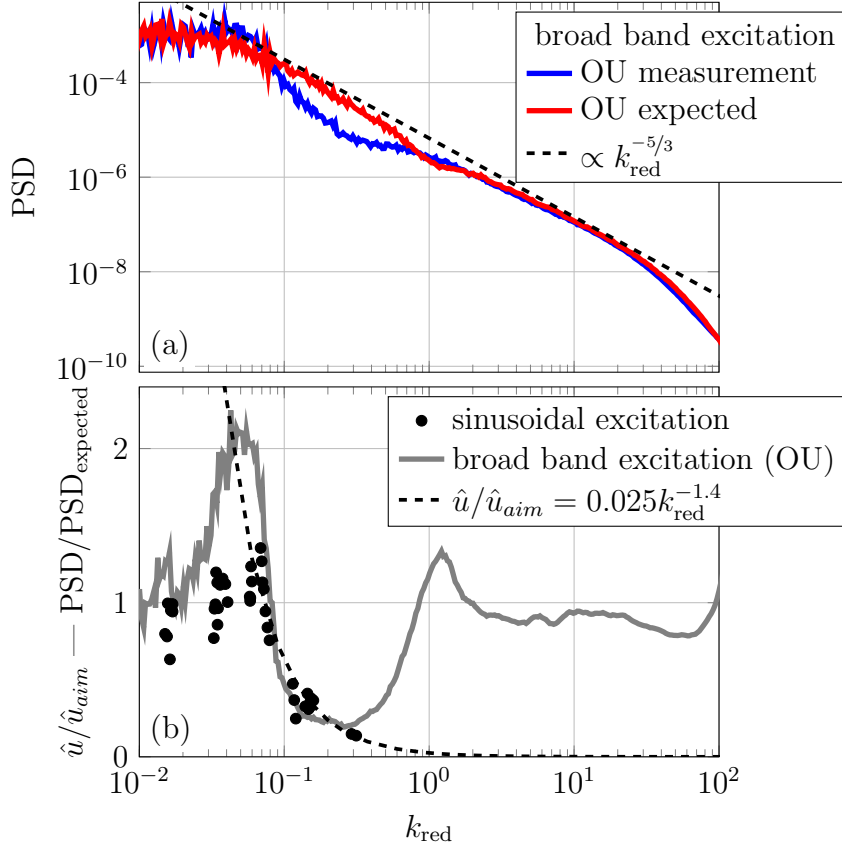


Figure 3.12: Expected and measured power spectral density (PSD) for the broad band excitation (Ornstein-Uhlenbeck (OU)) (a) and normalized PSD and results from sinusoidal inflow (Fig. 3.4 (b)) (b) dependent on the reduced frequency k_{red} .

excitation (WN) contains more energy in the region, where strong damping was observed for the unadapted broad band excitation (OU). In comparison to the unadapted broad band excitation (OU), the WN spectra is closer to the $-5/3$ power law. At the same time, the statistics of the generated velocity time series are hardly affected by this adaption (Tab. 3.2). This is just a first simple improvement, but it shows the capability of this adaption to handle dynamic effects and tailor active grid motion protocols to its applications.

Table 3.2: Statistics of turbulent time series generated with a broadband excitation based on an Ornstein-Uhlenbeck process (OU) and white noise (WN).

Name	$\langle u \rangle$ [m/s]	$\sigma(u)$ [m/s]	skewness	flatness
OU	7.35	0.98	-0.25	3.01
WN	7.29	0.86	-0.23	2.93

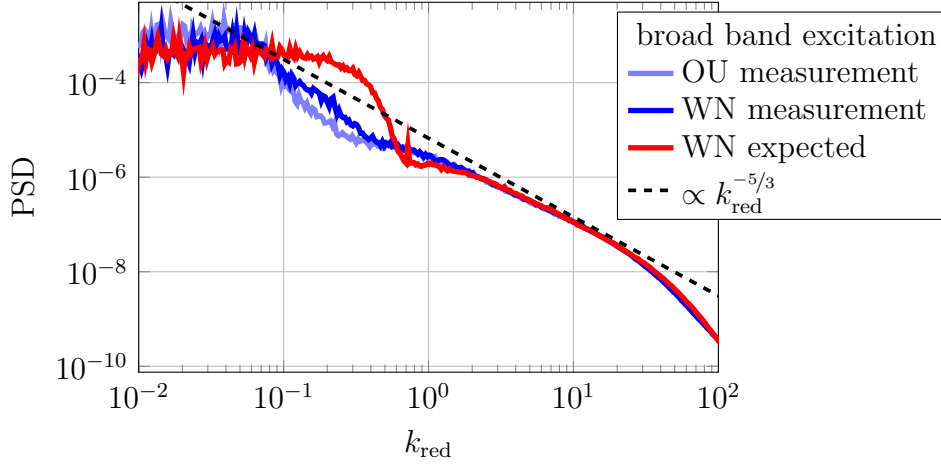


Figure 3.13: Expected and measured power spectral density (PSD) for the adapted broad band excitation (white noise (WN)) dependent on the reduced frequency k_{red} in comparison to the unadapted broad band excitation (Ornstein-Uhlenbeck (OU)).

However, still some lack of energy can be observed. Undergoing some transition further downstream will allow the flow to adapt to a fully developed turbulence as discussed in detail in Ch. 4 (Neuhaus et al., 2020). By this adaptation it may be possible to further control the position of this transition. Also the generation of comparable flow conditions in a larger longitudinal region could be possible by an active variation of the introduced energy on the different scales.

3.4 Conclusion

In this study on the possibilities to generate temporal flow structures with an active grid, a dependence of the excitable frequencies on the reduced frequency was found for the sinusoidal velocity variation. An asymmetric temporal behavior was found for velocity steps and gusts, which in combination with fluctuations after such single events showed the necessity to distinguish between positive and negative velocity increments, as the flow adapts differently to those flow manipulations.

Using a quasi-steady transfer function of the active grid allows to generate flow structures with low reduced frequencies. For reduced frequencies $k_{\text{red}} > 0.075$ a damping of the amplitudes is observed. Additionally, the quality of flow structures decreases, but is found to be good for high amplitudes as long as the reduced frequency k_{red} is below 0.3. However, with increasing reduced frequency the shape deviates further from the expectations.

Furthermore, the same dependence on the reduced frequency is found for turbulence generating protocols. The energy introduced at high reduced frequencies $k_{\text{red}} > 0.075$ by the active grid is below the expectations from the quasi-steady transfer function. Adjusting the active grid motion protocols allows to increase the energy in the damped region and to bring the spectra closer to the desired $-5/3$ power law. Thus, the depen-

dence on the reduced frequency is not limited to specific flow structures, but can be found for a variety of flows with different complexity.

The dimensionless characterisation of the capabilities of the active grid allows to apply these results to other grids. In preliminary investigations comparable behavior was found in three different sized wind tunnels (cross sections: $3 \times 3 \text{ m}^2$, $1 \times 0.8 \text{ m}^2$, and $0.25 \times 0.25 \text{ m}^2$) equipped with active grids (flap diagonals: 0.14 m, 0.106 m, and 0.049 m). Hence, it is propose to use the worked out limitation as design parameter for active grids.

The method presented in this chapter enables to test wind turbines under customized reproducible conditions. Specific flow structures allow for an investigation under isolated extreme events. The turbulent wind fields facilitate to study the turbine dynamics on a broad operational range. Gusts and turbulent flows that are generated by applying the *blockage induced flow design* approach discussed in this chapter were already used by Petrović et al. (2019), Sinner et al. (2021), Pöschke et al. (2022), and Berger et al. (2022). The method therefore enables wind turbine designs and controller designs to be tested under customized, reproducible inflow conditions in the wind tunnel, thus creating optimal conditions for comparison.

Chapter 4

Generation of atmospheric turbulence with unprecedentedly large Reynolds-number in a wind tunnel ¹

In the previous chapter it was shown how specific flow structures can be generated by an active grid and what the limits for this excitation are. The aim of this chapter is to reproduce the statistics of atmospheric turbulence in the wind tunnel. This requires larger integral length scales than are commonly generated in wind tunnels. By this, realistic inflows for wind turbine experiments can be provided.

An experimental approach is presented to generate a turbulent flow with an integral length scale much larger than the tunnel width, using a stochastic process for the active grid motion. First, the downstream development of the active grid generated flow is investigated considering its power spectra and increment statistics. Further, to excite very large scales a dynamic variation of the wind tunnel fan speed is done. The key idea is that whereas the width of the tunnel is usually not larger than several meters, and the maximum transverse turbulent length scale is bounded by a fraction of this, the stream-wise length of the tunnel may exceed this size so that larger correlation lengths can be observed in that direction.

¹The content presented in this chapter is published as Lars Neuhaus, Wouter J. T. Bos, Michael Hölling, and Joachim Peinke: Generation of atmospheric turbulence with unprecedentedly large Reynolds-number in a wind tunnel, *Physical Review Letters*, 2020. L. Neuhaus carried out the measurements as well as the scientific analysis and wrote the manuscript. W.J.T. Bos helped to interpret the results and wrote the section “kinetic energy balance”. Michael Hölling and Joachim Peinke had a supervising function.



Figure 4.1: Active grid installed in the closed test section.

4.1 Experimental setup and turbulence excitation

Measurements are made in the closed test section of the Göttingen type wind tunnel in Oldenburg, having a cross section of $3 \times 3 \text{ m}^2$ and a length of the measurement section of 30 m (Kröger et al., 2018a). Wind velocities up to 42 m/s can be generated by four fans with a power of 110 kW each.

The same active grid as used in Ch. 3 is mounted to the nozzle (Fig. 4.1). In addition to the excitation presented in Ch. 3, the wind tunnel fan speed (and thereby the wind tunnel velocity) is modulate simultaneously to the shaft motion by the motion protocol.

To characterize the flow, an X-type hot-wire 55P61 probe by Dantec Dynamics is placed on the centerline of the closed test section. The hot-wire signals are sampled with a frequency of 20 kHz after being low-pass filtered at 10 kHz. The measurements are repeated for different downstream positions from 1.43 m to 20 m (which correspond to 10M to 140M) using an in-house build 20 m traversing system.

In this chapter a new approach to create atmospheric-like turbulence with large integral length scales is worked out. The idea is to use a stochastic process (e.g., Ornstein-Uhlenbeck process), which exhibits a broadband decaying energy spectra on large scales, for the motion protocol of the active grid, defining the deflection angle of the flaps (see further details in Ch. 3). Half the shafts are moving according to a predefined stochastic process, while the other half is following a motion to compensate the generated global blockage change. In consequence the global blockage is kept constant, whereas the local blockage can vary strongly on short time scales. To ensure an undirected flow, neighboring shafts are pointing in opposite directions.

The groups in this case are defined as an inner group (inner 10 shafts vertical and horizontal) and an outer group (outer 5 shafts per side). Hereby the shafts of the inner

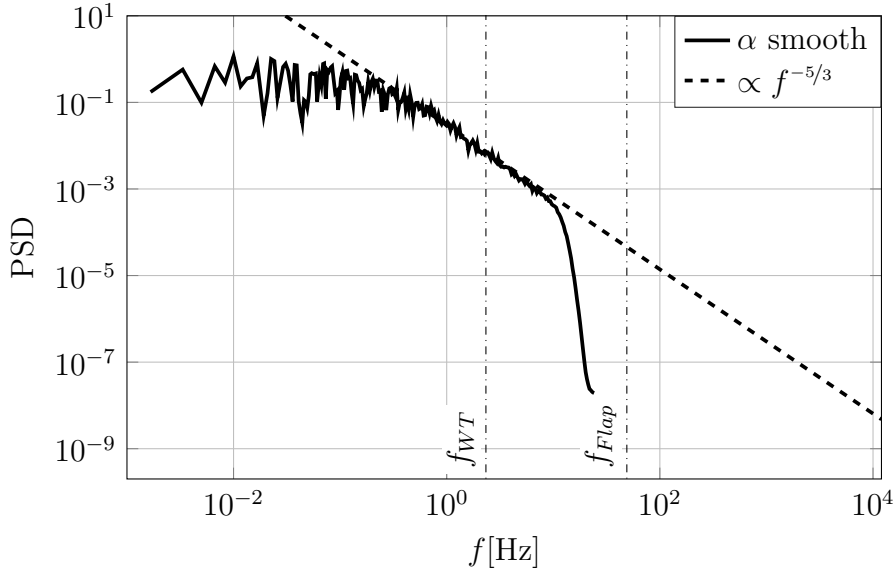


Figure 4.2: Exemplary power spectral density of the excitation protocol of the active grid.

group (roughly 1.5 m x 1.5 m core) are directly correlated, and the same is true for the outer shafts. Furthermore, the shafts of the outer group and inner group are correlated by the definition of β Eq. 3.1. This is leading to a super-position of an excitation by the design of the grid, the separation into different groups, which may be imprinting a grid with a larger spacing, the active grid and the the fan control.

A stochastic time series is used with a scaling based on the Langevin equation

$$\alpha(t + \tau) = \alpha(t) + \tau D_1(\alpha(t)) + \sqrt{\tau D_2(\alpha(t))} \Gamma(t), \quad (4.1)$$

with the drift coefficient $D_1(\alpha) = -4\alpha$, the diffusion coefficient $D_2(\alpha) = 1$ and Gaussian distributed white noise Γ . The time series is scaled to a mean flap angle of $\langle \alpha \rangle = 40^\circ$ and a standard deviation of $\sigma(\alpha) = 10^\circ$. The resulting spectrum of the scaled time series $\alpha(t)$ is given in Fig. 4.2.

Furthermore, the excitation can be expanded to even larger scales by a dynamic variation of the fan speed using the same type of stochastic process. The fan speed is dynamically varied based on a comparable time series, but at a lower frequency. The fluctuations in the low frequency region of the PSD can be found in the stochastic input as well as in the measured spectra, indicating that those fluctuations are directly caused by the stochastic time series of the excitation.

4.2 Analysis of the generated flow

Two experimental approaches are presented. Firstly, only the active grid is used for excitation and the evolution of the turbulence downstream is discussed. Secondly, results of the additional manipulation of the flow by the wind tunnel fans are shown.

In the first approach the fan speed is kept constant, generating a mean wind speed behind the active grid of roughly $\bar{u} = 7 \text{ m/s}$. Measurements are repeated for different downstream positions with the same 10 minute lasting active grid motion protocol.

Energy cascade

The aim is to generate very high Reynolds number turbulence with well developed small and intermediate scales. Therefore, the downstream evolution of the power spectral density (PSD) of the velocity fluctuations is assessed (Fig. 4.3). Two frequencies $f_{Flap} := \bar{u}/L_{Flap}$ and $f_{WT} := \bar{u}/L_{WT}$ are defined, associated with the size of the flaps of the active grid $L_{Flap} = 0.143 \text{ m}$ and with the size of the wind tunnel $L_{WT} = 3 \text{ m}$, respectively.

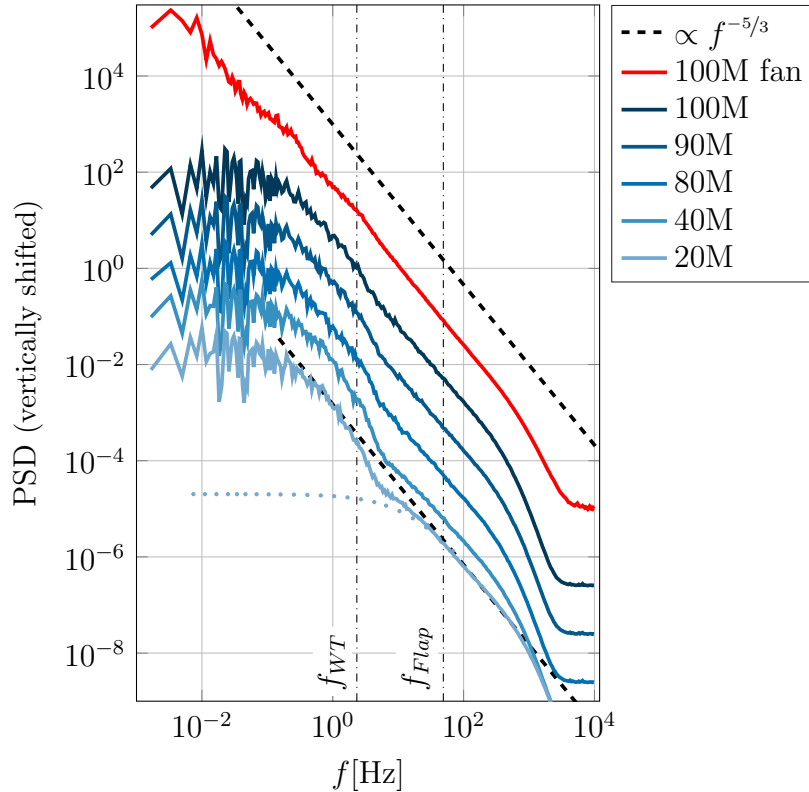


Figure 4.3: Power spectral density (smoothed by exponentially growing bins) of generated turbulence at different downstream positions. For 20M the expected spectrum by the static grid is illustrated by a dotted curve. The statistical fluctuations at small frequencies are an artifact of the random signals that drive the grid (see Sec. 4.1); they are the same for all downstream positions.

Close to the active grid (20M) the spectrum seems to be the superposition of two spectra, one containing energy in the highest frequencies ($f \geq f_{Flap}$), and one containing energy in the lower frequencies ($f \leq f_{WT}$). The high frequency part matches with the expected spectrum of the static grid (indicated by a colored dotted curve).

In between ($f_{WT} \leq f \leq f_{Flap}$) some lack of energy (or gap) is found. A $-5/3$ power law exponent, as expected for fully developed turbulence (Kolmogorov, 1941), is only observed for the low and high frequency parts.

Farther downstream the energy for the highest frequencies (40M) and low frequencies (80M) decreases, whereas the lack of energy in the medium frequencies is filled up by an energy cascade which extends now from the large scales, all the way down to the small scales. Even farther downstream (90M, 100M) the $-5/3$ power law spreads over a wide range of frequencies.

A constant slope from roughly $2 \cdot 10^{-1}$ to $3 \cdot 10^2$ Hz (≈ 3 decades) can be recognized for the far downstream position (100M). The gap between lower and higher frequencies is now closed as its power spectra seem to have merged to form one large cascading process.

To quantify the range over which a constant exponent (close to $-5/3$) is found in the spectrum, a parameter D (in units of decades 10^D) is introduced. To do so, the spectrum is fitted by a polynomial in the frequency range of 10^{-1} to $5 \cdot 10^3$ Hz. Regions in the spectra with almost no curvature are estimated by the second derivative of this fit. The extent D of the power law region is determined by the part of the (smoothed) spectra where the second derivative is below a certain threshold (results do not depend sensitively on the choice of the threshold).

Close to the grid D decreases and stays close to a unity value until, at a downstream position of approximately 86M, D rapidly increases (Fig. 4.4). After this rapid phase-transition-like behavior to a new developed turbulence state, D increases further downstream until a value of 2.4 decades is observed at the farthest downstream positions (125-140M).

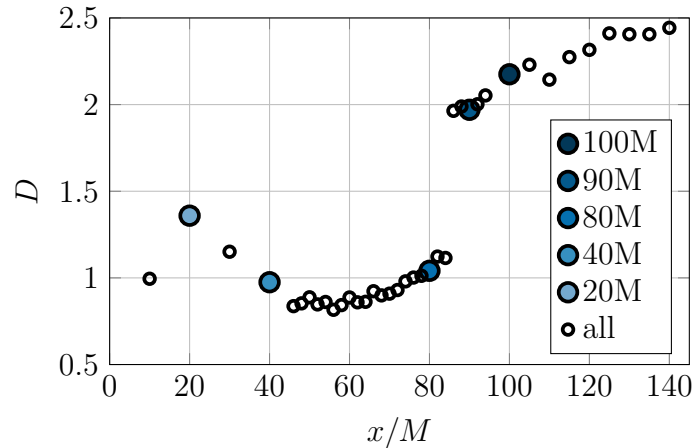


Figure 4.4: Downstream development of the length D of the range of scales over which a constant power law exponent is observed (in decades).

Increment statistics

Besides the power spectra, characterizing the variance of the fluctuations, intermittency is of particular interest. Therefore, the scale, or τ , dependence of the probability density functions (PDF) of velocity increments $u_\tau = u(t) - u(t + \tau)$ is investigated. The widths or the variances, $\langle u_\tau^2 \rangle$, is directly connected to the PSD, as seen by the Wiener-Khinchin theorem (Frisch, 1995). To describe the shape of the PDFs at the time scale τ , a shape factor λ^2 is analyzed (Eq. 2.30), which is shown for different downstream positions in Fig. 4.5 in a semi-log representation.

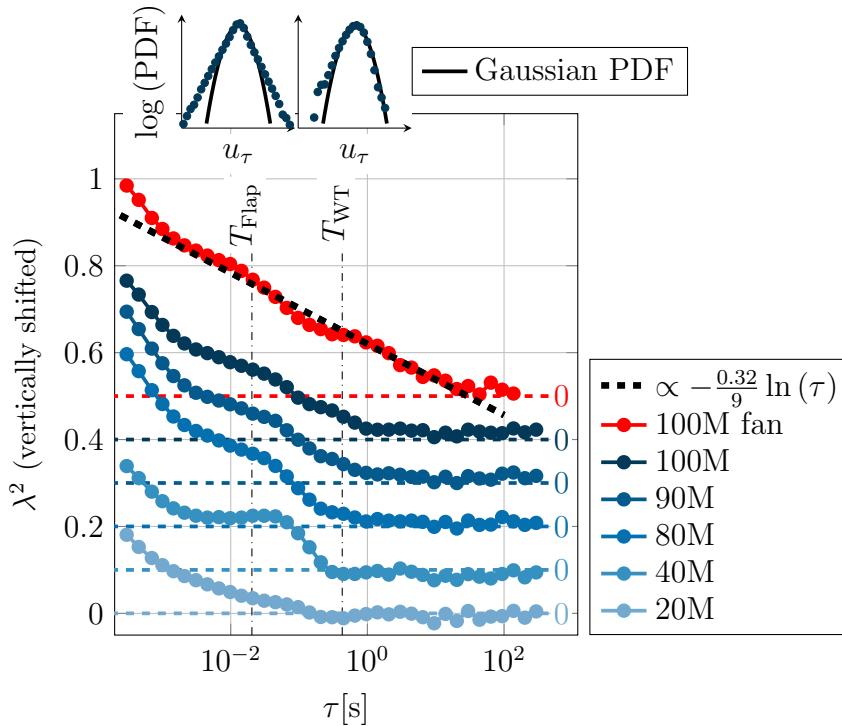


Figure 4.5: Shape factor of generated turbulence at different downstream positions (colored dashed lines correspond to 0, respectively). Increment PDFs are shown exemplarily for the scales of the flaps, T_{Flap} , and the wind tunnel, T_{WT} , for the 100M position.

On large scales the PDFs of the velocity increments, u_τ , are Gaussian and the shape factor is 0. For smaller scales the distributions become more heavy-tailed, a phenomenon known as intermittency. This changing shape of the PDFs can be quantified by the increase of λ^2 , which is connected to the increase of the dissipation rate fluctuations $\langle (\ln \epsilon_r)^2 \rangle \propto \lambda^2(r)$. Following classic phenomenology (Kolmogorov, 1962) the turbulent cascade is characterized by a logarithmic increase of the shape factor

$$\lambda^2(\tau) = (\Lambda_0^2 - \mu \ln(\tau))/9. \quad (4.2)$$

with decreasing scales up to the largest intermittency value on small scales defined via

Λ_0 (Castaing et al., 1990). The so-called intermittency factor μ can be estimated by the slope of $\lambda^2(\tau)$ or by the sixth order structure function (Arneodo et al., 1996, see Eq. 2.32).

The closest upstream position (20M) shows a significant increase of λ^2 only for scales smaller than the flap size $T_{Flap} := L_{Flap}/\bar{u}$ (Fig. 4.5). Distributions close to Gaussian ones are found for $\tau \geq 0.1$ s. The logarithmic increase of the shape factor for smaller τ values shows where typical turbulent behavior is found, consistent with the results of the power spectrum.

Farther downstream (40M) the shape factor increases to small scales in two steps with a plateau close to T_{Flap} . The flow here seems to be dominated by two regions of different scales - one smaller than T_{Flap} and one between T_{Flap} and $T_{WT} := L_{WT}/\bar{u}$. Farther downstream (80M) the two regions begin to merge. At the far downstream position (100M) the logarithmic law is extended over a larger range of scales, consistent with the findings of the extended scaling range in the PSD. Evaluating the slope in the semi-log plot from $2 \cdot 10^{-3}$ s to 1 s after Eq. 4.2, the value $\mu = 0.258$ is obtained. This is in the expected range between 0.2 and 0.3 for ideal turbulence (Davidson, 2004; Arneodo et al., 1996). Consistent results are found by analysis of the sixth order structure function.

Additional fan excitation

In the second experimental approach a low-frequency modulation of the wind tunnel fan speed by a stochastic process is added. The resulting mean wind speed $\bar{u} = 8.4$ m/s is slightly increased. Measurements are done for 100 minutes composed in 10 independent 10 minute intervals. The temperature was measured and found to be stable within 0.2 K.

The PSD and the corresponding behavior of λ^2 for the far downstream (100M) position of this case, where both the fan and the active grid are exciting the flow, are also shown on Fig. 4.3 and Fig. 4.5 as upper red curves. It can be seen that more energy is fed into the system on larger scales and properties of ideal turbulence are extended over a wider range. This corresponds to an even higher Re turbulence state for which a $-5/3$ power law decay in the PSD over ≈ 4.5 decades, and a logarithmic increase of λ^2 over about four decades is found. The intermittency factor of $\mu = 0.318$ is slightly increased.

Length scales

Besides these statistical features of turbulence the length scales are evaluated. The integral length scales are given by

$$L_{ii} = \bar{u} \int_0^{\infty} R_{ii}(\tau) d\tau \quad (4.3)$$

with $R_{ii}(\tau)$ the stream wise auto-correlation function of the i -component of the velocity fluctuations. The isotropic definition of the Taylor-scale λ_T (Eq. 2.21) is calculated

by the velocity fluctuations u' in stream-wise, x , direction. The length scale is numerically estimated for different time lags τ with the assumption of frozen turbulence and $\overline{(\partial u'/\partial x)^2} \approx (\bar{u}\tau)^{-2} \langle u_\tau^2 \rangle$ (Aronson and Löfdahl, 1993). By a linear fit λ_T is extracted closed to $\tau = 0$. These length scales are used to calculate the integral scale Reynolds number $\text{Re}_L = \sqrt{\overline{u'^2}} L/\nu$ and the Taylor Reynolds number $\text{Re}_{\lambda_T} = \sqrt{\overline{u'^2}} \lambda_T/\nu$.

For the case of active grid excitation an integral length scale of $L_{11} = 6$ m (already larger than the diameter of the wind tunnel) and Reynolds numbers of $\text{Re}_L = 4.4 \cdot 10^5$ and $\text{Re}_{\lambda_T} = 3.230$ are achieved. Combined with the additional dynamic fan speed variation, an integral length scale of $L_{11} = 120$ m and Reynolds numbers of $\text{Re}_L = 2.2 \cdot 10^7$ and $\text{Re}_{\lambda_T} = 12.800$ are estimated, comparable to atmospheric flows with values of about 10.000 (Bradley et al., 1981). The integral length scales of the transversal component are found to be $L_{22} = 0.185$ m (active grid) and $L_{22} = 0.505$ m (active grid and fan excitation) due to the geometry of the wind tunnel. Most interestingly, the intermittency of velocity increments measured by the shape factor λ^2 behaves as if L_{22} is of the size of L_{11} as it is shown in Fig. 4.6.

Isotropy

To give further details about the generated flows, the transversal component of the velocity is investigated. Results are shown for the case including the dynamic fan speed variation.

Fig. 4.6 (a) shows the power spectral density of the longitudinal and transversal component of the flow for an excitation by the active grid and the wind tunnel fan. Both spectra show a good agreement for frequencies larger than $f_{WT} := \bar{u}/L_{WT}$, defined with the wind tunnel size $L_{WT} = 3$ m and the mean wind speed \bar{u} . Deviations are found for smaller frequencies. Hence, the wind tunnel size does limit the fluctuations of the transversal component, but not of the longitudinal component.

Fig. 4.6 (b) shows the shape factor λ^2 of the longitudinal and transversal component of the flow for an excitation by the active grid and the wind tunnel fan. Again, on the small scales, a similar behavior of both components can be observed. For scales larger than $T_{WT} := L_{WT}/\bar{u}$, the longitudinal component becomes Gaussian ($\lambda^2 = 0$). For the transversal component, still higher λ^2 values can be found for scales larger than T_{WT} .

Interestingly, at small scales the λ^2 of the transversal component shows about the same intermittency as the one of the longitudinal component, whereas the power spectrum for the transversal component saturates. Taking λ^2 as a parameter, which corresponds to the depth of the cascade, it is conjectured that the transversal cascade starts at a similar depth/intermittency as the longitudinal cascade for this scale - this supports the statement of a slice cut out of much-larger-scale turbulence.

The analysis of the transversal velocity component is showing comparable results for time scales up to 0.5s. This is indicating approximate isotropy in the small scales (Fig. 4.6). The highest isotropy is found at scales of roughly 1 m. The anisotropy for larger scales behaves in a way also observed by Klipp (2014). Hence, the flow exhibits turbulence properties comparable to those found in the atmospheric boundary layer.

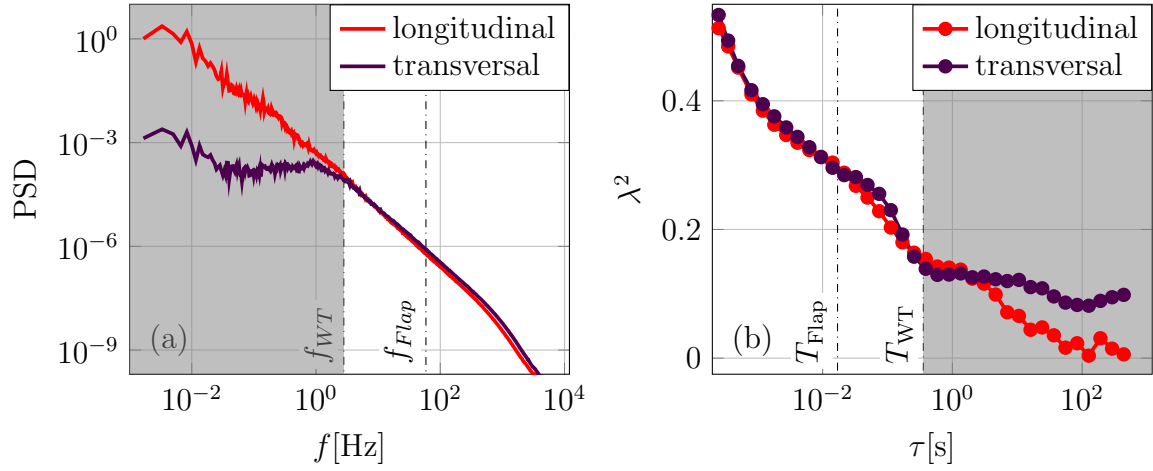


Figure 4.6: Longitudinal and transversal power spectral density (a) and shape factor λ^2 for the longitudinal and transversal component (b) of the excitation by active grid and wind tunnel fans. The gray regions mark scales larger than the wind tunnel width.

Homogeneity

To compare the flow at different positions in a cross sectional region of the wind tunnel the results of two hot-wires are compared (Fig. 4.7). One hot-wire is placed in the centerline and one shifted diagonal by roughly 0.425 m at a downstream position of roughly 126M.

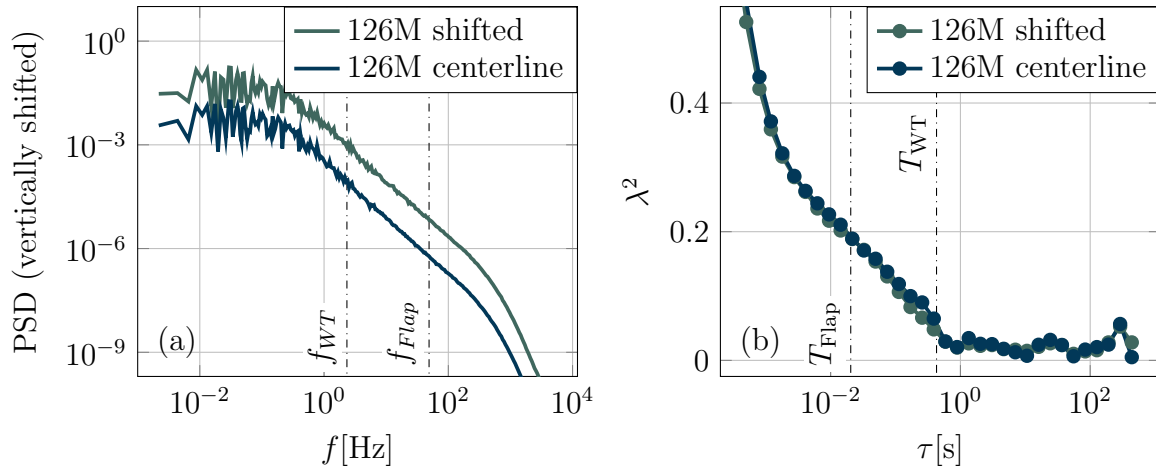


Figure 4.7: Power spectral density (a) and shapefactor λ^2 (b) for measurements by one hot-wire in the centerline and one shifted diagonal in the cross section by 0.425 m for the excitation by the active grid.

The mean wind speed measured in the centerline is 6.91 m/s and the one of the shifted measurement is 6.96 m/s. The turbulence intensities are 15.6% and 15.3%, respectively. Hence, the deviation between both positions is below 2%.

Fig. 4.7 (a) shows the power spectral density for both hot-wires (the PSD of the shifted hot-wire is vertically shifted). Both positions show a comparable spectra. Fig. 4.7 (b) shows the shape factor λ^2 for both hot-wires. Again, both measurements show comparable shape factors. The analysis of the transversal shifted hot-wire is showing comparable results on all scales. In the investigated core region of the wind tunnel a homogeneous flow can be assumed (Fig. 4.7).

4.3 Conclusion

The new approach of excitation of a turbulent flow on scales larger than the experimental set-up itself seems to drastically increase the attainable Reynolds number in wind tunnel turbulence. The investigation of such flows needs long wind tunnels. In the present set-up measurements 80M behind the grid showed the merger of the spectral ranges associated with small and large scale excitation, respectively. At positions $x \geq 100\text{M}$ behind the grid, a continuous scaling range of more than 4 decades, and an integral length scale of more than 100m were measured.

The analysis of the transverse velocity component is showing comparable results like the logarithmic behavior of the shape factors for time scales up to 0.5s, indicating approximate isotropy in the small scales.

It is puzzling that the generated flow, shows, at the small scales, characteristics of turbulence with scales larger than the width of the wind tunnel. A first answer is obtained by realizing that the energy fluctuations are generated differently in the present case. Whereas in classic grids a transverse shear is generated by the grid-bars, in the present case the active grid and wind tunnel fans add a low-frequency longitudinal shear pattern to this. This allows to inject energy into the turbulence at longitudinal scales beyond the tunnel width (for further discussion see Appx. A).

The presence of energy at these low frequencies thereby may act, through nonlocal triadic interaction, as a catalyst for the nonlinear activity at much smaller scales (Domaradzki and Rogallo, 1990; Waleffe, 1992; Alexakis et al., 2005). The rapid filling of the spectral gap, observed in Fig. 4.3 seems to be a direct consequence of this. The low-frequency excitation is therefore not purely decorative but allows to attain turbulence over a wider range of scales than normal, high frequency excitation alone, would allow to attain. It is important that this is confirmed by the shape-factor which shows a large scaling range, reminiscent of very large Reynolds number turbulence.

Thereby, the present work allows to investigate very high Reynolds number turbulence, with small scales which are still relatively large, enabling the experimental study of the interaction of small scale high Reynolds number turbulence in the laboratory. This opens interesting new rescaling applications for experimental investigations of the impact of high Reynolds number turbulence on objects, like the impact of turbulent wind on wind turbines.

Chapter 5

Model wind turbine in turbulent inflow - Application of the Langevin analysis

In this chapter a wind tunnel investigation under reproducible turbulent conditions (generated based on the approaches in the previous chapters) is presented. The main objective here is to provide a method for a systematic analysis of model wind turbines in turbulent inflow. This should further allow for a comparison of different turbine configurations and a precise determination of differences. To do so, a procedure based on the Langevin approach is shown in this chapter. Exemplarily, the analysis is done for a leading edge slat equipped wind turbine in comparison to the baseline turbine.

For full-scale turbines the Langevin approach was introduced to stochastically describe the turbine dynamics (Anahua et al., 2008; Gottschall and Peinke, 2008). This approach allowed to further estimate the so called Langevin power curve (LPC, i.e., the stable operation points of the wind turbine). This LPC in comparison to the common power curve is independent of the turbulence intensity and further sensitive to identify failures and multiple stable operation points (due to failure, but also as consequence of a hysteresis caused by switching between controller regions) (Anahua et al., 2008; Gottschall and Peinke, 2008; Wächter et al., 2011). This approach was till now only applied to full scale turbines. One objective of this work is to determine how it can be transferred to model wind turbines, which have a significantly higher rotational speed and in consequence lower characteristic temporal scales. Further, the Langevin approach will be used to provide a method to systematically compare different turbine configurations.

Another objective is to investigate the effects of slats on a wind turbine. Slats are commonly applied on airplanes. The benefit is a delayed separation, hence higher angles of attack are possible, and at the same time an increased maximum lift at high angles of attack (Smith, 1975). Wind turbines experience high angles of attack in the root region. Due to structural requirements thick profiles are needed here, which exhibit a poor aerodynamic shape. This combination of high angles of attack and

poor aerodynamic shape frequently leads to flow separation in the root region. Hence, stall delaying devices are desirable in the root region. Nowadays, to delay separation, vortex generators are often used on wind turbines which increase the mixing of the flow. But also leading edge slats, influencing the flow on the whole chord of the airfoil, may improve wind turbine performance by delaying stall and increasing the maximum lift.

Investigations on slats for wind turbine application are already made by different research groups. Gaunaa et al. (2012) showed in a numerical study that slats can prevent flow separation in the root region and assumed that an annual energy production (AEP) increase of 1% could be achieved. Wind tunnel investigations on thick airfoil blade segments with a rigid slat showed similar results (Pechlivanoglou et al., 2010). Zahle et al. (2012) combined numerical and experimental investigations and also found the slat concept promising for wind turbines. Their results showed that the angle of attack of maximum lift could be shifted by 16° . Jaume and Wild (2016) optimized the slat design for wind turbine application. Experimental investigations under fluctuating inflow angles, generated by a two-dimensional active grid (Wester et al., 2022), with a rigid slat and an active slat were undertaken based on this optimization (Neuhaus et al., 2018; Singh et al., 2021), showing the benefit of an active slat for load alleviation. Schmidt and Wild (2021) developed a passive adaptive slat, which adapts itself to the current inflow condition based on the pressure distribution on the slat. Steiner et al. (2020) did a parametric numeric investigation of slats on thick wind turbine blades and validated this by wind tunnel experiments (Viré et al., 2021). They found that a slat has the potential of higher aerodynamic efficiency (for high AoA $> 8^\circ$ an increased glide ratio), increased lift, and delayed stall. However, a slat reduces the performance of the airfoil (i.e., the glide ration) for low angles of attack. These studies focused on two-dimensional airfoil investigations and numerical simulations. A detailed experimental investigation on the effects of slats on a rotating system was not done and will be treated in this chapter.

Hence, the objective of this chapter is manifold. A new conceptual wind turbine with slats will be investigated in a wind tunnel equipped with an active grid, which is generating atmospheric-like inflow, and its power characteristics (dynamics) will be analyzed by the Langevin analysis. The applicability of the active grid generated flows (Ch. 3, 4) to the model wind turbine needs to be investigated. A procedure for comparing the different turbine configurations based on the Langevin approach is worked out and exemplarily shown for the slat equipped turbine in comparison to the baseline turbine. Therefore, a focus is put on the deterministic behavior of the power output of the turbine.

5.1 Experimental setup and methods

Experiments are conducted in the large $3 \times 3 \text{ m}^2$ wind tunnel in Oldenburg (Kröger et al., 2018a) (Fig. 5.1). The wind tunnel is operated without (laminar inflow) and

with the active grid (Ch. 3, 4). The model wind turbine Oldenburg with a diameter of 1.8 m (MoWiTO 1.8) is mounted 4.75 m downstream of the wind tunnel nozzle (Berger et al., 2018). Two rotor configurations are investigated, one without slats (baseline) and one with leading edge slats installed in the root region (Fig. 5.1 (b)) The inflow is characterized by hot-wire anemometry 2.2 m downstream of the wind tunnel nozzle (2.55 m upstream of the MoWiTO 1.8).

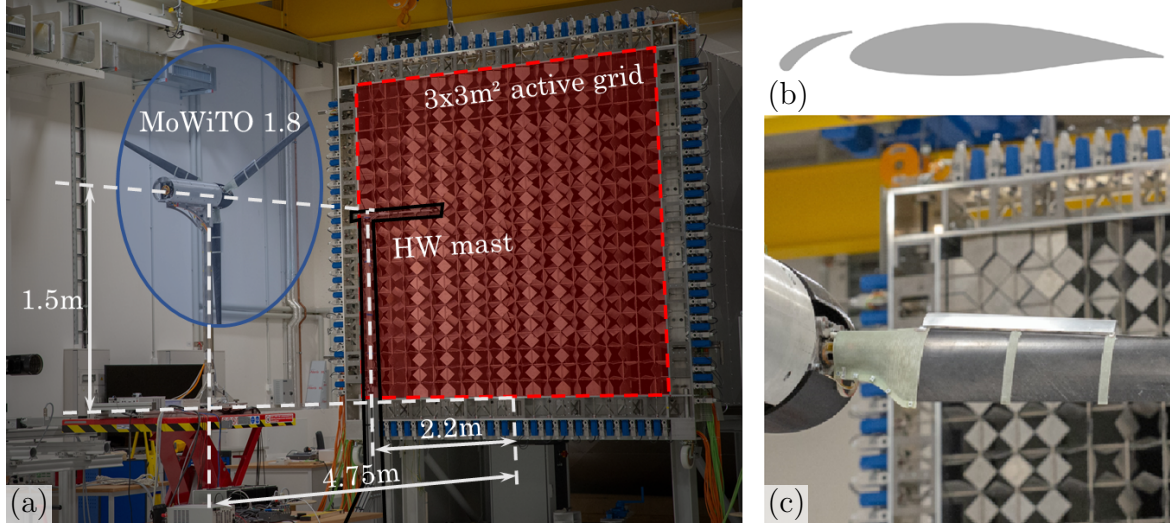


Figure 5.1: Setup in the wind tunnel, with hot-wire (HW) mast and MoWiTO 1.8 downstream of the nozzle equipped with the active grid (a). Schematic of the airfoil with superimposed slat (b). Slat installed in the root region of the MoWiTO 1.8 (c).

Active grid - generated flow

The active grid is used as described in Ch. 3, 4 (Neuhaus et al., 2020, 2021). Flow is generated using the active grid and the wind tunnel fans comparable to the approach presented in Ch. 4.

The flow is measured by three hot-wires on a mast (horizontally shifted from the centerline by -0.225 m, 0.07 m, and 0.45 m, respectively), 2.2 m downstream of the active grid. The location is sufficient to estimate the current mean inflow velocity experienced by the model wind turbine, even though the turbulence continues to develop downstream as shown in Ch. 4.

A 30 min time series is generated with a medium TI level (Fig. 5.2). Here, the mean wind speed and TI are determined for 12 s sections. These sections correspond to the commonly 10 min sections used for characterizing atmospheric wind and full scale wind turbines, considering the temporal scaling factor of roughly 50. Fig. 5.2 shows the probability density function of these 12 s mean wind speeds and the 12 s TI as well as the mean TI dependent on the mean wind speed. The overall TI of the generated flow field is in the order of 13%, which is by the turbulence classes definition of the IEC-standard 61400-1 (IEC, 2019) a low to medium turbulence intensity.

This active grid generated flow is mimicking the statistics found in the atmosphere and reproducible. By this it is perfectly suited for experiments, as it allows to vary, e.g., turbine parameters and investigate its behavior under the exact same inflow conditions. In this chapter, the focus is set on an investigation of the power output of a turbine with and without slats. However, the approach also enables to test new control methods and to investigate and compare loads on turbines.

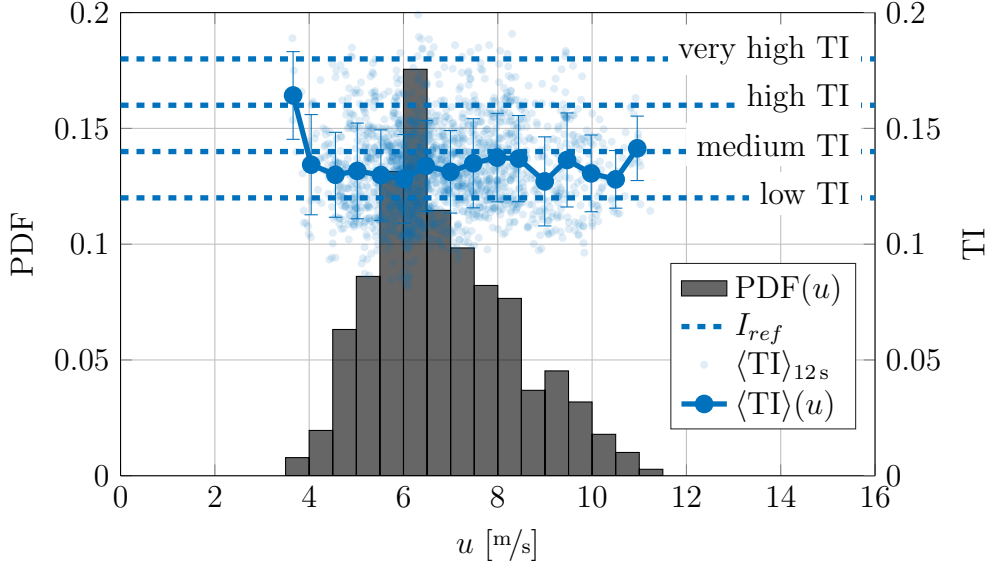


Figure 5.2: Probability density function (PDF) of the wind speed and corresponding mean turbulence intensity in comparison to the reference turbulence intensity I_{ref} by the IEC standard.

MoWiTO 1.8

The model wind turbine Oldenburg with a rotor diameter of 1.8 m is used (Berger et al., 2018, 2021). The turbine is controlled and data recorded by a CompactRIO PAC system. Measures as torque, rotational speed, and wind speed (beyond other, which are not used in here) are recorded with a sampling frequency of 5 kHz simultaneously on one machine. Torque control is used in the partial load and pitch control (constant rotational speed) in the full load region. The transition between both regions is made by keeping the rotational speed constant and increasing the torque up to rated torque. In contrast to the design rotational speed of $600 \text{ }^1/\text{min}$ the turbine is down rated here to $550 \text{ }^1/\text{min}$ for safety reasons.

For the measurements the MoWiTO 1.8 was equipped with leading edge slats in the root region. The slat design follows the approach by Jaume and Wild (2016) for a DU91-250 profile. In a numerical study it was then further optimized for the thinner blades and lower Reynolds numbers of the MoWiTO 1.8 blades with SG6040 profiles (Teßmer et al., 2021). The maximum lift coefficient is shifted from an angle of

attack of 12° to 16° and increased from roughly 1.3 to roughly 1.8. The slats are not permanently fixed, hence a quite bulky support on the blades is needed for a secure operation consisting out of a shoe at the root, ensuring no radial motion, and belts, keeping the slat in position (Fig. 5.1 (c)). It is positioned in the root region, covering a radial range from $0.2R$ (position of first aerodynamic shaped cross section of the blade) to $0.42R$. By this the blade inertia increased by 19% (14% inertia increase including hub and drive train).

Analysis

The characterization of the overall dynamic behavior of the wind turbine is done by applying the Langevin approach (Sec. 2.3) (Anahua et al., 2008; Gottschall and Peinke, 2008). Here the system is described by the Langevin equation

$$P(t + \tau) = P(t) + D_1(u(t), P(t))\tau + \sqrt{D_2(P(t), (u(t)))\tau}\Gamma_t \quad (5.1)$$

consisting out of the drift term, which is describing the deterministic behavior by the drift coefficient D_1 , and diffusive term, which is describing the stochastic behavior by the diffusion coefficient D_2 and δ -correlated Gaussian white noise Γ_t with the time lag τ . These coefficients, the Kramers-Moyal coefficients

$$D_n(u, P) = \frac{1}{n!} \lim_{\tau \rightarrow 0} \frac{1}{\tau} M_n(u, P) \approx \frac{1}{n!} \frac{dM_n(u, P)}{d\tau}, \quad (5.2)$$

can be extracted from a time series based on the slope of the conditional moments

$$M_n(u, P, \tau) = \langle (P(t + \tau) - P(t))^n \rangle_{|P(t)=P, u(t)=u}. \quad (5.3)$$

The coefficients are determined for bins of the corresponding parameters u and P (here wind speed and power but can also be applied to, e.g., wind speed and rotational speed or rotational speed and torque).

The wind speed is measured upstream of the wind turbine, hence there is a certain delay between measured wind speed and power. This delay

$$\Delta T(t) = x_{\text{HWtoMoWiTO}}/u_{\text{movavg}}(t) \quad (5.4)$$

is estimated by the moving averaged wind speed

$$u_{\text{movavg}}(t) = \frac{1}{Tf} \sum_{\Delta t=-T/2}^{T/2} u(t + \Delta t) \quad (5.5)$$

with $T = 1$ s (corresponding to 9.167 rotor revolutions at rated rotational speed) and the distance between hot-wire and wind turbine $x_{\text{HWtoMoWiTO}}$. The delay is then applied to the wind speed to get the rotor-plane corresponding wind speed

$$u_{\text{corr}}(t) = u(t + \Delta T(t)). \quad (5.6)$$

This corrected wind speed gives a better estimate of the wind velocity experienced by the turbine and is used for the estimation of the conditional moments.

5.2 Results

The different turbine configurations are investigated based on their performance, considering power production and the dynamic response of the system. Initially, a laminar characterization is done Sec. 5.2.1. In the following, the power output and the dynamic behavior of the turbine in turbulent inflow are investigated Sec. 5.2.2.

5.2.1 Laminar characterization of MoWiTO with slats

A first investigation of the slat influence on the turbine behavior is done by operating the turbine at a fixed rotational speed of 480 1/min for different fixed pitch angles of the blades (contrary to the torque controller mentioned in the experimental setup (Sec. 5.1)). The pitch is defined here as positive when pitched towards the feather position, and negative when pitched towards the stall position. Hence, with decreasing pitch angle a higher local angle of attack on the blade can be expected. To characterize the behavior for different tip speed ratios (TSR), the wind speed is varied step wise by the wind tunnel fans while the rotational speed is kept constant. Per step the corresponding rotational speed n and torque T of the model wind turbine are measured and used to calculate the power $P = 2\pi nT$ (Fig. 5.3).

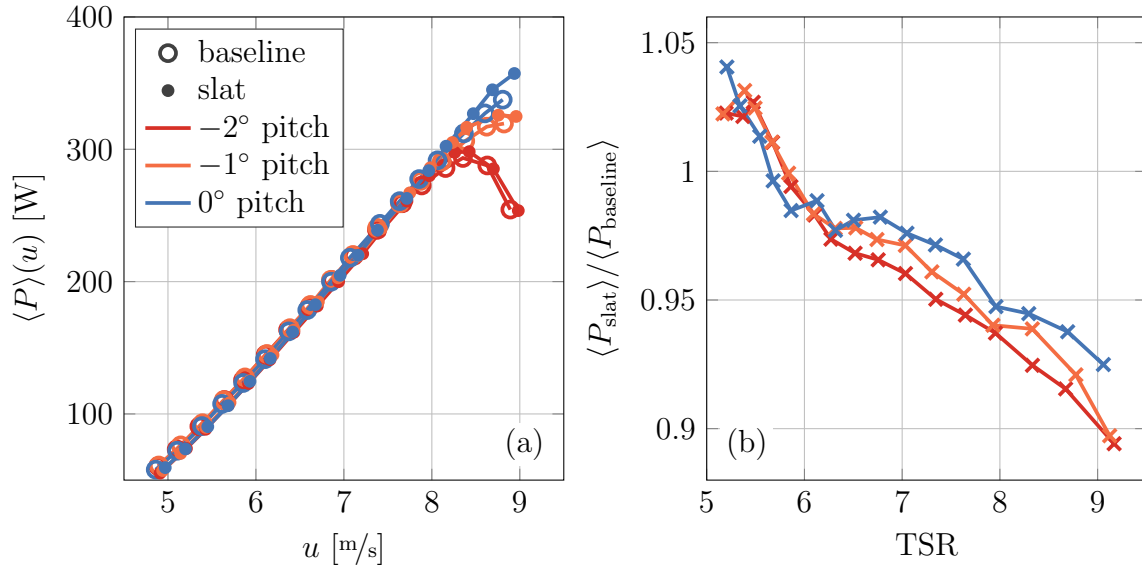


Figure 5.3: Power P dependent on the wind speed u for fixed rotational speed (a) and ratio of power of the slat configuration to the baseline configuration dependent on the TSR (b).

Measurements are performed with and without slats (baseline configuration) for three different pitch angle settings (-2° , -1° , and 0°). The difference between both configurations are comparatively small (Fig. 5.3 (a)). Fig. 5.3 (b) shows the ratio of slat to baseline configuration for power dependent on the TSR. A lower TSR corresponds

to a higher angle of attack. For the slat a beneficial effect is expected for larger angle of attack (more negative pitch angle or lower TSR). This effect can be recognized for $\text{TSR} < 6$. For $\text{TSR} > 6$ the power output of the wind turbine with slats is reduced compared to the baseline configuration. This reduction becomes significant for $\text{TSR} > 8$, for which the power of the slat configuration is decreased to values below 95%.

The installation of slats in the root region of the turbine blades, allows for a more sufficient operation of the turbine at low TSR. This might be caused by the beneficial effect of slats for high angles of attack, e.g., increased maximum lift and stall delay. Compared to the baseline configuration, this positive effect at the root might compensate the negative effect of high angles of attack at the blade tip (e.g. increased drag and stall) and might shift the blade load closer to the turbine hub.

5.2.2 Dynamic characterization - in turbulent inflow

The wind turbine is now exposed to turbulent inflow generated by the active grid and the dynamic behavior of the wind turbine is investigated for different configurations (Tab. 5.1). In the following measurements, the commonly used baseline controller with a TSR of 7.5 is applied (partial load: variable rotational speed control by torque; full load: fixed rotational speed control by blade pitch). For the slat configuration two different controller settings are picked — one which will operate the turbine at a comparable TSR of 7.5 and blade pitch angle of 0° as the baseline turbine and one setting which forces the blades to experience higher angles of attack by pitching the blades to -2° and run the turbine at a TSR of 7.

Basic analysis

In a first step a basic analysis is done. Therefore the power curve is determined (Fig. 5.4 (a, c)) and the dynamic behavior analyzed by the power spectral density (PSD) (Fig. 5.4 (b, d)).

The turbine performance is described by the power curve using 12 s (corresponding to 10 min full-scale) mean values. The active grid generated flow allowed to cover the whole power curve by a 30 min turbulent velocity field (from cut-in (here the limit is the minimum $n = 400 \text{ 1/min}$) to the full-load region (however not up to the cut-out wind speed)). The ratio of the power curve to the Baseline TSR 7.5 configuration is shown in Figure 5.4 (c). The differences between the configurations are below 5% and

Table 5.1: Different turbine configurations investigated in turbulent inflow.

Configuration	TSR	pitch angle
Baseline TSR 7.5	7.5	0°
Slat TSR 7.5	7.5	0°
Slat TSR 7	7	-2°

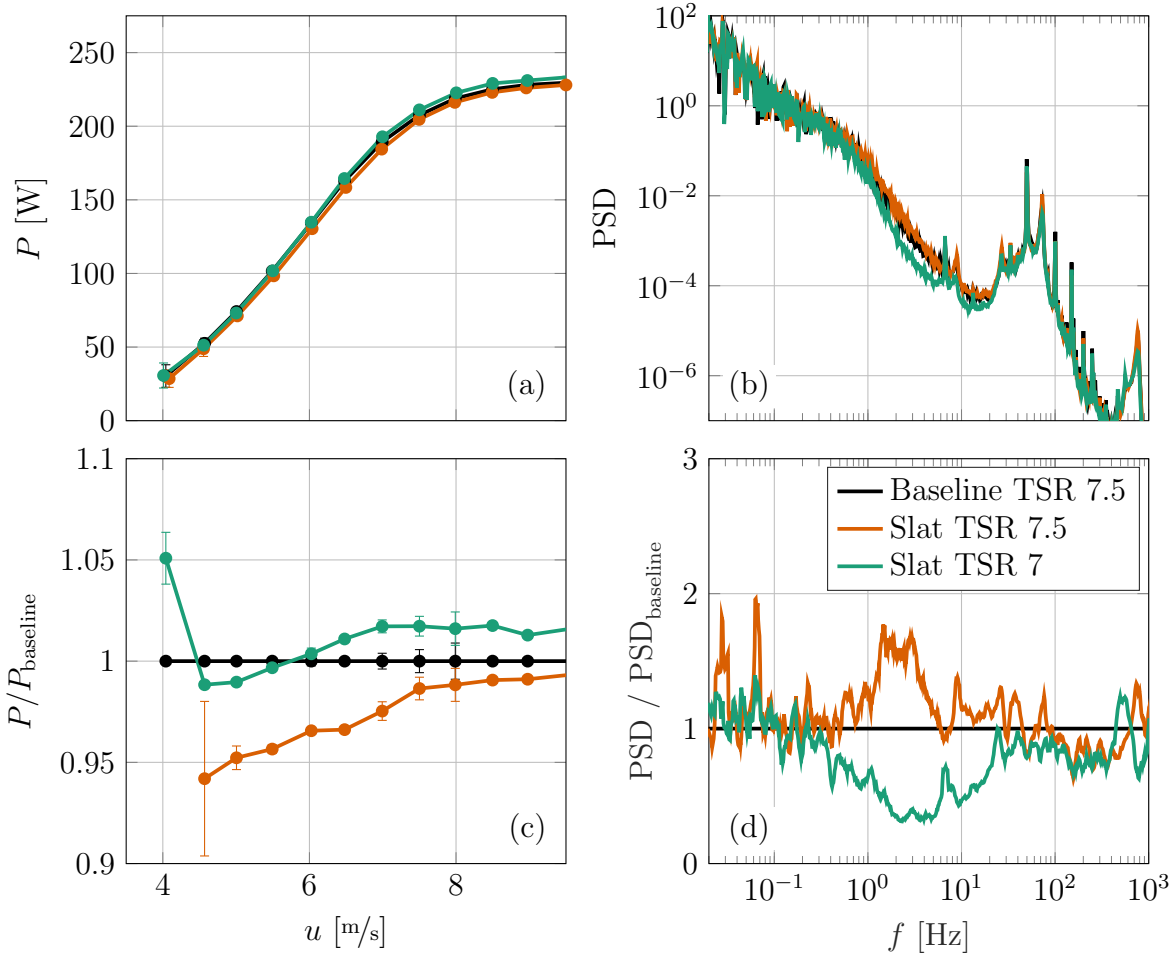


Figure 5.4: Power curve (a) and power spectral density (PSD) of the power fluctuations (b) for the different wind turbine configurations, and the ratio to the Baseline TSR 7.5 configuration of the power curve (c) and PSD (d).

mostly even below 2.5%. However, the slat configuration operated at a lower TSR shows the better performance. This might be caused by an operation closer to the favorable TSR, identified by the laminar characterization.

The power spectral density is shown in Figure 5.4 (b). Turbine eigenfrequencies can be recognized from 20 to 100 Hz. Further two peaks, caused by the rotational speed at $400 \text{ }^1/\text{min}$ (6.7 Hz, minimal rotational speed) and at $550 \text{ }^1/\text{min}$ (9.2 Hz, maximal rotational speed), can be found. For frequencies below the eigenfrequencies, the spectra of the configurations deviate. The Slat TSR 7 configuration shows a significant reduction of the energy in the frequency range from 0.3 to 20 Hz (Fig. 5.4 (d)). In contrast stronger fluctuations in this region can be found for the Slat TSR 7.5 configuration. Hence, the slat configuration with a lower TSR seems to be beneficial here.

The Langevin approach

Both – power curve (averaged information) and power spectral density (frequency response of a single signal) – only revealed small differences between the configurations. To gain further information, the Langevin approach is applied (Anahua et al., 2008). The Langevin approach allows to reveal the dynamic response of the turbine with respect to the incoming wind field.

Estimation of the drift coefficient First, the Langevin analysis will be exemplary shown for the Baseline TSR 7.5 configuration. The analysis is done on a two-dimensional plane, spanned by the wind velocity u and the power output P . This plane is divided into equally sized bins with a width of 0.2 m/s and 5 W .

The conditional moments $M_1(\tau)$ (Eq. 5.3) are determined per bin and time increment τ (Fig. 5.5 (a-c)). Periodic fluctuations of M_1 can be recognized for all chosen examples. However, clear trends can be identified for the individual examples. These trends, can be estimated by fitting the conditional moments over several of these fluctuations. In this setup a time increment range from $\tau = 12$ to 77.4 ms is found to be sufficient (but also other ranges may be feasible). The drift coefficients D_1 are estimated by the slope of the conditional moments in this range (Fig. 5.5 (d, f)). So, for every operational point (defined by velocity and power bin) an individual trend can be observed, which is describing the deterministic dynamic behavior of the turbine at this operational point. A positive drift results in a dynamics with an increasing power, while a negative drift corresponds to a decrease of the power.

For low power outputs, the drift is positive, and for high power outputs it is negative (Fig. 5.5 (d)). On a wide range the drift shows a linear trend from which it deviates at high powers (different turbine behavior). Integrating the drift coefficient gives the potential $\Psi = -\int_{\min(P)}^P D_1(P)dP$, which illustrates the stability of the individual states (Fig. 5.5 (e)).

The determination of the drift coefficient for all velocity and power bins gives the drift field shown in Fig. 5.5 (f). The zero-crossings of the drift coefficient (the local minima of the potential) are defining the stable fixed points. The stable fixed points describe the Langevin power curve (LPC) to which the turbine tends for a laminar flow. Per wind speed bin, only one zero crossing is observed. Hence, no multiple stable points are found which may indicate a hysteresis.

Meaning of the drift coefficient To understand the meaning of the drift coefficient its effect is further analysed based on the drift field extracted for the Baseline TSR 7.5 configuration. A benefit of the Langevin analysis is, that the extracted drift coefficient allows to model the turbines deterministic behavior for synthetic inflows. Here synthetic wind time series u_{syn} are used to calculate the deterministic power output of the turbine

$$P_{D_1}(t + \tau) = P_{D_1}(t) + \tau D_1(u_{syn}(t), P_{D_1}(t)) \quad (5.7)$$

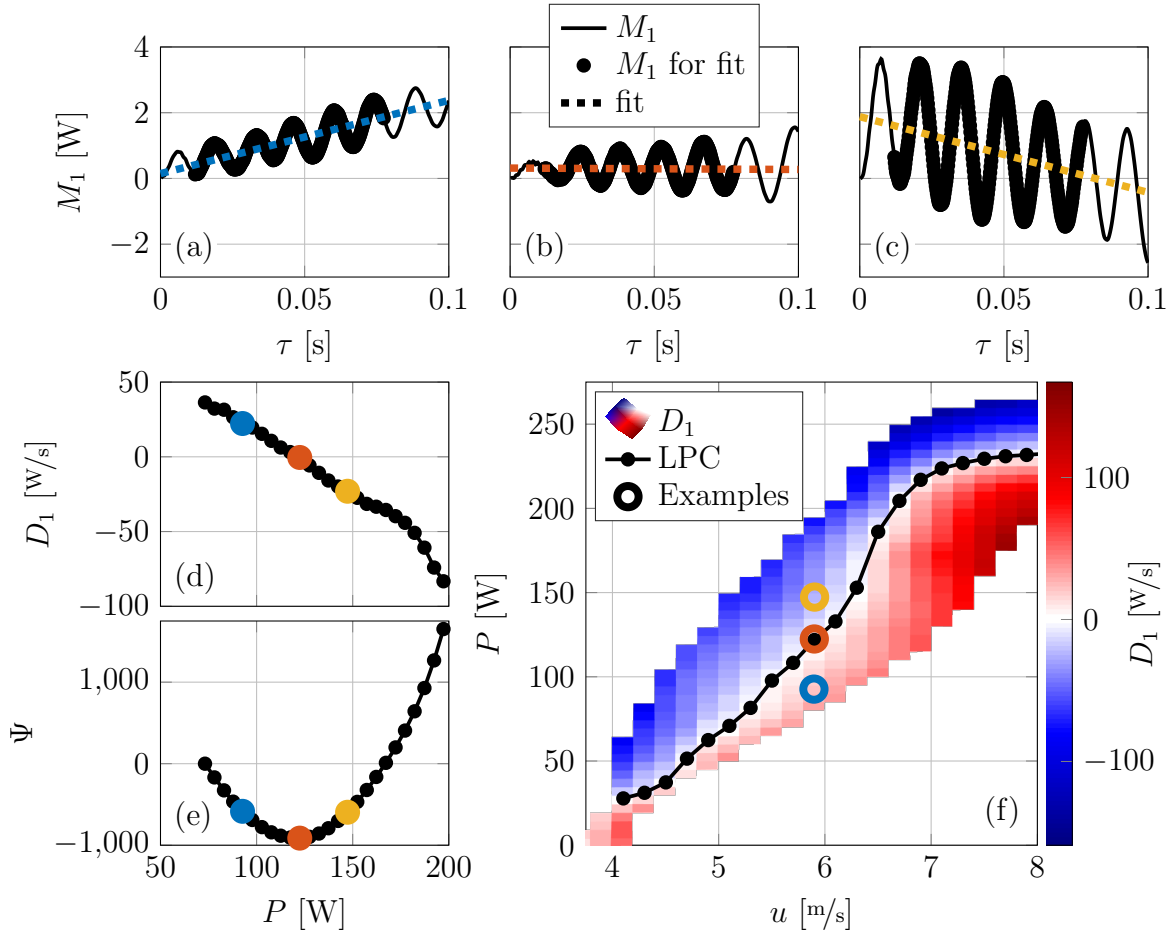


Figure 5.5: Example of extracting the drift field D_1 (f) out of the conditional moments M_1 (a, b, c). Conditional moments are exemplarily shown for the velocity bin at 5.9 m/s and the power bins 92.5 W (a), 122.5 W (b), and 147.5 W (c). The resulting drift for this velocity bin is shown in (d) and the potential Ψ in (e).

by the stochastic model of the turbine neglecting the diffusive term. For the calculation the drift field $D_1(u, P)$ is linearly interpolated and extrapolated, providing a high resolved look up table.

As the drift coefficient D_1 defines the turbine reaction, the resulting power time series of a velocity step is investigated (Fig. 5.6). A step size of 0.6 m/s up and down around a mean velocity of 6 m/s is chosen. The steps response of the turbine can be described by the function $P_{\text{fit}} = \Delta P(1 - e^{-t/T_{\text{react}}}) + P_0$ with the reaction time T_{react} , the power output before the velocity step P_0 , and the difference between the power before and after the step ΔP . The reaction time is determined here exemplarily in two different ways (Tab. 5.2). It can be estimated by the intersection of the tangential of the power time series at the moment of the velocity step with the upper respectively lower power level (T_{tan}). The slope of the tangential at the moment of the velocity step corresponds to $D_1(t_0)$ at the time of the velocity step t_0 . Hence, the reaction time

based on the tangential $T_{\text{tan}} = \Delta P/D_1(t_0)$ is given by the drift $D_1(t_0)$. The reaction time can also be estimated by the area between P_{D_1} and the upper respectively lower power level divided by ΔP (reaction time based on the integral T_{int}).

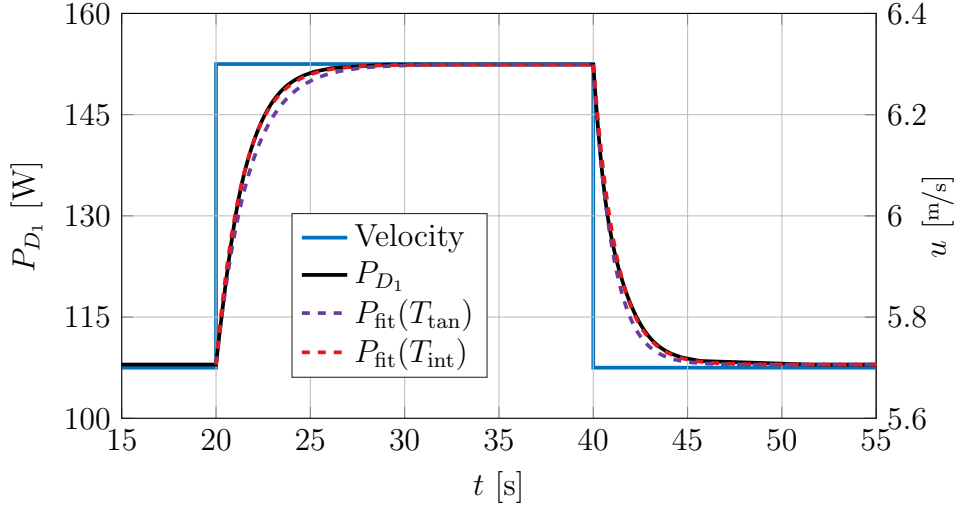


Figure 5.6: Synthetic deterministic power time series P_{D_1} calculated based on D_1 for a velocity step.

Table 5.2: Extracted reaction time for velocity steps.

velocity step	T_{tan} [s]	T_{int} [s]
upwards	1.72	1.46
downwards	1.06	1.21

The deterministic behavior of the turbine for a velocity step can be well described by the exponential function P_{fit} . Applying T_{int} gives the better results here, as D_1 shows no strictly linear dependence on power output, as assumed by the T_{tan} -approach. Hence, to correctly describe the turbine behavior the individual D_1 need to be considered.

Effect of the drift coefficient A higher D_1 corresponds to a faster reaction time. In a next step the consequences of different drift magnitudes (reaction times) for the turbine operation are investigated. Therefore, the drift look up table is multiplied by factors ranging from 0.1 to 10 giving 21 manipulated stochastic models. Simple gusts (negative cosine shifted up by the amplitude) are given to these manipulated stochastic models to determine the corresponding deterministic power outputs P_{D_1} . The duration is 1s and the gust magnitude (twice the amplitude of the cosine) is varied from -1 to 1 m/s.

Exemplarily, P_{D_1} time series for a -1 m/s (Fig. 5.7 (a)) and 1 m/s (Fig. 5.7 (c)) gust are shown for multiplication factors of 0.1, 0.32, 1, 3.16, and 10. A higher drift

leads to a faster reaction. Lower drifts lead to a delayed and damped reaction. The consequence for the energy production is shown in Fig. 5.7 (b, d). The generated energy is calculated by the integral of the power in the observed time range. The difference of the generated energy ΔE is calculated by the difference towards the not manipulated case ($1D_1$). Lower D_1 are beneficial for negative gusts, as the produced energy is increased compared to the not manipulated case (Fig. 5.7 (b)). Higher D_1 are beneficial for positive gusts. Fig. 5.7 (d) shows the sum of the difference of the generated energy ΔE for the different multiplication factors. Due to the cubic dependence of the power on the wind speed, lower D_1 are unfavorable (considering energy production) (Fig. 5.7 (d)). Higher D_1 lead to higher energy production in gusty (turbulent) conditions, however will also cause higher fluctuations.

This is only a theoretical consideration. The drift coefficient D_1 cannot be set directly, but is a consequence of a large number of system parameters that contribute to the deterministic dynamic behavior of the wind turbine. However, with this knowledge concepts can be systematically evaluated.

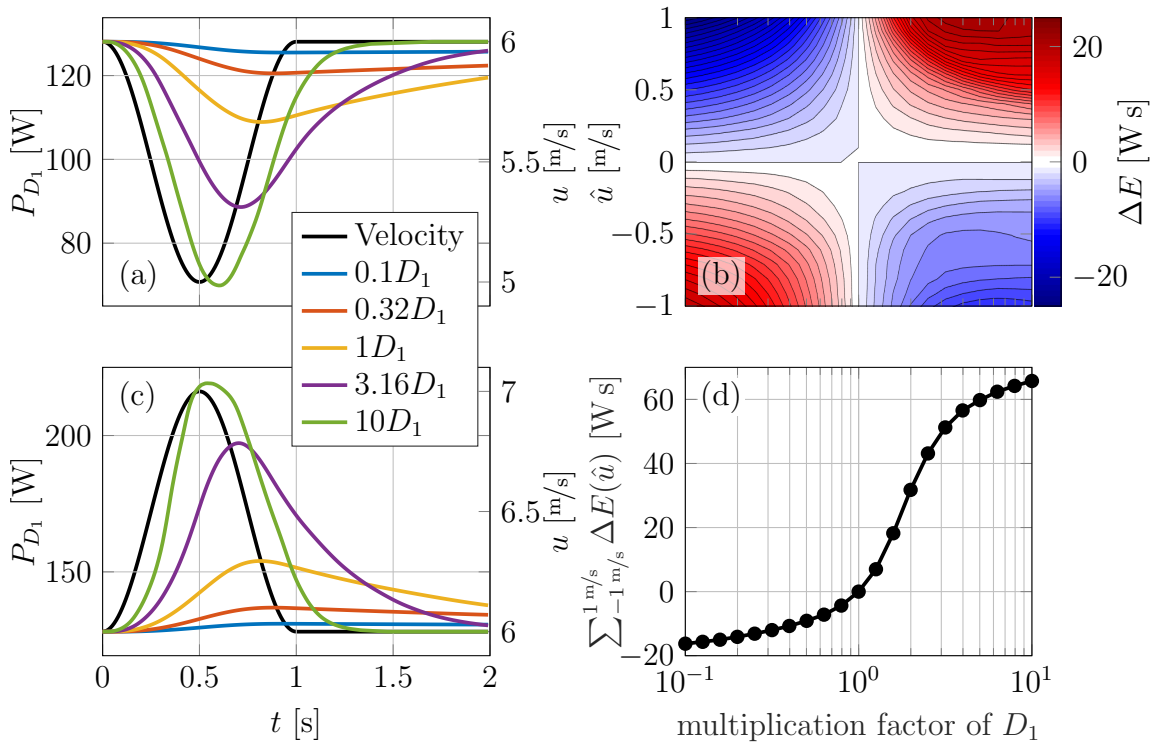


Figure 5.7: Effect of D_1 on the energy production. Deterministic power output for different multiplication factors of D_1 for a negative (a) and a positive gust (c), the resulting difference of the generated energy ΔE dependent on the multiplication factor of D_1 and the gust amplitude (b), and the mean of this difference dependent on the multiplication factor (d).

Application of the Langevin approach

Based on this analysis method the different turbine configurations are compared. Fig. 5.8 shows the ratio of the drift D_1 of the slat configurations towards the drift of Baseline TSR 7.5 configuration $D_{1,\text{Baseline}}$ (see Appx. B for individual drift values and Appx. B for details on the drift slopes).

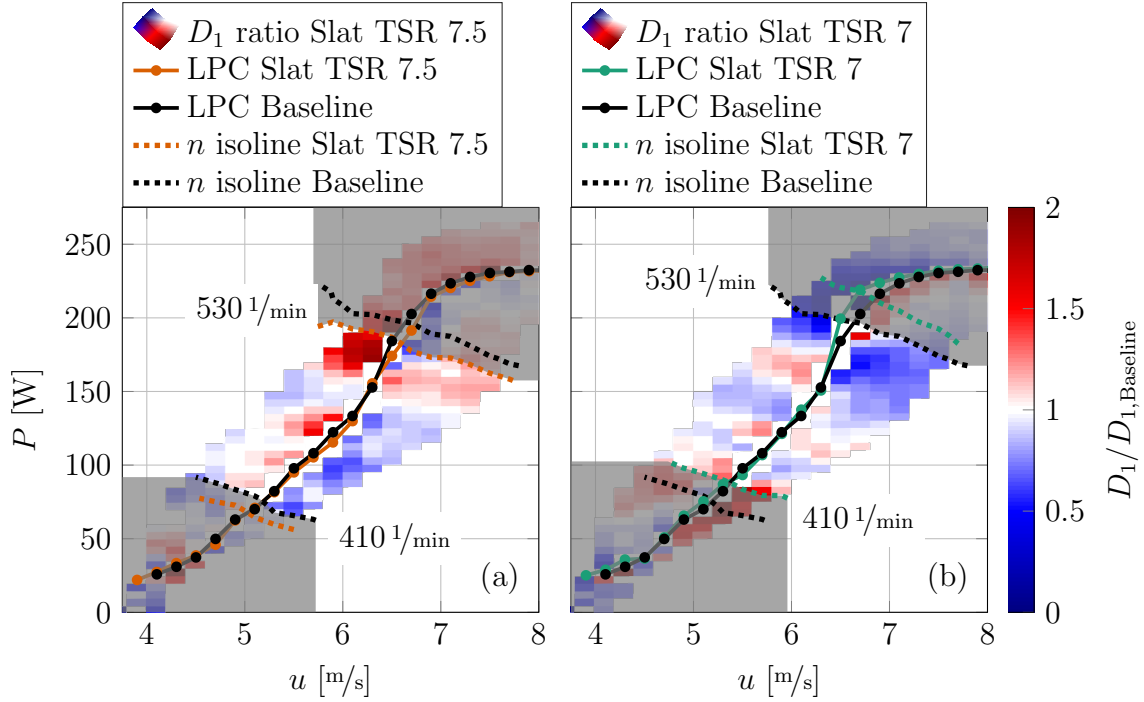


Figure 5.8: Ratio of the drift D_1 of the Slat TSR 7.5 (a) and Slat TSR 7 (b) configuration to the drift of the Baseline TSR 7.5 configuration $D_{1,\text{Baseline}}$. Shaded areas mark regions outside the considered partial load region (between the rotational speed isolines).

High deviations are found for large wind speeds and power outputs. For high power outputs in the region of $n = 530$ 1/min, the Slat TSR 7.5 configuration exhibits a drift which is up to twice the one of the Baseline TSR 7.5 configuration (Fig. 5.8 (a)). Interestingly, in the same region the drift for the Slat TSR 7 configuration is half the drift of the Baseline TSR 7.5 configuration or even less (Fig. 5.8 (b)). This is in good agreement with the higher fluctuations found in the PSD (Fig. 5.4 (b, d)) for the Slat TSR 7.5 configuration and the lower fluctuations for the Slat TSR 7 configuration, as power output fluctuations are assumed to be caused by the drift. For a small region around $n = 410$ 1/min, the opposite behavior can be found, where the drift of the Slat TSR 7 configuration is the highest.

However, the controller needed to be adapted for the different configurations, causing strong deviations in its behavior outside the partial load and especially at the switching region between partial and full load region (Fig. 5.9, see Appx. B for a de-

tailed discussion). In the partial load region ($410 \text{ 1/min} < n < 530 \text{ 1/min}$) the turbine configurations exhibit different dependencies of the torque on the rotational speed, but overall show a comparable behavior. Hence, differences in D_1 outside the partial load region might be significantly affected by these different controller settings and the different controller settings are assumed to have a minor effect on the dynamic response in the considered partial load region.

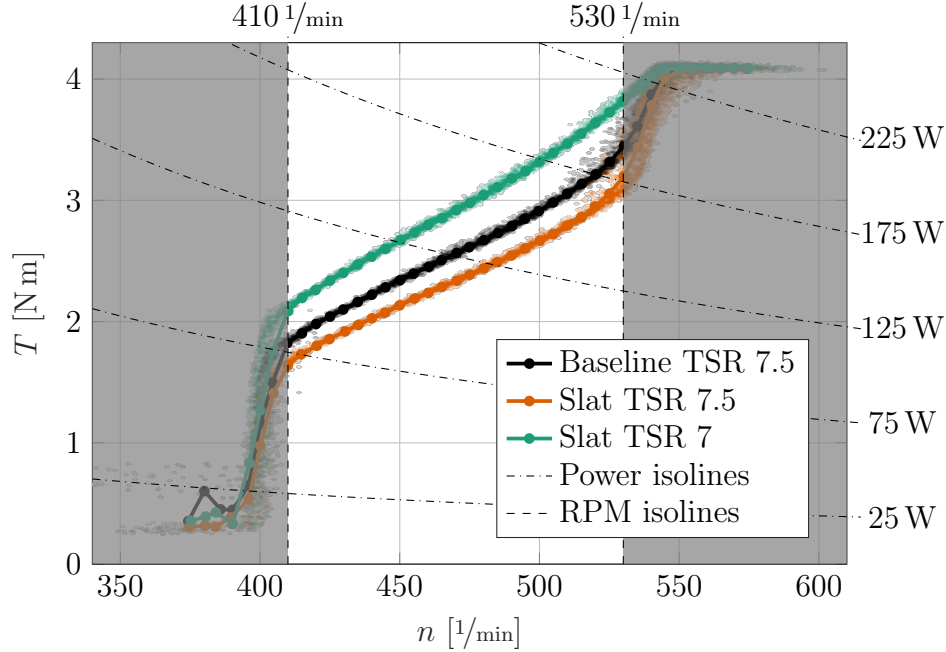


Figure 5.9: Torque dependent on the rotational speed for the different configurations.

Considering the purely partial load region ($410 \text{ 1/min} < n < 530 \text{ 1/min}$), the drift of the slat configurations is partly higher and partly lower compared to the Baseline TSR 7.5 configuration. Close to the transition region ($n = 530 \text{ 1/min}$) higher D_1 (Slat TSR 7.5 due to steeper T - n -slope) and lower D_1 (Slat TSR 7 due to lower T - n -slope) can be recognized. In between spots with half to twice the absolute drift value of the Baseline TSR 7.5 configuration can be found for the slat configurations. Except the clear trend close to the switching region at 530 1/min , no clear tendency of the absolute drift ratio (higher or lower) can be found throughout the partial load region.

Evaluation of the deterministic turbine behavior

Differences in the drift field of the configurations can be recognized. However, these differences mainly occur outside the partial load region or close to its boundary and are caused by different controller settings. In the partial load region the differences are comparatively small. To further describe how these differences affect the deterministic turbine behavior, it is investigated by the deterministic power output P_{D_1} (Eq. 5.7) for different synthetic wind time series. The advantage of this synthetic study is that

it offers more freedom in the definition of the wind fields while providing exactly the same conditions (without the slightest deviations) for the different configurations studied. It helps to transfer the experimental data acquired to a broader parameter space and is faster than additional measurements (when meaningful data have already been collected).

Here, the complexity of the synthetic wind time series is increased in three steps. The simplest case, a velocity step, is used to determine the effect of the different configurations on the reaction time (exemplarily one upwards and one downwards step are chosen). In the next step, the mean power production of the different configurations for periodic velocity variations are investigated. Here, sinusoidal velocity variations with different amplitudes and frequencies and (closer to the wind energy application) gusts with different gust magnitudes and peak duration are chosen. The highest complexity is reached by using turbulent time series (which can be interpreted as a combination of different gust) with different mean wind speeds and TIs to analyze the corresponding mean power production for the different configurations.

Velocity step (reaction time) The individual deterministic power output for a velocity step upwards and downwards (according to Fig. 5.6) is simulated for the individual configurations (Fig. 5.10). Different power levels can be found for the configurations.

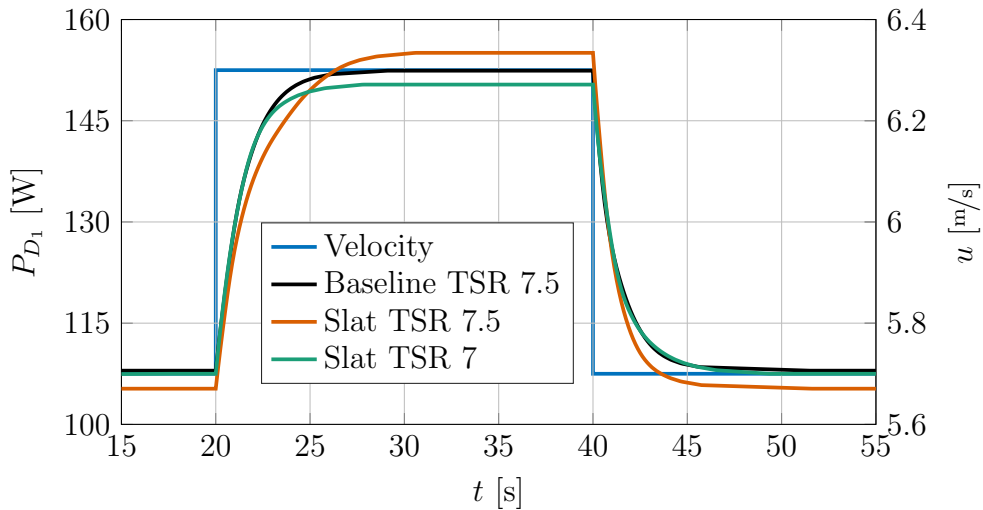


Figure 5.10: Comparison of the synthetic deterministic power time series P_{D_1} of the different configurations calculated based on D_1 for a velocity step.

Baseline TSR 7.5 and Slat TSR 7 are having almost the same power levels, whereas the Slat TSR 7.5 configuration exhibits a lower power output for the lower wind speed and a higher power output for the higher wind speed. In general all configurations show the same behavior of the deterministic power output. The slope (D_1) at the time step of the velocity steps is comparable for the different configurations (Tab. 5.3).

Table 5.3: Comparison of reaction time T_{int} for synthetic velocity steps of Δu 0.6 m/s upwards and downwards around 6 m/s mean wind speed.

Configuration	upwards step		downwards step	
	$T_{\text{int}}[\text{s}]$	$D_1(t = 20 \text{ s})$	$T_{\text{int}}[\text{s}]$	$D_1(t = 40 \text{ s})$
Baseline TSR 7.5	1.464	25.79	1.217	-42.07
Slat TSR 7.5	2.095	25.79	1.165	-40.77
Slat TSR 7	1.333	29.58	1.324	-35.69

Baseline TSR 7.5 and Slat TSR 7 configuration show comparable deterministic power time series, except from deviations due to different power levels. The Slat TSR 7.5 configuration is reaching the upper power level slower and the lower power limit faster than the other configurations. The corresponding reaction times (based on the integral) T_{int} cover this trend (Tab. 5.3). For upwards and downwards step, the Baseline TSR 7.5 and Slat TSR 7 configuration show reaction times in the same order of magnitude. The Slat TSR 7.5 configurations exhibits a more than 40% longer reaction time for the upwards step, whereas the reaction time for the downwards steps is comparable (even though slightly smaller) to the other configurations. For the Slat TSR 7 an opposite trend (however small difference to Baseline TSR 7.5 configuration) can be found, showing a slightly faster reaction time for the upwards and a slightly slower reaction time for the downwards velocity step.

Periodic velocity variations (mean power production) The reaction time of the turbine is influenced by the different configurations. Different deterministic power output time series can be observed. In the next step the consequence for the mean power production is investigated. To do so, simple periodic synthetic velocity variations, namely sinusoidal velocity variations and gusts based on the IEC-standard 61400-1 are used. For these test cases multiple amplitudes \hat{u} and gust magnitudes u_{gust} and frequencies f , respectively gust duration T_{gust} with a temporal spacing of $T_{\text{gust}}/2$ are considered for a mean wind speed of 6 m/s (Tab. 5.4). In Fig. 5.11 one period of the different test cases with the amplitude $\hat{u} = 0.45 \text{ m/s}$ and the gust magnitude $u_{\text{gust}} = 0.9 \text{ m/s}$ and the corresponding deterministic power outputs P_{D_1} of the Baseline TSR 7.5 configuration are shown for six frequencies from 0.2 Hz to 10 Hz. The variation of the deterministic power decreases with increasing frequency. For high frequencies, the response of the turbine is strongly damped, as no delayed response occurs due to the periodicity.

Table 5.4: Chosen parameter for synthetic test cases.

f and $1/T_{\text{gust}}$ [Hz]												$2\hat{u}$ and u_{gust} [m/s]						
0.2	0.25	0.4	0.5	1	1.25	2	2.5	5	10	12.5	25	0.3	0.5	0.7	0.9	1.1	1.3	1.5

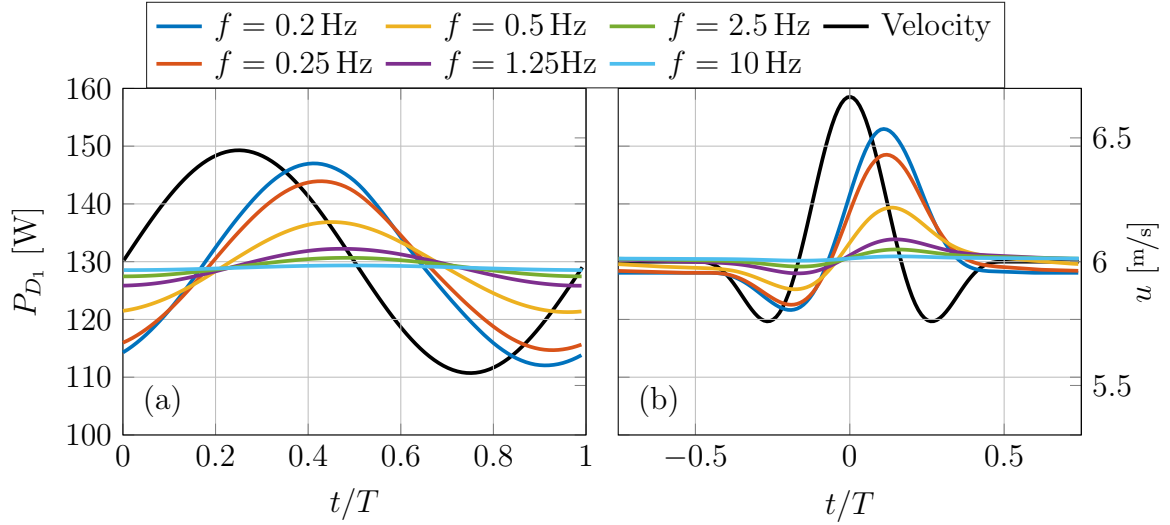


Figure 5.11: Examples of deterministic power P_{D_1} of the Baseline TSR 7.5 configuration for synthetic sinusoidal (a), and gust ($T_{\text{gust}} = 1/f$) (b) wind speed time series.

The deterministic power output is calculated for the different amplitudes and gust magnitudes and frequencies and gust duration (Tab. 5.4). For every case (sinusoidal and gust and Baseline TSR 7.5, Slat TSR 7.5, and Slat TSR 7) the mean of the deterministic power is estimated and the ratio towards the Baseline TSR 7.5 configuration determined. The corresponding results for the sinusoidal wind time series are shown in Fig. 5.12 and for the gust time series in Fig. 5.13. Mean power outputs (a, b) and relative power outputs in comparison to the Baseline TSR 7.5 configuration (c, d) are shown for the two configurations Slat TSR 7.5 (a, c) and Slat TSR 7 (b, d), respectively.

At low frequencies an increase of the mean of the deterministic power P_{D_1} with the amplitude can be recognized (Fig. 5.12 (a, b)). This effect is stronger for the Slat TSR 7.5 configuration, whereas it is small for the Slat TSR 7 configuration. The higher the frequency, the lower the increase. For the Slat TSR 7 configuration even a slight decrease in mean power with increasing amplitude can be recognized at high frequencies. In comparison to Baseline TSR 7.5 configuration, the mean power is reduced by up to 5% for the Slat TSR 7.5 configuration (Fig. 5.12 (c)). The Slat TSR 7 shows a comparable mean power (within 2%) as the Baseline TSR 7.5 configuration (Fig. 5.12 (d)). However, the ratio decreases with increasing amplitude and frequency. All three configurations show clear differences in their mean deterministic power output dependent on the inflow velocity.

The mean deterministic power for a synthetic gust increases with increasing gust magnitude (Fig. 5.13 (a, b)). Again the effect decreases with increasing frequency (decreasing gust duration). In comparison to the Baseline TSR 7.5 configuration, the mean deterministic power is reduced by roughly 5% for the Slat TSR 7.5 configuration (Fig. 5.13 (c)). The Slat TSR 7 shows a comparable mean deterministic power (within

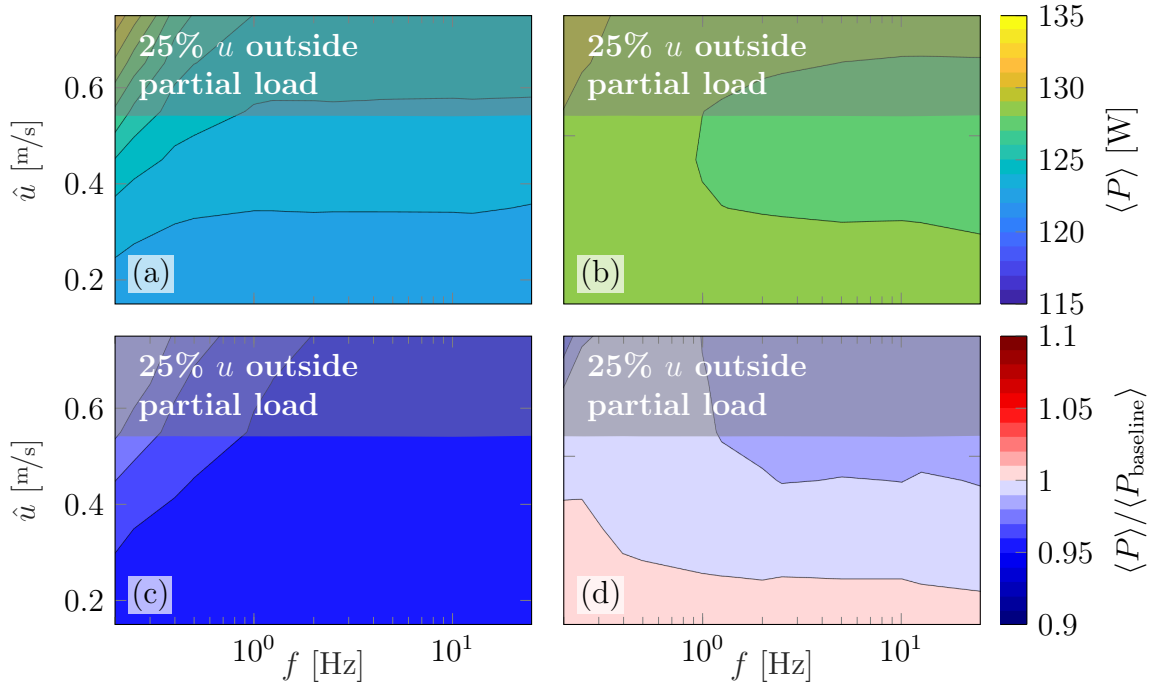


Figure 5.12: Mean deterministic power output P_{D_1} for Slat TSR 7.5 (a) and TSR 7 (b) configuration under sinusoidal velocity variation with amplitude \hat{u} and frequency f and corresponding ratios towards Baseline TSR 7.5 configuration (c, d).

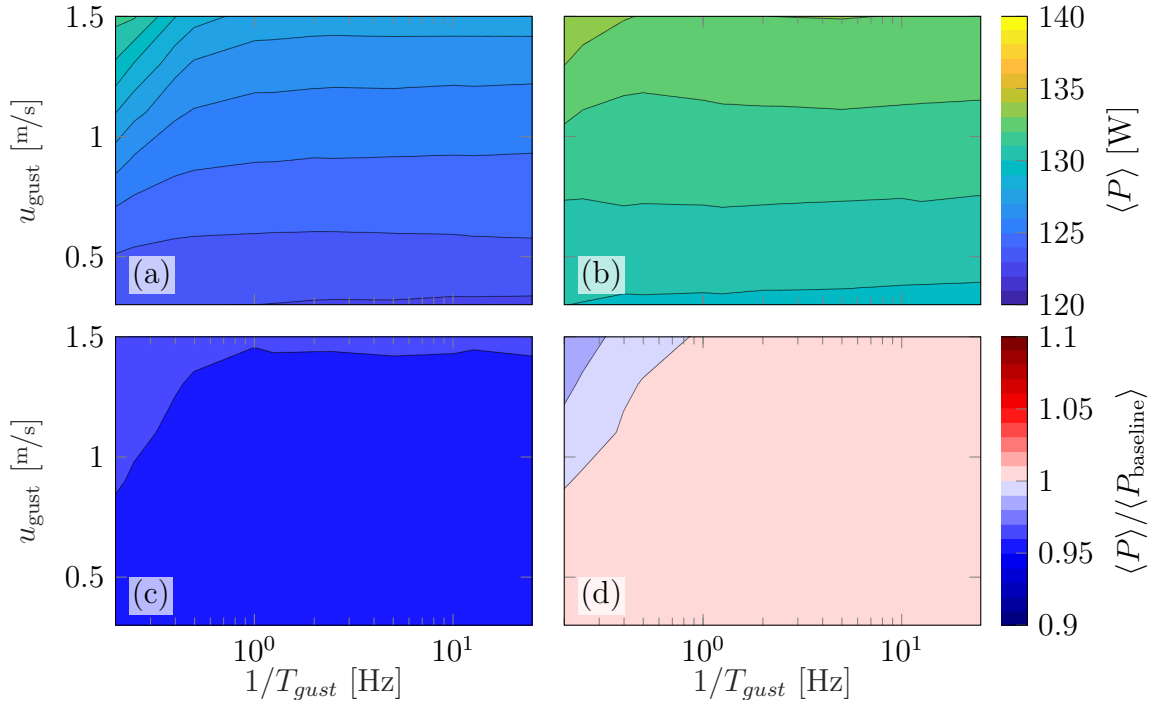


Figure 5.13: Mean deterministic power output P_{D_1} for Slat TSR 7.5 (a) and TSR 7 (b) configuration experiencing a gust with magnitude u_{gust} and duration T_{gust} and corresponding ratios towards Baseline TSR 7.5 configuration (c, d).

2%) as the Baseline TSR 7.5 configuration (Fig. 5.13 (d)). With increasing gust magnitude and frequency (decreasing gust duration) the ratio increased.

The Langevin approach allows for investigating effects on different isolated events. It enables to detect even small difference in the deterministic behavior of different turbine configurations and assign them to certain inflow conditions.

Turbulent time series (mean power production) In the last step, synthetic turbulent wind fields are used to model the turbine behavior. Previously, the turbine behavior was investigated based on its behavior on the amplitude and frequency of single events. By turbulent wind fields the turbine configurations are studied under complex, realistic combinations of frequencies and amplitudes. To do so, the same wind speed time series (see Appx. B for details) is scaled to different mean wind speeds $\langle u \rangle$ and turbulence intensities (TI) (Tab. 5.5).

Table 5.5: Investigated mean wind speeds $\langle u \rangle$ and turbulence intensities (TI) for the synthetic wind time series.

$\langle u \rangle$ [m/s]	$\Delta \langle u \rangle$ [m/s]	TI [%]	Δ TI [%]
5.2 — 6.8	0.1	0 — 20	1

Again, the deterministic power output P_{D_1} is estimated for the synthetic wind time series. The resulting mean values for the two slat configurations are shown in Fig. 5.14 (a, b). The ratio of the mean deterministic power of the slat configurations towards the Baseline TSR 7.5 configuration are shown in Fig. 5.14 (c, d). Additionally, the regions outside the partial load region (where only major effects by the controller settings should be expected) and the regions, where due to high turbulence intensity wind and power combinations are exceeding the model boundaries are marked.

A small dependency (which depends on the mean wind speed) of the mean deterministic power on the TI can be found. The mean power is reduced compared to the Baseline TSR 7.5 configuration. However, for very low TI some cases are found with a slightly increased mean deterministic power. Outside the partial load region, higher mean deterministic powers can be found, caused by the different controller settings. Also a clear deviation from the trend (of a reduced mean deterministic power) can be observed, if the boundaries of the model are exceeded (Fig. 5.14 (c, d)). In consequence, considering the partial load region, where the dominant effects should be caused by the slat, the mean power output can be reduced by up to 6%.

By estimation of the deterministic power for a synthetic wind speed time series a systematic comparison of different configurations is possible. This allows to gain additional insight into consequences of deviations in drift D_1 and power curve (Langevin power curve). It was found, that the mean deterministic power increases with the amplitude for single events. This effect decreases with increasing frequency. The Slat TSR 7.5 configuration shows an unfavorable behavior when considering the mean deterministic power, which is decreased by up to 6%. For low amplitudes respectively

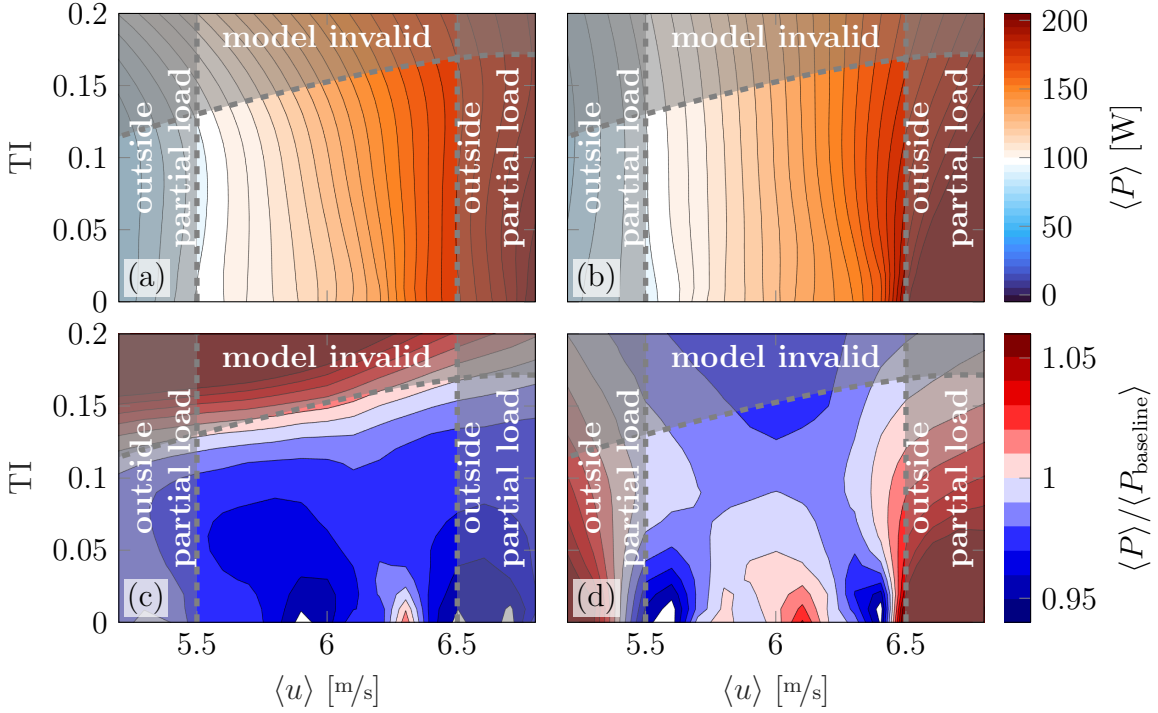


Figure 5.14: Mean deterministic power output P_{D1} for the Slat TSR 7.5 (a) and Slat TSR 7 (b) configuration dependent on wind velocity and turbulence intensity of a synthetic wind time series and the ratios towards the Baseline TSR 7.5 configuration (c, d), respectively.

low TI the Slat TSR 7 shows a slightly favorable behavior and increases the mean deterministic power by up to 2%. Hence, only small differences are caused by the slat.

5.3 Conclusion

In this chapter, results of measurements with the MoWiTO 1.8 in turbulent inflow, generated by the active grid in combination with the wind tunnel fans are presented. A 30 min wind time series allowed to cover the whole power curve under medium turbulence intensity. A baseline turbine and two configurations with installed leading edge slats in the root region of the blades and with two different tip speed ratios, were investigated.

In this investigation a superposition of different alterations, i.e., slat-installation, TSR-variation, and controller-adaption can be found. The laminar characterization showed that the operation with slats is beneficial at low TSR (< 5.7), since slightly more energy is produced at these TSR compared to the baseline configuration. This low TSR value corresponds to a higher angle of attack at the blade. This could lead to flow separation in the root region, where the highest angles of attack occur. In the baseline configuration, this leads to a decrease in power, while in the slat configuration,

flow separation may be prevented, resulting in higher power generation compared to the baseline configuration.

For turbulent inflow and controlled operation, this low TSR were hardly reached. Differences were found in the IEC power curve and power spectral density. However, these methods only allow for a limited and averaged characterization (averaged over the whole time series) of the turbine configurations. Hence, as the objective is to give a tool to investigate the deterministic behavior of different model wind turbine configurations, a method based on the Langevin approach was developed. By this approach, additional insight is gained, as it holds detailed information for the individual operational regions and inflow conditions. Here a detailed examination of the drift coefficient is done.

The most prominent difference in the dynamic behavior of the turbine configurations are caused by the different controller settings and in consequence a different switching behavior between the controller regions. A clearly increased respectively decreased drift coefficient is found in this region by the slat configurations compared to the baseline configuration. To identify the effect of the slat, the purely partial load region, which is hardly affected by the controller switching, is investigated. A slight decrease of the absolute value of the drift coefficient for the slat configurations is observed here. This decrease of the drift coefficient is directly connected to an increased reaction time of the turbine. Depending on the flow fluctuations, this can have a beneficial effect on the power production. However, the differences caused by the slat are comparable small.

There are certain limitations of such a small filigree slat model, e.g., the low Reynolds number, a reduction in lift for low angle of attacks, the unfeasibility of slat tip and root optimization (unfavorable tip and root vorticies on the slat), and a bulky mount (disturbed flow). Hence, the investigation may not show the full capability of the slat. However, considering these restrictions highlights the capability of the Langevin approach to even detect small effects and allocate differences to individual operation points.

Concluding, the approach of investigating a model wind turbine under turbulent conditions and applying the Langevin approach, allowed to gain further insight into the deterministic behavior of the turbine. By the turbulent inflow, many different conditions and the respective individual dynamic response of the turbine are captured. Based on this, the Langevin approach allows to extract the deterministic behavior of the turbine. Differences between turbine configurations can be directly identified in this deterministic drift field and allow the differences to be assigned to specific operating regions. The drift field can further be used as stochastic model, which can be feed with synthetic wind fields to simulate the dynamic response of the turbine to specific user-defined situations as extreme events and investigate them isolated. By this, detail information on the dynamic behavior of the turbine in specific inflows can be gained and in consequence, a comparison of different configurations under unique user-defined conditions can be done. This approach can also be transferred to other parameter (such as torque, rotational speed, blade root bending moments, tower bending moments) and setups.

Chapter 6

Conclusion

In this thesis, a method was developed to generate reproducible atmosphere-like inflow conditions in the wind tunnel. The flow response to the excitation by an active grid was studied and its behavior characterized. By the generation process large scale turbulence is brought into a small wind tunnel. This is a big step for fundamental turbulence research, facilitating the investigation of old discoveries and unravel turbulence questions. Furthermore, the generated flows enable systematic investigations of model wind turbines under reproducible atmosphere-like inflow conditions. Exemplarily, a model wind turbine with different rotor configurations was investigated under such inflow conditions and its dynamic behavior was characterized based on the Langevin approach.

For the generation of the inflow a *blockage induced flow design* approach for the excitation by the active grid was used. This allows to generate specific events by a quasi-steady transfer function. Limits of this approach are identified by a systematic analysis of dynamics of the generated flow structures. These limits are giving a design parameter (namely the reduced frequency which further defines the flap size) for the construction of active grids. In a next step, further effort needs to be spend on a smart, adaptable compensation method for the damping of the imprintable flow structures, which occurs with increasing excitation frequency. Both, the constant blockage approach but also the procedure to characterize the active grid behavior, can be transferred to other active grids.

Flows generated by this approach, exhibit a gap in the power spectral density. This gap is a consequence of the different physical excitation being passive by the grid design (small scales) and active by the shaft motion (large scales). Downstream the flow undergoes a complex transition (closing this gap) to a fully developed turbulence state (homogeneous, isotropic on the small scales, fulfilling K41 and K62) exhibiting highest Taylor-scale Reynolds numbers Re_{λ_T} . These Re_{λ_T} can be increased to atmospheric-like values (exceeding 10.000) by including a dynamic fan speed variation. With this, an additional one-dimensional driving of the flow is possible, which creates structures larger than the wind tunnel.

The generated high Reynolds number turbulence exhibits comparatively large in-

intermittent small scale turbulence, which opens up new opportunities for studying wind tunnel models affected by it. Hence, the active grid excitation approach allows on the one hand for investigations under atmospheric-like conditions and on the other hand may help to shed some light on old discoveries (e.g., the bottleneck effect (Lohse and Müller-Groeling, 1995)) by reproducible large small scale high Reynolds number turbulence. Further, the observed spectral gap (which is also found in the atmosphere) and its closing downstream are worth further investigations to understand its physics and ways to actively influence it by a sophisticated excitation.

Another feature is, that the generated flows allow to investigate different wind turbine concepts under reproducible conditions. In the chosen example, differences were detected that could be assigned to specific operating points by a stochastic analysis based on the Langevin equation. The deterministic behavior of the model wind turbine can be characterized and further used to simulate the behavior using synthetic inflows. This allows for a systematic analysis of the turbine and the study of its behavior during unique events (such as short gusts) that can not be generated by the active grid. In this way, further insight can be gained into the different turbine dynamics and differences dependent on operating points can be identified. This method, shown for power output, can be applied to other parameters (e.g., torque, rotational speed, blade root bending moments, tower bending moments) and contribute to a better understanding of the deterministic behavior of wind turbines.

In conclusion, a new approach for flow excitation by an active grid has been elaborated and analyzed in detail, providing a powerful method for flow generation in the wind tunnel. This active grid excitation approach can be used to generate both single extreme events and atmospheric-like turbulence with highest Reynolds numbers. These flows provide an excellent opportunity to conduct fundamental turbulence research and also to study wind turbines under realistic conditions. Based on the Langevin approach, model turbines experiencing these inflows can be analyzed to characterize their deterministic dynamic behavior. Both together, the active grid excitation and the Langevin approach, provide an extremely valuable method for the investigation and quantitative evaluation of wind turbine concepts under realistic conditions in the wind tunnel. This method facilitates the development of more sophisticated wind turbines and is thus an (albeit small) cog in the wheel of the energy transition to counteract climate change.

Bibliography

- Alexakis A, Mininni P, Pouquet A (2005) Imprint of large-scale flows on turbulence. *Physical review letters* 95(26):264503
- Anahua E, Barth S, Peinke J (2008) Markovian power curves for wind turbines. *Wind Energy: An International Journal for Progress and Applications in Wind Power Conversion Technology* 11(3):219–232
- Aramendia I, Fernandez-Gamiz U, Ramos-Hernanz JA, Sancho J, Lopez-Guede JM, Zulueta E (2017) Flow control devices for wind turbines. In: *Energy Harvesting and Energy Efficiency*, Springer, pp 629–655
- Arneodo A, Baudet C, Belin F, Benzi R, Castaing B, Chabaud B, Chavarria R, Ciliberto S, Camussi R, Chilla F, Dubrull B, Gagne Y, Hebral B, Peinke J, van de Water W, et al. (1996) Structure functions in turbulence, in various flow configurations, at Reynolds number between 30 and 5000, using extended self-similarity. *EPL (Europhysics Letters)* 34(6):411
- Aronson D, Löfdahl L (1993) The plane wake of a cylinder: measurements and inferences on turbulence modeling. *Physics of Fluids A: Fluid Dynamics* 5(6):1433–1437
- Berger F, Kröger L, Onnen D, Petrović V, Kühn M (2018) Scaled wind turbine setup in a turbulent wind tunnel. In: *Journal of Physics: Conference Series*, IOP Publishing, vol 1104, p 012026
- Berger F, Onnen D, Schepers G, Kühn M (2021) Experimental analysis of radially resolved dynamic inflow effects due to pitch steps. *Wind Energy Science* 6(6):1341–1361
- Berger F, Neuhaus L, Onnen D, Hölling M, Schepers G, Kühn M (2022) Experimental analysis of the dynamic inflow effect due to coherent gusts. *Wind Energy Science* 7(5):1827–1846
- Betz A (1927) Die Windmühlen im Lichte neuerer Forschung. *Naturwissenschaften* 15(46):905–914
- Bodenschatz E, Bewley GP, Nobach H, Sinhuber M, Xu H (2014) Variable density turbulence tunnel facility. *Review of Scientific Instruments* 85(9):093908

- Bossanyi E, Savini B, Iribas M, Hau M, Fischer B, Schlipf D, van Engelen T, Rossetti M, Carcangiu C (2012) Advanced controller research for multi-mw wind turbines in the UPWIND project. *Wind Energy* 15(1):119–145
- Böttcher F, Peinke J (2007) Small and large scale fluctuations in atmospheric wind speeds. *Stochastic environmental research and risk assessment* 21(3):299–308
- Bourgoin M, Baudet C, Kharche S, Mordant N, Vandenberghe T, Sumbekova S, Stelzenmuller N, Aliseda A, Gibert M, Roche PE, Bodenschatz E, Bewley G, Sinhuber M, Örlü, Puczyłowski J, Peinke J, et al. (2018) Investigation of the small-scale statistics of turbulence in the modane slma wind tunnel. *CEAS Aeronautical Journal* 9(2):269–281
- Bradley EF, Antonia R, Chambers A (1981) Turbulence Reynolds number and the turbulent kinetic energy balance in the atmospheric surface layer. *Boundary-Layer Meteorology* 21(2):183–197
- Brown R (1828) Xxvii. a brief account of microscopical observations made in the months of june, july and august 1827, on the particles contained in the pollen of plants; and on the general existence of active molecules in organic and inorganic bodies. *The philosophical magazine* 4(21):161–173
- Burton T, Jenkins N, Sharpe D, Bossanyi E (2011) *Wind energy handbook*. John Wiley & Sons
- Castaing B, Gagne Y, Hopfinger E (1990) Velocity probability density functions of high Reynolds number turbulence. *Physica D: Nonlinear Phenomena* 46(2):177–200
- Cekli HE, van de Water W (2010) Tailoring turbulence with an active grid. *Experiments in fluids* 49(2):409–416
- Cekli HE, Joosten R, van de Water W (2015) Stirring turbulence with turbulence. *Physics of Fluids* 27(12):125107
- Chen D, Rojas M, Samset BH, K Cobb, Diongue-Niang A, Edwards P, Emori S, Faria SH, Hawkins E, Hope P, Huybrechts P, Meinshausen M, Mustafa SKEAR, Plattner GK, Treguier AM, et al. (2021) Framing, context, and methods. In: *Climate change 2021: the physical science basis*, Cambridge University Press, pp 145–286
- Chilla F, Peinke J, Castaing B (1996) Multiplicative process in turbulent velocity statistics: A simplified analysis. *Journal de Physique II* 6(4):455–460
- da Vinci L (1510–1512) *Studies of turbulent water*, Royal collection trust, ©Her Majesty Queen Elizabeth II 2019
- Davidson P (2004) *Turbulence: An Introduction for Scientists and Engineers*. OUP Oxford

- Deutsche Windguard (2021a) Status des Offshore-Windenergieausbaus in Deutschland – Jahr 2020. Tech. rep.
- Deutsche Windguard (2021b) Status des Windenergieausbaus an Land in Deutschland – Jahr 2020. Tech. rep.
- DNW (2021) DNW german-dutch wind tunnels, large low-speed facility, <https://www.dnw.aero/wind-tunnels/llf> (accessed: 04.08.2022)
- Domaradzki JA, Rogallo RS (1990) Local energy transfer and nonlocal interactions in homogeneous, isotropic turbulence. *Physics of Fluids A: Fluid Dynamics* 2(3):413–426
- Einstein A (1905) Über die von der molekularkinetischen Theorie der Wärme geforderte Bewegung von in ruhenden Flüssigkeiten suspendierten Teilchen. *Annalen der Physik* 4
- ForWind (2021) ForWind center for wind energy research, generating turbulent wind fields in the large wind tunnel, <https://forwind.de/en/research/infrastructures/active-grid/> (accessed: 04.08.2022)
- Friedrich R, Peinke J, Sahimi M, Tabar MRR (2011) Approaching complexity by stochastic methods: From biological systems to turbulence. *Physics Reports* 506(5):87–162
- Frisch U (1995) *Turbulence: the legacy of AN Kolmogorov*. Cambridge university press
- Gaunaa M, Zahle F, Sørensen NN, Bak C (2012) Quantification of the effects of using slats on the inner part of a 10MW rotor. *Proceedings of EWEA* pp 919–930
- Gillett NP, Kirchmeier-Young M, Ribes A, Shiogama H, Hegerl GC, Knutti R, Gastineau G, John JG, Li L, Nazarenko L, et al. (2021) Constraining human contributions to observed warming since the pre-industrial period. *Nature Climate Change* 11(3):207–212
- Good GH, Warhaft Z (2011) On the probability distribution function of the velocity field and its derivative in multi-scale turbulence. *Physics of Fluids* 23(9):095106
- Gottschall J, Peinke J (2008) How to improve the estimation of power curves for wind turbines. *Environmental Research Letters* 3(1):015005
- Griffin KP, Wei NJ, Bodenschatz E, Bewley GP (2019) Control of long-range correlations in turbulence. *Experiments in Fluids* 60(4):55
- GWEC (2021) *Global Wind Energy Council – global wind report 2021*
- Hearst RJ, Ganapathisubramani B (2017) Tailoring incoming shear and turbulence profiles for lab-scale wind turbines. *Wind Energy* 20(12):2021–2035

- Hearst RJ, Lavoie P (2015) The effect of active grid initial conditions on high Reynolds number turbulence. *Experiments in Fluids* 56(10):185
- Heslot F, Castaing B, Libchaber A (1987) Transitions to turbulence in helium gas. *Physical Review A* 36(12):5870
- Hurst D, Vassilicos J (2007) Scalings and decay of fractal-generated turbulence. *Physics of Fluids* 19(3):035103
- IEC (2017) Wind turbine generator systems, part 12-1 – power performance measurements of electricity producing wind turbines. Standard IEC 61400-12-1:2017, International Electrotechnical Commission, Geneva, Switzerland
- IEC (2019) Wind turbine generator systems, part 1 – design requirements. Standard IEC 61400-1:2019, International Electrotechnical Commission, Geneva, Switzerland
- iwd (2020) iwd – Der Informationsdienst des Instituts der deutschen Wirtschaft - Windkraft: Ausbau kommt nicht voran, <https://www.iwd.de/artikel/windkraft-ausbau-kommt-nicht-voran-457916/> (accessed: 04.08.2022)
- Jaume AM, Wild J (2016) Aerodynamic design and optimization of a high-lift device for a wind turbine airfoil. In: *New Results in Numerical and Experimental Fluid Mechanics X*, Springer, pp 859–869
- Kaimal JC, Wyngaard J, Izumi Y, Coté O (1972) Spectral characteristics of surface-layer turbulence. *Quarterly Journal of the Royal Meteorological Society* 98(417):563–589
- Kaiser K, Langreder W, Hohlen H, Højstrup J (2007) Turbulence correction for power curves. In: *Wind Energy*, Springer, pp 159–162
- Klipp C (2014) Turbulence anisotropy in the near-surface atmosphere and the evaluation of multiple outer length scales. *Boundary-layer meteorology* 151(1):57–77
- Knebel P, Kittel A, Peinke J (2011) Atmospheric wind field conditions generated by active grids. *Experiments in fluids* 51(2):471–481
- Kolmogorov AN (1941) The local structure of turbulence in incompressible viscous fluid for very large Reynolds numbers. *Cr Acad Sci URSS* 30:299–303
- Kolmogorov AN (1962) A refinement of previous hypotheses concerning the local structure of turbulence in a viscous incompressible fluid at high Reynolds number. *Journal of Fluid Mechanics* 13(1):82–85
- Kröger L, Frederik J, van Wingerden JW, Peinke J, Hölling M (2018a) Generation of user defined turbulent inflow conditions by an active grid for validation experiments. *Journal of Physics: Conference Series* 1037(5):052002

- Kröger L, Neuhaus L, Peinke J, Gülker G, Hölling M (2018b) Turbulence generation by active grids. In: *iTi Conference on Turbulence*, Springer, pp 191–196
- Larssen JV, Devenport WJ (2011) On the generation of large-scale homogeneous turbulence. *Experiments in fluids* 50(5):1207–1223
- Lemons DS, Gythiel A (1997) Paul Langevin’s 1908 paper ”on the theory of brownian motion” [”sur la théorie du mouvement brownien,” *cr acad. sci.(paris)* 146, 530–533 (1908)]. *American Journal of Physics* 65(11):1079–1081
- Lohse D, Müller-Groeling A (1995) Bottleneck effects in turbulence: scaling phenomena in r versus p space. *Physical review letters* 74(10):1747
- Makita H (1991) Realization of a large-scale turbulence field in a small wind tunnel. *Fluid Dynamics Research* 8(1-4):53
- Meneveau C (2019) Big wind power: seven questions for turbulence research. *Journal of Turbulence* pp 1–19
- Menezes EJM, Araújo AM, da Silva NSB (2018) A review on wind turbine control and its associated methods. *Journal of cleaner production* 174:945–953
- Milan P, Wächter M, Peinke J (2013) Turbulent character of wind energy. *Physical review letters* 110(13):138701
- Morales A, Wächter M, Peinke J (2012) Characterization of wind turbulence by higher-order statistics. *Wind Energy* 15(3):391–406
- Mydlarski L (2017) A turbulent quarter century of active grids: from Makita (1991) to the present. *Fluid Dynamics Research* 49(6):061401
- Mydlarski L, Warhaft Z (1996) On the onset of high-Reynolds-number grid-generated wind tunnel turbulence. *Journal of Fluid Mechanics* 320:331–368
- Mydlarski L, Warhaft Z (1998) Passive scalar statistics in high-Péclet-number grid turbulence. *Journal of Fluid Mechanics* 358:135–175
- Neuhaus L, Singh P, Homeyer T, Huxdorf O, Riemenschneider J, Wild J, Peinke J, Hölling M (2018) Mitigating loads by means of an active slat. In: *Journal of Physics: Conference Series*, IOP Publishing, vol 1037, p 022032
- Neuhaus L, Hölling M, Bos WJT, Peinke J (2020) Generation of atmospheric turbulence with unprecedentedly large Reynolds number in a wind tunnel. *Physical Review Letters* 125(15):154503
- Neuhaus L, Berger F, Peinke J, Hölling M (2021) Exploring the capabilities of active grids. *Experiments in Fluids* 62(6):1–12

- Neunaber I, Braud C (2020) First characterization of a new perturbation system for gust generation: the chopper. *Wind Energy Science* 5(2):759–773
- Niemela J, Sreenivasan K (2006) The use of cryogenic helium for classical turbulence: promises and hurdles. *Journal of low temperature physics* 143(5-6):163–212
- Pechlivanoglou G, Nayeri C, Paschereit C (2010) Fixed leading edge auxiliary wing as a performance increasing device for hawt blades. DEWEK, Bremen, Germany
- Petrović V, Berger F, Neuhaus L, Hölling M, Kühn M (2019) Wind tunnel setup for experimental validation of wind turbine control concepts under tailor-made reproducible wind conditions. In: *Journal of Physics: Conference Series*, IOP Publishing, vol 1222, p 012013
- Pietropinto S, Poulain C, Baudet C, Castaing B, Chabaud B, Gagne Y, Hébral B, Ladam Y, Lebrun P, Pirotte O, Roche P (2003) Superconducting instrumentation for high Reynolds turbulence experiments with low temperature gaseous helium. *Physica C: Superconductivity* 386:512–516
- Poorte R, Biesheuvel A (2002) Experiments on the motion of gas bubbles in turbulence generated by an active grid. *Journal of Fluid Mechanics* 461:127–154
- Pope SB (2001) *Turbulent flows*. Cambridge university press
- Porté-Agel F, Bastankhah M, Shamsoddin S (2020) Wind-turbine and wind-farm flows: a review. *Boundary-Layer Meteorology* 174(1):1–59
- Pöschke F, Petrović V, Berger F, Neuhaus L, Hölling M, Kühn M, Schulte H (2022) Model-based wind turbine control design with power tracking capability: A wind-tunnel validation. *Control Engineering Practice* 120:105014
- Reinke N, Homeyer T, Hölling M, Peinke J (2017) Flow modulation by an active grid. arXiv preprint arXiv:170300721
- Reynolds O (1883) An experimental investigation of the circumstances which determine whether the motion of water shall be direct or sinuous, and of the law of resistance in parallel channels. *Philosophical Transactions of the Royal society of London* (174):935–982
- Richardson LF (1922) *Weather prediction by numerical process*. Cambridge University Press, Cambridge
- Ritchie H, Roser M (2020) Energy. Our World in Data <https://ourworldindata.org/energy>
- Ritchie H, Roser M, Rosado P (2020) CO₂ and greenhouse gas emissions. Our World in Data <https://ourworldindata.org/co2-and-other-greenhouse-gas-emissions>

- Saddoughi SG, Veeravalli SV (1994) Local isotropy in turbulent boundary layers at high Reynolds number. *Journal of Fluid Mechanics* 268:333–372
- Schmidt FN, Wild J (2021) Development of a passive-adaptive slat for a wind turbine airfoil. *Wind Energy*
- Shen X, Warhaft Z (2000) The anisotropy of the small scale structure in high Reynolds number ($R_\lambda \sim 1000$) turbulent shear flow. *Physics of Fluids* 12(11):2976–2989
- Shirzadeh K, Hangan H, Crawford C (2020) Experimental and numerical simulation of extreme operational conditions for horizontal axis wind turbines based on the IEC standard. *Wind Energy Science* 5(4):1755–1770
- Simmons L, Salter C (1934) Experimental investigation and analysis of the velocity variations in turbulent flow. *Proceedings of the Royal Society of London Series A, Containing Papers of a Mathematical and Physical Character* 145(854):212–234
- Singh P, Neuhaus L, Huxdorf O, Riemenschneider J, Wild J, Peinke J, Hölling M (2021) Experimental investigation of an active slat for airfoil load alleviation. *Journal of Renewable and Sustainable Energy* 13(4):043304
- Sinner M, Petrović V, Langidis A, Neuhaus L, Hölling M, Kühn M, Pao LY (2021) Experimental testing of a preview-enabled model predictive controller for blade pitch control of wind turbines. *IEEE Transactions on Control Systems Technology* pp 1–15
- Smith AM (1975) High-lift aerodynamics. *Journal of Aircraft* 12(6):501–530
- Sognnaes I, Gambhir A, Van de Ven D, Nikas A, Anger-Kraavi A, Bui H, Campagnolo L, Delpiazzo E, Doukas H, Giarola S, et al. (2021) A multi-model analysis of long-term emissions and warming implications of current mitigation efforts. *Nature Climate Change*
- Steiner J, Viré A, Benetti F, Timmer N, Dwight R (2020) Parametric slat design study for thick-base airfoils at high Reynolds numbers. *Wind Energy Science* 5(3):1075–1095
- Teßmer J, Monatano Rejas ZM, Rose M, Daniele E, Stoevesandt B, Riemenschneider J, Hölling M, Balzani C (2021) SmartBlades2 – Bau, Test und Weiterentwicklung intelligenter Rotorblätter: Schlussbericht: 01.06.2016–30.09.2020. Tech. rep., DLR Deutsches Zentrum für Luft- und Raumfahrt e.V.
- Van Kuik G, Peinke J, Nijssen R, Lekou D, Mann J, Sørensen JN, Ferreira C, van Wingerden J, Schlipf D, Gebraad P, et al. (2016) Long-term research challenges in wind energy—a research agenda by the european academy of wind energy. *Wind energy science* 1(1):1–39

- Veers P, Dykes K, Lantz E, Barth S, Bottasso CL, Carlson O, Clifton A, Green J, Green P, Holttinen H, Laird D, Lundquist JK, Meneveau C, Pao L, Peinke J, et al. (2019) Grand challenges in the science of wind energy. *Science* 366(6464):eaau2027
- Viehweger F (1989) The Kryo-Kanal Köln(KKK): Description of the tunnel conversion. thermal insulation, instrumentation, operational experience, test results and operating costs. AGARD, Special Course on Advances in Cryogenic Wind Tunnel Technology
- Viré A, LeBlanc B, Steiner J, Timmer N (2021) Experimental study of the effect of a slat on the aerodynamic performance of a thick base airfoil. *Wind Energy Science Discussions* pp 1–19
- Wächter M, Milan P, Mücke T, Peinke J (2011) Power performance of wind energy converters characterized as stochastic process: applications of the langevin power curve. *Wind Energy* 14(6):711–717
- Waleffe F (1992) The nature of triad interactions in homogeneous turbulence. *Physics of Fluids A: Fluid Dynamics* 4(2):350–363
- Weitemeyer S, Reinke N, Peinke J, Hölling M (2013) Multi-scale generation of turbulence with fractal grids and an active grid. *Fluid Dynamics Research* 45(6):061407
- Wester TT, Krauss J, Neuhaus L, Hölling A, Gülker G, Hölling M, Peinke J (2022) How to design a 2D active grid for dynamic inflow modulation. *Flow, Turbulence and Combustion* 108(4):955–972
- Zahle F, Gaunaa M, Sørensen NN, Bak C (2012) Design and wind tunnel testing of a thick, multi-element high-lift airfoil. *Proceedings of EWEA*

Appendix

A Generation of atmospheric turbulence

Kinetic energy balance ¹

Grid-turbulence is created by generating perturbations which then develop into turbulence. Let us call the initially imposed perturbations U_i and the developed self-organized turbulent fluctuations u_i . The associated turbulent kinetic energy is

$$k = \frac{1}{2} \overline{u_i u_i}. \quad (6.1)$$

The balance for k writes,

$$d_t k = p - \epsilon, \quad (6.2)$$

where p is given by

$$p = \overline{u_i u_j} D_{ij}, \quad (6.3)$$

where $D_{ij} = (\partial_i U_j + \partial_j U_i)/2$. Using a classical eddy-viscosity assumption, p can be written as

$$p = \nu_T D_{ij} D_{ij}, \quad (6.4)$$

where ν_T is determined by the turbulent fluctuations u_i . A classical grid induces mainly transverse fluctuations of the stream-wise velocity, leading to

$$p \sim \nu_T \frac{U_x^2}{M^2}, \quad (6.5)$$

where M is the transverse correlation size of the turbulent fluctuations, and U_x is set by the velocity deficit in the grid-bar-wakes. Streamwise modulation adds a second term to the production, leading to

$$p \sim \nu_T \left(\frac{U_x^2}{M^2} + \frac{U_y^2}{L^2} \right), \quad (6.6)$$

¹W.J.T. Bos wrote this section as supplemental material to Lars Neuhaus, Wouter J. T. Bos, Michael Hölling, and Joachim Peinke: Generation of atmospheric turbulence with unprecedentedly large Reynolds-number in a wind tunnel, *Physical Review Letters*, 2020. L. Neuhaus carried out the measurements as well as the scientific analysis and wrote the manuscript. W.J.T. Bos helped to interpret the results and wrote the section "kinetic energy balance". Michael Hölling and Joachim Peinke had a supervising function.

where L is the longitudinal correlation length of the transverse fluctuations induced by the modulation of fan and active grid. The length L , since it is longitudinal, is not constrained by the width of the wind tunnel. If the size of the perturbations U_y is large enough, this contribution to the kinetic energy balance allows the injection of kinetic energy into the turbulence at typical scales of order L .

Evidently, this order-of-magnitude estimate does not take into account the detailed multi-scale nature of the injection, but only shows, on the level of integral quantities, how the large scales are affected by transverse and longitudinal shear-layers, with given correlation-lengths.

B Model wind turbine in turbulent inflow

Drift fields

On a first glance, the drift fields of the different configurations show comparable behavior (Fig. B.1). Close to the full load region ($u > 7.5$ m/s), the drift coefficient exhibits its largest values.

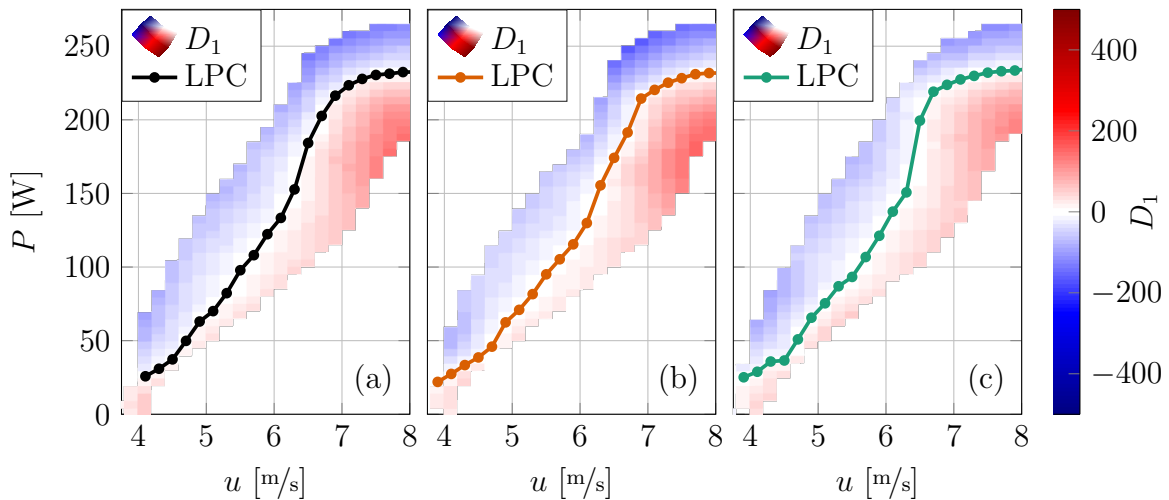


Figure B.1: Drift D_1 dependent on wind speed u and power P for the different configurations Baseline TSR 7.5 (a), Slat TSR 7.5 (b), and Slat TSR 7 (c).

Drift slopes

To highlight the drift behavior, D_1 is plotted dependent on the power P for different wind speeds (Fig. B.2). At the lowest shown wind speed ($u = 5.5$ m/s), the absolute slope of D_1 increases for low power (Fig. B.2 (a)). All configurations show a comparable behavior. At $u = 6$ m/s, which is in the middle of the partial load region, D_1 exhibits a linear trend for a wide power range, which only deviates at high power outputs (Fig. B.2 (b)). Again the configurations are quite comparable. However, for high

power outputs a deviation can be recognized. The Slat TSR 7.5 configuration exhibits the highest absolute D_1 from 175 W on. The Slat TSR 7 configuration shows the lowest absolute values here, but is close to the Baseline TSR 7.5 configuration. At high wind speed ($u = 6.5 \text{ m/s}$), this trend continues (Fig. B.2 (c)). The Slat TSR 7.5 configuration exhibits the highest absolute D_1 , while the lowest absolute D_1 can be observed for the Slat TSR 7 configuration. Note that for the Slat TSR 7 configuration no clear zero-crossing can be observed for this wind speed, but a region of powers with comparatively low D_1 . Also different zero-crossings (stable fixed points) can be observed for the different configurations. The biggest deviations between the configurations can be observed outside the partial load region ($P = 75 \text{ W}$ to 175 W considering $n = 410 \text{ }^1/\text{min}$ to $530 \text{ }^1/\text{min}$).

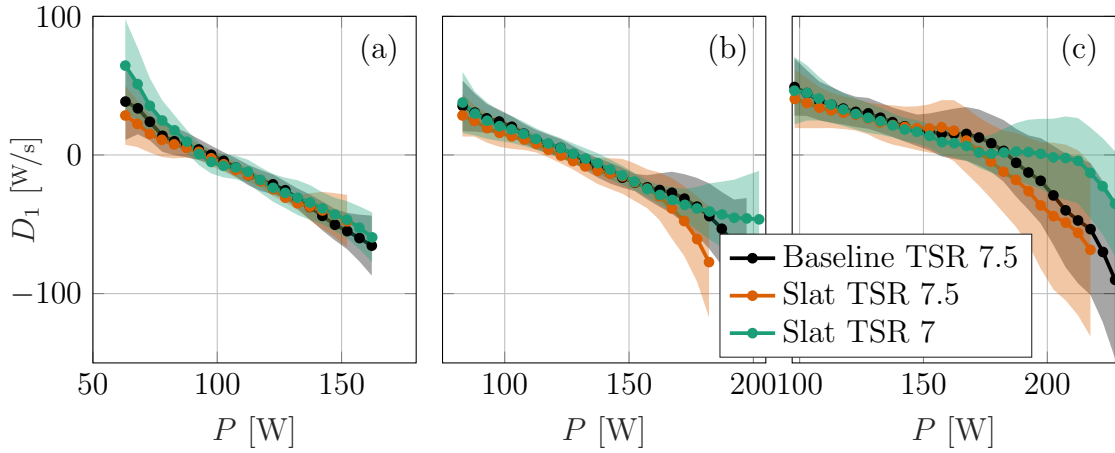


Figure B.2: Drift D_1 dependent on power P for the wind speeds 5.5 m/s (a), 6 m/s (b), and 6.5 m/s (c)

The drift over power slope dD_1/dP at the zero crossings (stable fixed points) are estimated and shown dependent on the wind speed (Fig. B.3). In the partial load region (deep colored curves) the slopes of the different configurations are comparable and constant. Outside the partial load region (light colored curves), the slopes differ due to different controller settings. Further, the full load controller leads to higher slopes of the drift coefficient.

Controller settings

The transition between partial and full load behaves different for the different controller settings. Fig. 5.9 shows the dependence of torque on the rotational speed. Five regions can be recognized. Below $400 \text{ }^1/\text{min}$, the torque is drastically reduced to keep the turbine running at the minimum rotational speed of $400 \text{ }^1/\text{min}$. Around $410 \text{ }^1/\text{min}$ a transition to the partial load controller can be recognized. From $410 \text{ }^1/\text{min}$ to roughly $530 \text{ }^1/\text{min}$ the partial load controller sets the torque $T = K_\lambda n^2$ based on the constant K_λ (Eq. 2.15). The curves of the individual configurations vary due to different K_λ

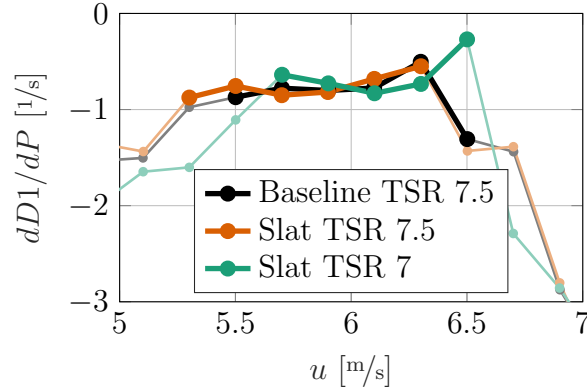


Figure B.3: The drift over power slope dD_1/dP at the zero crossing dependent on the wind speed. Deep colored curves mark the partial load region ($410 \text{ 1/min} < n < 530 \text{ 1/min}$).

values. Around 530 1/min a transition between the partial and full load controller is done. Here the slopes of the different configurations strongly differ. In the full load region ($n > 550 \text{ 1/min}$) all configurations show the same behavior.

As the power dependent on the wind speed is roughly the same for all configurations, a higher torque for the same rotational speed corresponds to a lower rotational speed at the same wind speed and in consequence a lower TSR. Hence, already the difference in the K_λ may make a difference in the dynamic response of the turbine. But the strongest differences in the dynamic behavior occur close to the full load region (Fig. 5.8). This might be caused by the significantly different slopes of torque over rotational speed (Fig. 5.9). The Slat TSR 7 configuration shows the lowest slope in this transition region (partial load curve and full load curve directly match). The Slat TSR 7.5 configuration exhibits the highest slope in this transition region.

The different slopes of the T - n -curves might have a significant effect on the drift values. In the transition region from partial to full-load ($530 \text{ 1/min} < n < 540 \text{ 1/min}$) the highest slope is found for the Slat TSR 7.5 configuration (Fig. 5.9). This configuration also exhibits the highest drift values around this region ($P > 150 \text{ W}$) (Fig. 5.8 (a)). For the Slat TSR 7 configuration the opposite is true, it exhibits the lowest slope in the T - n -plot and exhibits the lowest drift in this region (Fig. 5.8 (b)). The behavior at the lower transition region around 410 1/min , shows the same dependence of the drift on the T - n -slope (Fig. 5.9). Here the Slat TSR 7 configuration exhibits the highest slope and drift value, while both are the lowest for the Slat TSR 7.5 configuration.

Synthetic velocity time series

The velocity time series, which is used for the analysis of the deterministic power output in turbulent inflow, is measured with a hot-wire far downstream (100M) of the active grid. The flow is generated by the active grid similar as described in Ch. 3. By measuring far downstream a fully developed turbulence state is guaranteed. The

power spectral density is showing Kolmogorov's $-5/3$ power law over a wide range of frequencies (Fig. B.4). The frequency range of the previously investigated sinusoidal velocity variations is marked by a gray area. The lowest frequencies in the turbulent time series correspond to the low frequencies investigated for the sinusoidal velocity time series. Hence, both are covering a similar range of relevant scales, as the smallest scales (highest frequencies of the sinusoidal velocity variation) were found to have no significant effect on the deterministic power. For the systematic analysis of the deterministic power for different mean wind speeds and TIs, the synthetic wind speed time series

$$u_{\text{syn}} = (u_{\text{meas}} - \langle u_{\text{meas}} \rangle) \text{TI}_{\text{syn}} \langle u_{\text{syn}} \rangle + \langle u_{\text{syn}} \rangle \quad (6.7)$$

is build by subtraction of the original mean wind speed $\langle u_{\text{meas}} \rangle$ and adaption to the desired mean wind speeds $\langle u_{\text{syn}} \rangle$ and turbulence intensities TI_{syn} (for values shown in Tab. 5.5).

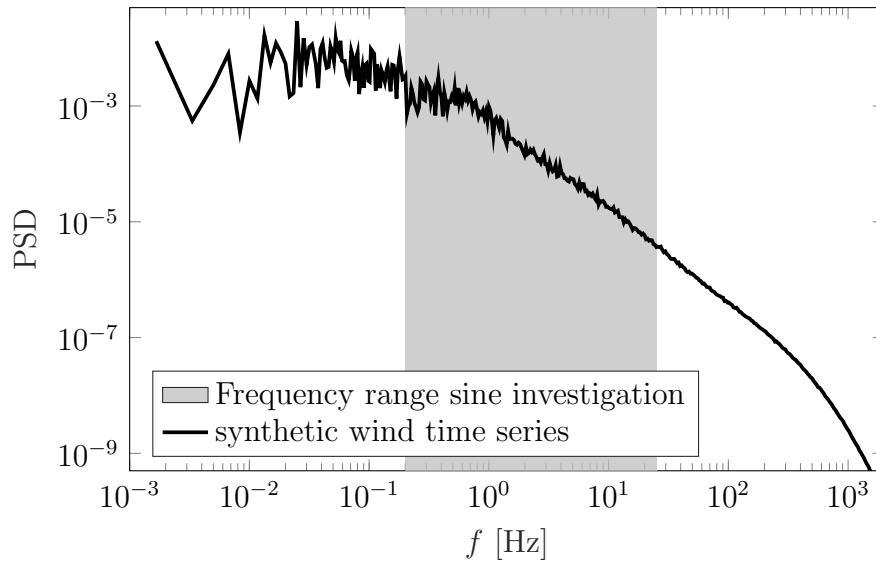


Figure B.4: Power spectral density (PSD) of the synthetic wind speed time series.

Acknowledgements / Danksagung

This work would not have been possible without the support of a large number of people, whom I would like to thank in this way. First of all, I want to thank Prof. Joachim Peinke for the opportunity to write this thesis in the working group TWiSt. I want to thank him for his supervision, the inspiring discussions and his infectious enthusiasm for wind energy and turbulence. I am also grateful to have been the first to investigate the new large active grid in detail.

I want to thank Dr. Michael Hölling, for all the fruitful discussions, for keeping me motivated, and helping to see the sense in all the data.

I also want to thank my co-authors for their support writing and reviewing papers.

Thanks to, Piyush my office mate, sharing frustrations and success. Further, Lars Köger for building up the large wind energy research facility active grid. I want to thank, Frederik Berger for compensating my lag of knowledge regarding turbine operation, and the time we spend in experiments together.

Also I want to thank Abdulkarim Abdulrazek, André Fuchs, Julian Jüchter, Gerrit Kampers, Gerd Gülker, Hendrik Heißelmann, Aga Hölling, Tim Homeyer, Apostolos Langidis, Pyei Phyo Lin, Thomas Messmer, Ingrid Neunaber, David Onnen, Vlaho Petrović, Christian Philipp, Jarek Puczyłowski, Lisa Rademacher, Michael Schwarz, Dominik Traphan, Lena Vorspel, Matthias Wächter, Tom Wester, Khaled Yassin, and all the other members of the TWiSt and WeSys working groups.

Also I would like to thank my family and friends. My wife for all the support and understanding but also for forcing me to bring this thesis to an end. To my daughter for brightening my day and putting a smile on my face. Thanks to my parents, who paved the way for my studies and thus for this thesis.

Furthermore, I would like to thank Jason Hearst for being my second exaimer.

Last but not least I want to thank the projects Smart Blades 2, ConUp, Wind-Elektrolyse (MWK), and the CRC 1463 Offshore Mega Structures for the funding of my research position and the possibility to work on topics accompanying my doctoral research.

I could give an endless list of other people here. Their contribution shall not be underestimated. I have experienced much further help in discussions, in the support of measurements, even through small suggestions and much more.

Thank you!

Curriculum

Personal information

Name	Lars Kristian Neuhaus
Date of Birth	19.03.1990
Place of Birth	Bonn
Citizenship	German

Education

10/2013 - 09/2016	M.Sc. Mechanical Engineering Leibniz Universität Hannover
10/2010 - 03/2014	B.Sc. Mechanical Engineering Leibniz Universität Hannover
06/2009	Abitur Grotefend-Gymnasium Münden

Professional

since 01/2022	Research fellow ForWind GmbH
since 11/2016	Research fellow ForWind, Institute of Physics, University of Oldenburg
10/2012 - 01/2016	Research assistant Leibniz Universität Hannover
04/2013 - 06/2013	Internship MTU Maintenance Hannover GmbH, Langenhagen

List of publications

Peer-reviewed journal articles

LN conducted the measurements, analyzed the data, and wrote the manuscript. Coauthors contributed in fruitful discussions and assisted writing the manuscript. MH and JP supervised the work.

Neuhaus L, Berger F, Peinke J, Hölling M (2021) Exploring the capabilities of active grids. *Experiments in Fluids* 62(6):1-12

Neuhaus L, Hölling M, Bos WJT, Peinke J (2020) Generation of atmospheric turbulence with unprecedentedly large Reynolds number in a wind tunnel. *Physical Review Letters* 125(15):154503

Additional publications

Peer-reviewed journal articles

LN contributed to the study conception and design and assisted in material preparation, data collection, and analysis:

Wester TTB, Krauss J, **Neuhaus L**, Hölling A, Gülker G, Hölling M, Peinke J (2022) How to design a 2D active grid for dynamic inflow modulation. *Flow, Turbulence and Combustion* 108:955-972

Singh P, **Neuhaus L**, Huxdorf O, Riemenschneider J, Wild J, Peinke J, Hölling M (2021) Experimental investigation of an active slat for airfoil load alleviation. *Journal of Renewable and Sustainable Energy* 13(4):043304

LN prepared and provided active grid motion protocols and assisted its operation:

Singh P, **Neuhaus L**, Abdulrazek A, Peinke J, Hölling M (2022 - in preparation) Turbulence intensity and its effect on thick airfoils; is it just a number or is there more to it?

Berger F, **Neuhaus L**, Onnen D, Hölling M, Schepers JG, Kühn M (2022) Experimental analysis of the dynamic inflow effect due to coherent gusts. *Wind Energy Science*, 7(5):1827–1846

Pöschke F, Petrović V, Berger F, **Neuhaus L**, Hölling M, Kühn M, Schulte H (2022) Model-based wind turbine control design with power tracking capability: a wind-tunnel validation. *Control Engineering Practice* 120:105014

van Dooren MF, Kidambi Sekar AP, **Neuhaus L**, Mikkelsen TK, Hölling M, Kühn M (2022) Modelling the spectral shape of continuous-wave lidar measurements in a turbulent wind tunnel. *Atmospheric Measurement Techniques* 15(5):1355–1372

Sinner M, Petrović V, Langidis A, **Neuhaus L**, Hölling M, Kühn M, Pao LY (2021) Experimental testing of a preview-enabled model predictive controller for blade pitch control of wind turbines. *IEEE Transactions on Control Systems Technology* 30(2), 583–597

Conference proceedings

LN performed material preparation, data collection, analysis, and prepared the presentation (shared contributions are marked):

Kröger L, **Neuhaus L**, Peinke J, Gülker G, Hölling M (2018) Turbulence generation by active grids. In: *iTi Conference on Turbulence*, Springer, pp 191-196 (*shared contribution with LK*)

Neuhaus L, Singh P, Homeyer T, Huxdorf O, Riemenschneider J, Wild J, Peinke J, Hölling M (2018) Mitigating loads by means of an active slat. In: *Journal of Physics: Conference Series*, IOP Publishing, vol 1037, p 022032 (*shared contribution with PS*)

Neuhaus L, Gilge P, Seume JR, Mulleners K (2016) Influence of surface roughness on the turbulent properties in the wake of a turbine blade. In: *18th International symposium on the Applications of Laser and Imaging Techniques to Fluid Dynamics*

LN prepared and provided active grid motion protocols and assisted its operation:

Sinner M, Petrović V, Berger F, **Neuhaus L**, Kühn M, Pao LY (2020) Wind tunnel testing of an optimal feedback/feedforward control law for wind turbines. *IFAC-PapersOnLine* 53(2), 12638-12643

Petrović V, Berger F, **Neuhaus L**, Hölling M, Kühn M (2019) Wind tunnel setup for experimental validation of wind turbine control concepts under tailor-made reproducible wind conditions. In: *Journal of Physics: Conference Series*, IOP Publishing, vol 1222 p 012013

LN and PS contribute a small section on slats:

Montano Rejas Z, Opitz S, Riemenschneider J, Werthen E, Pohl M, Govers Y, Gundlach J, Petrović V, Ungurán R, **Neuhaus L**, Singh P, Balzani C, Wentingmann M, Haldar A, Rolfes R (2019) Selected results on the development and testing of smart blades technologies for wind turbines. In Proceedings: ECCOMAS Thematic Conference on Smart Structures and Materials-SMART 2019, International Centre for Numerical Methods in Engineering (CIMNE), pp 102-117

Conference contributions first author / presenter

LN performed material preparation, data collection, analysis, and prepared the presentation (shared contributions are marked).

Neuhaus L, Berger F, Peinke J, Hölling M (2021) Tailoring inflows for wind turbine testing in wind tunnels (Presentation). Wind Energy Science Conference 2021. 25.-28. May 2021. Virtual

Neuhaus L, Hölling M, Peinke J (2021) Exciting atmospheric turbulence on lab-scales by an active grid (Presentation). iTi Conference on Turbulence IX. 25.-26. February 2021. Virtual

Neuhaus L, Bos WJT, Hölling M, Peinke J (2020) Exciting atmospheric turbulence on lab-scales by an active grid (Presentation). 73rd Annual Meeting of the APS Division of Fluid Dynamics. 22.-24. November 2020. Virtual

Neuhaus L, Peinke J, Hölling M (2019) High Reynolds number turbulence generation by active grid and wind tunnel control (Presentation). 17th European Turbulence Conference. 3.-6. September 2019. Turin, Italy

Neuhaus L, Berger F, Peinke J, Hölling M (2019) WESC 2019 Capturing wind turbine power curve and dynamics by atmospheric-like inflow at lab-scale (Presentation). Wind Energy Science Conference 2019. 17.-20. June 2019. Cork, Ireland

Neuhaus L, Hölling M, Peinke J (2019) Transition to highest Reynolds number turbulence by active grid and wind tunnel control (Presentation). Workshop on different states of turbulence and transitions from one state to the other: small and large-scale aspects and their interrelations. 13.-14. February 2019. Grenoble, France

Neuhaus L, Kröger L, Peinke J, Gülker G, Hölling M (2018) Active grid excitation for tailored turbulence generation (Presentation). 71st Annual Meeting of the APS Division of Fluid Dynamics. 18.-20. November 2018. Atlanta, Georgia (US)

Neuhaus L, Singh P, Homeyer T, Huxdorf O, Riemenschneider J, Wild J, Peinke J, Hölling M (2018) Mitigating loads by means of an active slat (Poster). The Science of Making Torque from Wind Conference. 20.-22. July 2018. Milan, Italy (*shared contribution with PS*)

Neuhaus L, Gilge P, Seume JR, Mulleners K (2016) Influence of surface roughness on the turbulent properties in the wake of a turbine blade (Presentation). 18th International Symposium on the Applications of Laser and Imaging Techniques to Fluid Mechanics. 04.-07. July 2016. Lisbon, Portugal

Neuhaus L, Melius MS, Cal RB, Mulleners K (2014) Design of a scaled non-rotating model wind turbine (Presentation). European Fluid Mechanics Conference 10. 15.-18. September 2014. Copenhagen, Denmark

Erklärung

Ich erkläre hiermit, dass

- (a) eine Promotion zum Dr.-Ing. angestrebt wird,
- (b) ich diese Arbeit selbständig und nur die angegebenen Hilfsmittel benutzt habe,
- (c) die Arbeit in Teilen bereits veröffentlicht bzw. zur Veröffentlichung eingereicht wurde,
- (d) ich die Leitlinien guter wissenschaftlicher Praxis der Carl von Ossietzky Universität Oldenburg befolgt habe,
- (e) im Zusammenhang mit dem Promotionsvorhaben keine kommerziellen Vermittlungs- oder Beratungsdienste (Promotionsberatung) in Anspruch genommen worden sind und
- (f) diese Dissertation weder in ihrer Gesamtheit noch in Teilen einer anderen Hochschule zur Begutachtung in einem Promotionsverfahren vorgelegen hat.

15.08.2022, Oldenburg



(Lars Neuhaus)